$IN-08$
76756
$P-113$

NASA Technical Memorandum 4356

Linearized Aerodynamic and Control Law Models of the X-29A Airplane and Comparison With Flight Data

John T. Bosworth

FEBRUARY 1992

NASA

NASA Technical Memorandum 4356

Linearized Aerodynamic and Control Law Models of the X-29A Airplane and Comparison With Flight Data

John T. Bosworth
Dryden Flight Research Facility
Edwards, California

CONTENTS

FIGURES

iv

vi

ABSTRACT

Flight control system design and analysis for aircraft rely on mathematical models of the vehicle dynamics. In addition to a six-degree-of-freedom nonlinear simulation, the X-29A flight controls group developed a set of programs that calculate linear perturbation models throughout the X-29A flight envelope. The models included the aerodynamics as well as flight control system dynamics and were used for stability, controllability, and handling qualities analysis. These linear models were compared to flight test results to help provide a safe flight envelope expansion. This report presents a description of the linear models at three flight conditions and two flight control system modes. The models are presented with a level of detail that would allow the reader to reproduce the linear results if desired. Comparisons between the response of the linear model and flight-measured responses are presented to demonstrate the strengths and weaknesses of the linear models' ability to predict flight dynamics.

INTRODUCTION

Advances in high-speed, light-weight flight control computers have made possible the development and flight test of vehicles with dynamic characteristics that are dominated by the flight control system. Flight control systems for these vehicles are generally complicated systems, which incorporate multiple control effectors as well as multiple feedback variables (Kempel and Earls, 1988). Although nonlinear simulation is generally used for final flight control system checkout, linear flight control system theory is still used for most of the flight control systems design and development.

A linear model, which includes the flight control system, rigid body aerodynamics, actuator dynamics, and feedback sensors and filters can provide an invaluable tool for the analysis of a new or modified flight control system design. Compared to a full nonlinear piloted simulation, the simplicity of the linear model allows for reasonably accurate results obtained in a timely manner, with minimal manpower. This makes the linear model a very useful tool to obtain surveys of stability, control, and handling qualities characteristics throughout the flight envelope. Even though these linear models play an important role in the early stages of the control system design and analysis, they are seldom validated after the flight-testing begins.

The X-29A aircraft is a recent example of a control configured vehicle that was designed with a high degree of longitudinal static instability (up to 35 percent at low subsonic speeds). The vehicle is stabilized by a full-authority, fly-by-wire flight control system. Linear models were used extensively prior to flight to determine the closed-loop stability, controllability, and handling qualities with the various control system modes throughout the flight envelope. During flight test, it was critical to closely monitor vehicle dynamic stability characteristics to ensure safe flight envelope expansion (Gera, 1986; Gera and Bosworth, 1987). Techniques were developed to compare in near real time the frequency response (Bosworth and West, 1986; Bosworth, 1989) and time response (Bauer et al, 1987) of the vehicle with predicted results. The linear simulation used to obtain the predicted results was the same linear model that was used for the control law development.

The X-29A linear model is the topic of discussion for this paper. Three flight conditions and two flight control system modes were selected for presentation. The flight conditions selected provided a take-off and landing configuration, a middle-of-the-flight envelope case, and a flight condition with one

of the quickest time-to-double amplitude (approximately 135 msec) open-loop instabilities. These three cases provided a representative sampling of the vehicle characteristics throughout the flight envelope. The analog backup control system mode was included along with the primary digital flight control system mode. The analog backup mode provides a more easily implementable model because of its analog elements and its reduced number of feedback variables. The rigid body aerodynamic models derived from the nonlinear aerodynamic database were obtained from wind-tunnel-test results. No attempt was made to update the aerodynamics with flight-test-derived parameter estimates. High-angle-of-attack or highly nonlinear flight conditions are not addressed. The linear models are compared with flight data in the frequency and time domain.

The linear models are discussed with enough detail that they could be recreated by the reader. The purpose is to provide realistic models that can be used in comparison to other aircraft, for academic discussion, or for general studies such as the effects of model reduction or sensitivity to changes in aerodynamic derivatives. These models represent a real aircraft with a state-of-the-art flight control system design.

NOMENCLATURE

Acronyms

ACC	automatic camber control
AR	analog reversion flight control system mode
FFT	fast Fourier transformation
KEAS	equivalent airspeed, kn
ND	normal digital flight control system mode
PA	powered approach flight control system mode
UA	up-and-away flight control system mode

Symbols

A	state derivative matrix
a	coefficient in strake flap noise filter
B	control derivative matrix
$BLEND$	angle-of-sideslip rate blending function
$BMAX$	rudder pedal command gain, deg/percent
$C1, C2, C3$	z-plane coefficients in rudder-to-aileron washout filter
$DFTA$	lateral stick position (ND mode), percent of full throw; (AR mode), in.
$DFTE$	longitudinal stick position (ND mode), percent of full throw; (AR mode), in.
$DFTR$	rudder pedal position (ND mode), percent of full throw; (AR mode), in.

2

e	error between pilot command and feedbacks, deg/sec
F	control observation matrix
Gp	lateral stick gearing gain, (deg/sec)/(percent)
$G1$	normal acceleration feedback gain, (rad/sec)/(g)
$G2$	pitch rate feedback gain, (deg/sec)/(deg/sec)
$G3$	pitch acceleration feedback gain, (deg/sec)/(deg/sec^2)
$G7$	pilot command gain, (rad)/(g)
$G8$	high-pass-filter gain, (deg/sec^2)/(deg)
$GMAX$	pitch stick command gain, (g)/(percent)
g	gravity constant, ft/sec^2
H	state observation matrix
h	altitude, ft
I_{xx}	moment of inertia about the x axis, lb ft sec^2
I_{xz}	xz product of inertia, lb ft sec^2
I_{yy}	moment of inertia about the y axis, lb ft sec^2
I_{zz}	moment of inertia about the z axis, lb ft sec^2
K_{ARI}	aileron-to-rudder gain, (deg)/(deg)
K_{FI}	symmetric flap feedforward gain, (deg)/(deg)
K_I	pitch axis integral feedforward gain, (deg)/(deg)
K_{LS}	lateral stick gain, (deg)/(in.)
K_P	roll rate feedback gain, (deg)/(deg/sec)
K_{RAI}	rudder-to-aileron gain, (deg)/(deg)
K_{RI}	yaw rate feedback gain, (deg)/(deg/sec)
K_{RP}	rudder pedal gain, (deg)/(in.)
K_c	longitudinal stick gain, (deg/sec)/(in.)
K_{cc}	pitch axis proportional feedforward gain, (deg)/(deg/sec)
K_{cs}	strake flap feedforward gain, (deg)/(deg)
K_q	pitch rate feedback gain, (deg/sec)/(deg/sec)
$K2$	roll rate-to-aileron gain, (deg/sec)/(deg/sec)
$K3$	yaw rate-to-aileron gain, (deg/sec)/(deg/sec)
$K4$	lateral acceleration-to-aileron gain, (deg/sec)/(g)
$K13$	lateral stick feedforward gain, (deg/sec)/(deg/sec)
$K14$	rudder-to-aileron gain, (deg/sec)/(percent)
$K16$	roll rate-to-rudder gain, (deg)/(deg/sec)
$K17$	yaw rate-to-rudder gain, (deg)/(deg/sec)

$K18$	lateral acceleration-to-rudder gain, (deg)/(g)
$K27$	aileron-to-rudder gain, (deg)/(deg/sec)
$K28$	rudder pedal feedforward gain, (deg)/(deg)
KST	strake ACC schedule gain, (deg)/(deg)
M	Mach number
n_y	lateral acceleration at sensor location (positive right), g
n_z	normal acceleration at sensor location (positive upward), g
p	roll rate (positive right wing down), deg/sec
$\dot{p}$	roll acceleration, deg/sec^2
q	pitch rate (positive nose up), deg/sec
$\dot{q}$	pitch acceleration, deg/sec^2
r	yaw rate (positive nose right), deg/sec
$\dot{r}$	yaw acceleration, deg/sec^2
s	Laplace transform variable
T	time interval between data samples, sec
u	control input vector
V	true velocity, ft/sec
V_{trim}	true velocity at trim, ft/sec
$XKI1$	pitch axis integral feedforward gain, (deg)/(deg)
$XKI3$	roll axis integral feedforward gain, (deg)/(deg)
$XKP1$	pitch axis proportional feedforward gain, (deg)/(deg/sec)
$XKP3$	roll axis proportional feedforward gain, (deg)/(deg/sec)
x	state vector
y	observation vector
y_{t_c}	sum of all feedbacks, deg/sec
z	discrete transform variable
α	angle of attack (positive nose up), deg
α_{trim}	angle of attack at trim (positive nose up), deg
$\dot{\alpha}$	rate of change of angle of attack (positive nose up), deg/sec
β	angle of sideslip (positive nose left), deg
$\dot{\beta}_{est}$	estimated angle-of-sideslip rate (positive nose left), deg/sec
δ_c	canard position (positive trailing edge down), deg
δ_{df}	differential flap position (positive right wing down), deg
δ_r	rudder surface position (positive trailing edge left), deg
δ_{sf}	symmetric flap position (positive trailing edge down), deg

4

$\delta_{sf_{com}}$	symmetric flap command (positive trailing edge down), deg
δ_{stf}	strake flap position (positive trailing edge down), deg
$\delta_{stf_{des}}$	desired low drag trim strake flap position, deg
θ	pitch attitude (positive nose up), deg
ϕ	bank angle (positive right wing down), deg

Subscripts and Superscripts

$\tilde{\ }$	denotes perturbation quantities
$trim$	denotes steady-state trim values
$\dot{\ }$	denotes time derivative

Operations

| $\dfrac{\partial()}{\partial()}$ | partial differential operation |

PROGRAM DESCRIPTION

The X-29A airplane is an experimental aircraft designed to test the integration of several modern technologies (forward-swept wings, tailored composites, high level of static instability, etc.). In 1977, the X-29A project (Krone, 1980; Sefic and Maxwell, 1986; and Spacht, 1980) was started and funded by the Defense Advanced Research Project Agency (DARPA). The airplane was designed and built by the Grumman Aerospace Corporation, Bethpage, New York. The vehicle is currently being flight-tested by a team composed of NASA, U.S. Air Force, and Grumman personnel at the NASA Dryden Flight Research Facility, Edwards, California.

VEHICLE CHARACTERISTICS

The X-29A airplane is a relatively small, single seat, high-performance aircraft powered by a single F404-GE-400 engine (General Electric, Lynn, Massachusetts). Maximum thrust is approximately 16,000 lb, empty weight is 14,000 lb, and the fuel capacity is 4000 lb. The aircraft dimensions are shown in figure 1. The vehicle incorporates a forward-swept wing with close-coupled canards to provide a low-drag configuration. The airplane physical characteristics are presented in table 1.

The wing structure includes aeroelastically tailored graphite-epoxy covers providing stiffness to overcome the torsional and bending divergence problems associated with forward-swept wings. The wing has a 5-percent-thick supercritical airfoil. Discrete variable camber is provided by full-span trailing-edge flaps.

The aircraft is balanced to be approximately 35 percent statically unstable in the longitudinal axis at the worst case, low dynamic pressure, subsonic flight conditions. Longitudinal stability and control

5

of the aircraft is obtained with active canard, symmetric flap, and strake surfaces (fig. 1). Lateral-directional motion is controlled by conventional rudder and differential flap deflection. The maximum surface deflections and rates are summarized in table 2.

RIGID-BODY AERODYNAMIC MODEL DESCRIPTION

Linear rigid-body aerodynamic models were obtained by solving for a steady-state 1-g trim point, and then using finite differences to approximate the coefficients of the linear equations of motion. The trim point was obtained by using iterative search techniques to find the surface positions, angle of attack, and thrust that resulted in steady-state straight and level flight. With the three-surface longitudinal control, the number of possible trim solutions is infinite; however, the control laws introduce fixed relationships between the surfaces that force a unique solution. These same relationships are incorporated in the trimming algorithm for the linear models. For each combination of surface position, angle of attack, and thrust, the forces and moments were computed using the full six-degree-of-freedom nonlinear equations of motion with a full envelope aerodynamic database derived from wind-tunnel data. For the results presented here, no attempt was made to update the wind-tunnel aerodynamic database with flight test results.

The linear perturbation rigid body equations of motion were formulated in the following state space form:

$$\dot{\tilde{x}} = A\tilde{x} + B\tilde{u}$$
$$\tilde{y} = H\tilde{x} + F\tilde{u}$$

The coefficients in the matrices were obtained by taking numerical perturbations about the trim condition. The perturbation step sizes were ±1 percent of the speed of sound for total velocity, ±2° for angle of attack, and ±1° for the remaining states and control surfaces. These step sizes provided reasonable estimates of the linear coefficients even when the perturbation increment spanned a breakpoint in the aerodynamic tables.

The linear equations were decoupled into longitudinal and lateral-directional axes. For the longitudinal equations $\tilde{x}$, $\tilde{u}$, and $\tilde{y}$ are defined as:

$$\tilde{x} = \begin{bmatrix} \tilde{V} \\ \tilde{\alpha} \\ \tilde{q} \\ \tilde{\theta} \end{bmatrix} \quad \tilde{u} = \begin{bmatrix} \tilde{\delta}_c \\ \tilde{\delta}_{sf} \\ \tilde{\delta}_{stf} \end{bmatrix} \quad \tilde{y} = \begin{bmatrix} \tilde{V} \\ \tilde{\alpha} \\ \tilde{q} \\ \tilde{\theta} \\ \tilde{n}_z \end{bmatrix}$$

6

For the lateral-directional equations $\tilde{x}$, $\tilde{u}$, and $\tilde{y}$ are defined as:

$$\tilde{x} = \begin{bmatrix} \tilde{\beta} \\ \tilde{p} \\ \tilde{r} \\ \tilde{\phi} \end{bmatrix} \quad \tilde{u} = \begin{bmatrix} \tilde{\delta}_{df} \\ \tilde{\delta}_r \end{bmatrix} \quad \tilde{y} = \begin{bmatrix} \tilde{\beta} \\ \tilde{p} \\ \tilde{r} \\ \tilde{\phi} \\ \dot{\tilde{p}} \\ \dot{\tilde{r}} \\ \tilde{n}_y \end{bmatrix}$$

The normal and lateral accelerations are calculated for the sensor locations.

For comparison with flight data, the total values for the states, outputs, and controls were computed by adding the steady-state 1-g trim values to the perturbation quantities as follows:

$$x = \tilde{x} + x_{trim}$$
$$y = \tilde{y} + y_{trim}$$
$$u = \tilde{u} + u_{trim}$$

The trim values were those obtained from the calculated steady-state trim, not those measured in flight.

FLIGHT CONTROL SYSTEM DESCRIPTION

The X-29A airplane has a triplex digital flight control system with an analog backup for each channel. The primary task of the control laws is to stabilize the longitudinal motion of the aircraft. The control laws for the X-29 airplane were updated at a rate of 40 samples/sec (T = 0.025 sec). The system was designed to be operational with a single sensor failure and safe after a second failure. This section presents the dynamic elements of the flight control system that were included in the linear models. Nonlinear elements such as dead bands, rate limits, and position limits were not included in the linear model; therefore, they are not discussed here. A more complete description of the flight control system can be found in Whitaker and Chin (1984). Tabulations of the flight control system gains that are a function of flight condition can be found in Gera, Bosworth, and Cox (1991).

Normal Digital Powered Approach Mode

The normal digital powered approach (ND–PA) flight control system mode is used in the takeoff and landing phases of flight. The dynamic elements included in the longitudinal ND–PA linear model are shown in the block diagram in figure 2. Table 3 presents the s-plane descriptions of the sensor, notch filter, actuator, and computational time delay models. Even though the rigid body aerodynamic model used in the linear models did not include higher frequency structural modes, the notch filters were modeled to account for the time delays associated with their presence in the feedback loops. The canard position sensor was not included since its dynamics were fast enough not to have a noticeable effect in the rigid body frequency range (0.1–50.0 rad/sec). The computational time delay was approximated with a first-order Pade approximation of an average 10-msec time delay in the forward loop.

The longitudinal ND–PA mode incorporates two primary feedback variables: pitch rate and canard position. Each feedback is multiplied by a gain that is a constant independent of flight condition. Pitch rate is the primary stabilizing feedback which is passed through a lead compensation filter. A synthesized pitch acceleration is obtained by differentiating pitch rate which is used at low frequencies. At high frequencies canard position is used as an estimate of pitch acceleration. The estimated pitch acceleration is then combined with the filtered pitch rate to provide the total feedback (y_{t_c} on fig. 2).

The pilot longitudinal stick input is multiplied by a gain and the difference between that and the total feedback is the feedforward command (e on fig. 2). The feedforward command is passed through a proportional-plus-integral compensation filter. This command is sent to the canard and strake flap actuators. The symmetric flaps are held at a constant 20.80° trailing-edge-down position for the ND–PA mode.

The lateral-directional ND–PA linear model is described by the block diagram of figure 3. Table 3 presents the s-plane descriptions of the sensor, notch filter, actuator, and computational time delay models. The lateral-directional ND–PA mode incorporates two feedbacks: roll rate and yaw rate. The yaw rate feedback is passed through a high-pass filter. This mode also includes aileron-to-rudder and rudder-to-aileron crossfeed gains to improve turn coordination.

For the normal digital modes the stick and rudder pedal input units are in percent of full throw. The stick and rudder feel system characteristics are given in table 4.

Normal Digital Up-and-Away Mode

For most of the vehicle flight time the control system is in the normal digital up-and-away (ND–UA) mode. The dynamic elements included in the longitudinal ND–UA linear model are shown in the block diagram in figure 4. Table 3 presents the s-plane description of the sensor, notch, actuator, and computational time delay models.

The longitudinal ND–UA mode is very similar to the longitudinal ND–PA mode with the following differences. The pilot longitudinal stick command is passed through a gain ($GMAX$) which is proportional to the maximum allowed normal acceleration at a given flight condition. Normal acceleration is included as a feedback. The feedback gains, a gain on the pilot input ($G7$), and the proportional-plus-integral gains are scheduled as a function of flight condition. The feedback lead compensation filter coefficients are different from the PA mode. The noise filter on the strake flap actuator command rolls off at higher frequencies than in the ND mode. The symmetric flap is an active controller and the strake path includes a high-pass filter. Slower loops are present, which in steady-state flight move the surfaces to predetermined low-drag automatic camber control (ACC) positions that are a function of flight condition. The ACC surface positions were selected to minimize drag in trimmed flight.

The ACC logic calculates a desired low-drag trim canard position based on Mach number (M), altitude (h), and angle of attack. In the nonlinear simulation the difference between the desired canard position and the canard command is fed through an integrator to the symmetric flap command. The integrator moves the symmetric flaps and the canard moves to negate the resulting pitching moment. Thus, the symmetric flaps move until the desired canard position is achieved.

It was sufficient to assume that changes in flight condition and angle of attack would be small enough to cause insignificant change in the desired trim canard position for the linear time history and frequency response analysis. The integrator in the flap loop is included; however, its input is the perturbation canard command. The result is that following the transient response from the pilot commands, the integrator attempts to force the canard back to its trim value.

The desired low-drag trim strake flap ACC position is a function of Mach number, altitude, and symmetric flap command. In the linear model the Mach number and altitude effects were negligible. The effect of the changing flap command on the ACC strake command is included by calculating the gain KST, which is defined as the following partial derivative:

$$KST = \frac{\partial_{(\delta_{stf_{des}})}}{\partial_{(\delta_{sf_{com}})}}$$

The symmetric flap command is multiplied by this gain and the resulting value (which is the change in desired strake position due to the ACC schedule) is low-pass filtered and added to the strake command.

Figure 5 is a block diagram of the lateral-directional ND–UA mode. Differences between the lateral-directional ND–UA and ND–PA modes will be pointed out in the following discussion. In addition to roll rate and yaw rate the ND–UA mode includes bank angle and lateral acceleration as feedback variables. The lateral acceleration and bank angle sensors were not modeled since they did not significantly affect the response of the linear model in the rigid body frequency range. An estimated angle-of-sideslip rate is calculated using:

$$\dot{\beta}_{est} = -r + 57.3 \left(\frac{g}{V_{trim}} \right) \left(\frac{\phi}{57.3} \right) + p \left(\frac{\alpha_{trim}}{57.3} \right)$$

This feedback is faded in at the higher Mach number and higher altitude flight conditions using the blending function ($BLEND$) which varies from zero to one depending on flight condition. The estimated angle-of-sideslip rate is then passed through a high-pass filter.

The ND–UA lateral-directional mode feedback, crossfeed, rudder pedal, and lateral stick command gains are all scheduled with flight condition. The rudder-to-aileron crossfeed is passed through a high-pass filter, and the forward loop roll command is passed through a proportional-plus-integral filter. These filter coefficients vary with flight condition.

Analog Reversion Mode

The analog reversion (AR) mode was designed as a fail-safe mode to enter in the event of system failures that render the ND modes inoperable. The AR mode is also pilot selectable for flight test purposes. Compared to the ND mode, the relative simplicity of the AR mode makes it easier to analyze and model.

The dynamic elements included in the longitudinal AR mode linear model are shown in the block diagram in figure 6. Table 3 presents the s-plane description of the sensor, notch filter, and actuator models. The longitudinal AR mode utilizes pitch rate as its sole stabilizing feedback variable. The

AR mode includes a second-order lead-lag feedback filter, and proportional-plus-integral feedforward control. The feedforward command is sent to the canard, symmetric flaps, and strake flap surfaces for three-surface active control. The gains for both the AR–PA and AR–UA control laws are found in table 5. In the AR–PA mode the symmetric flap position is fixed at 20.15°.

Figure 7 shows the linear block diagram for the lateral-directional AR mode. Roll rate, high-pass filtered yaw rate feedbacks, as well as aileron-to-rudder and rudder-to-aileron crossfeeds are used for feet-on-the-floor coordinated turns. The lateral-directional gains for both the AR–UA and AR–PA modes are presented in table 5.

SELECTED FLIGHT CONDITIONS

Three specific flight conditions were chosen to represent the X-29A characteristics over its flight envelope. The flight conditions are:

Case 1. Powered Approach, $M = 0.258$ (160 KEAS) at $h = 4,000$ ft
Case 2. Up and Away, $M = 0.70$ at $h = 20,000$ ft
Case 3. Up and Away, $M = 0.90$ at $h = 8,000$ ft

Models are presented for each of these flight conditions for the ND and AR modes and both the longitudinal and lateral-directional axes. The powered approach flight condition was chosen as a representative landing configuration. The landing gear is extended, the symmetric flaps are fixed in the landing configuration, and PA gains are selected. Case 2 was chosen as a middle-of-the-envelope test point and case 3 is near the part of the envelope with the quickest open-loop time-to-double amplitude. The flight control system gains scheduled as a function of flight condition are tabulated for cases 2 and 3 in table 6.

LINEAR MODEL AND FLIGHT DATA COMPARISONS

Both time and frequency domain comparisons are shown for each of the selected flight conditions and control system modes. The flight-measured and predicted steady-state 1-g trim control surface positions and angle of attack are given in table 7. The weights and inertias used in deriving the linear models at each flight condition were obtained by taking the average weight over the pitch, roll, and yaw inputs. These values are found in table 8. The aerodynamic state space models for the three flight conditions and two control modes are given in tables 9–20. The AR and ND mode linearized aerodynamic state space models differ slightly, because the ND mode uses ACC logic to achieve low-drag trim surface positions while the AR mode uses a simpler scheme that results in different trim control surface values and angle of attack.

The normal and lateral accelerations obtained from the state space model are the accelerations at the sensor locations. The sensor locations are given in table 21. Each flight condition has a slightly different center of gravity location because of different fuel loadings. The center of gravity locations are found in table 22.

10

For the ND control modes the continuous part of the linear model is discretized at the sample rate of the digital control system (40 samples/sec, T = 0.025 sec). This discretization is performed with the assumption that there are zero-order holds on all of the inputs to the continuous subsystem (Edwards, 1976). This accounts for the effects of the sample-and-hold devices on the actual vehicle. The discretized continuous subsystem is then combined with the discrete control system and standard linear analysis techniques are applied to calculate the time and frequency domain responses of the linear model. The AR mode is discretized at a rate of 80 samples/sec, which is an approximation of the continuous system.

Time Domain Comparisons

Pitch, roll, and yaw doublets were performed at each flight condition. Figures 8–25 show time domain comparisons of the flight-measured vehicle responses compared with the responses of the linear model. The inputs to the linear model are the flight-measured stick and rudder pedal commands. The time histories show the pilot commands, vehicle states and outputs, and the control surface positions. The total velocity state was not included in the plots because the manuevers did not significantly affect the long-period phugoid mode. In general, the linear model provides a reasonable representation of the flight vehicle. Cases where the linear model failed to predict the aircraft behavior will be discussed in the following section.

The clearest example of unmodeled, nonlinear behavior is apparent in the longitudinal powered approach cases (figs. 8 and 11) in the symmetric flap deflection time histories. For the ND mode the model fixes the flap at 21.8°. In the flight control computers, however, there is logic that moves the flaps to avoid positive canard deflections. This occurs between 1.7 and 2.7 sec as seen in figure 8. For the AR mode (fig. 11) a similar nonlinearity occurs. In this case, the symmetric flap is modeled as an active surface; however, the flight measurements show that it is against its position limit. Therefore, only the negative part of the incremental flap command actually results in a change in surface position. The resulting difference in response is most evident in the angle-of-attack time history of figure 11. To obtain better predictions of the dynamics of the pitch axis PA flight condition would require a model with nonlinear logic for the symmetric flap surface.

The ND–PA longitudinal overplot (fig. 8) shows evidence of an external disturbance. The flight vehicle encountered a gust at the initiation of the maneuver (at approximately 0.9 sec) which caused the angle of attack and normal acceleration to increase even though the initial pilot command was forward on the stick. This unmodeled external input resulted in errors which propagated through the maneuver.

A discrepancy between the linear model and the flight data that is most evident in figures 11 and 20 is the difference between the flight-measured trim angle of attack and trim pitch angle. This indicates that the aircraft was trimmed with a nonzero flightpath angle; however, this should not significantly affect the resulting perturbation dynamics. The other small differences in trim angle-of-attack and surface positions most likely can be attributed to errors in predicted aerodynamic characteristics.

In general, the roll doublets resulted in good matches of the frequency; however, the peak magnitudes were mispredicted. Three examples of this misprediction are the PA configurations of figures 9 and 12, and the ND–UA mode at $M = 0.70$ and $h = 20,000$ ft shown in figure 15. Another example

where the predicted peak magnitudes were less than the flight-measured values is the pitch rate and normal acceleration seen in figure 20 for the ND mode at $M = 0.90$ and $h = 8,000$ ft.

The roll doublets were immediately followed by a yaw doublet. In some cases (see figs. 13, 19, and 25) this meant the yaw maneuver started with some residual roll rate or lateral stick commands. The resulting errors in roll rate were integrated in the linear model and larger errors accumulated in the bank angle traces. In general, because the roll and pitch attitudes in the linear model are calculated by integrating the roll and pitch rates respectively, these time histories will accumulate a gradual drift when compared to flight-measured data. This drift is caused by the accumulation of the errors that result from unmodeled external inputs, such as residual motion and external gusts.

For the yaw doublet inputs, the roll due to rudder pedal command was not well predicted. This is most evident in figures 10 and 16. In general the other parameters matched fairly well.

Frequency Domain Comparisons

Most of the criteria used for the flight control system design of the X-29A airplane were described in frequency domain terms. Stability margins are obtained from the open-loop frequency response, and handling qualities predictions are obtained from lower order equivalent system (Military Specification MIL-F-8785C, 1980) or Neal-Smith analysis (Neal and Smith, 1970) of closed-loop frequency response data. Pilot-generated frequency sweeps and fast Fourier transformation (FFT) techniques (Bosworth and West, 1986; Bosworth, 1989) were used to extract the closed-loop and longitudinal open-loop frequency responses of the vehicle from flight data. A time history of a representative pilot-generated frequency sweep is shown in figure 26. Because of the multiple-input, multiple-output nature of the lateral-directional axis, open-loop frequency responses are presented only for the longitudinal axis. Frequency sweeps were not performed for all of the flight conditions, modes, and axes. However, when available the flight results are presented in comparison with linear predictions in figures 27–44.

The FFT results from flight data generally provided good coherent data from approximately 0.90 to 30.0 rad/sec. The loss of coherence at approximately 30.0 rad/sec (see figs. 34 and 38) causes the gain of the frequency response to approach 0.0 dB. This loss is a result of the lack of high-frequency excitation caused by system attenuation, as well as the physical limits of the speed with which the stick can be moved. Data above 30.0 rad/sec as well as data below approximately 0.90 rad/sec should be ignored.

Generally the frequency responses of the linear models matched the flight data very well. The following discussion will point out areas were the model did not match the flight data.

The flight data on the phase plot of figure 27 are not very smooth and show some sharp changes with frequency. This behavior is usually an indication of nonlinearities in the system and it could be attributed to the flap position limit discussed previously and seen in the time history of figure 11. The large differences seen on the normal acceleration due to longitudinal stick transfer function of figure 29 are also most likely explained by the flap position limit. Since the full-span flaperons have a large effect on the lift and are near the center of gravity, they tend to affect the normal acceleration much more

than the pitch rate of the aircraft. This would explain the good match of the pitch rate transfer function (fig. 28) even in the presence of nonlinear flap motion.

Compared to the linear model in the roll axis the higher peak magnitudes of the flight data are supported by the gain plot of figure 33. The period of excitation of the second doublet on figure 15 is approximately 1.1 sec which corresponds to 5.70 rad/sec. On the amplitude ratio plot of figure 33 the flight data are approximately 1.5 dB higher at 5.70 rad/sec. This agrees with the 20-percent-higher peaks observed on the time history plots in figure 15. It is interesting that both the time history (fig. 18) and frequency response (fig. 37) of the AR mode at the same flight condition do not exhibit the same difference in peak magnitudes.

Another difference that appears in the ND mode and not in the AR mode is the gain shift in the open-loop frequency response of figure 38. This difference does not appear in the AR mode (fig. 42). These discrepancies are perhaps less surprising when it is considered that the AR mode uses different feedback variables and trims at different angle-of-attack and surface positions than the ND mode.

Compared to the flight data, lower damping in the normal acceleration of the linear model can be seen in both the time history (fig. 20) and the frequency response (fig. 40) for the ND mode at $M = 0.90$ and $h = 8,000$ ft.

The AR mode open-loop phase and consequently, the phase margin tend to be lower than predicted in the middle frequency range. This can be seen in the phase plots of figures 34 and 42.

CONCLUDING REMARKS

Linear models of the X-29A aircraft were presented for three flight conditions and two flight control system modes. Sufficient descriptions of the flight control system and the state space representations of the aerodynamics were included so that the linear models could be reproduced by the reader. The purpose was to provide a realistic example of the important elements that contribute to the rigid body dynamics of a complex control configured vehicle.

Flight data comparisons with the linear models demonstrated that these models were representative of the flight test vehicle. Comparisons were made in both the time and frequency domains. Generally, the linear model provided good predictions of the dynamics of the flight vehicle. Of the discrepancies that did appear, some were the result of known nonlinearities in the system. The known nonlinearities involved the symmetric flap command logic for the longitudinal powered approach flight control system mode (PA) cases. These nonlinearities need to be included for accurate simulation of the pitch axis dynamics at this flight condition. Other discrepancies were caused by unmodeled inputs (gusts) and less-than-ideal initial conditions that are typical of flight test data.

There were some differences most likely attributed to misprediction of the aerodynamic state space model. It should be noted that when looking at the combined aircraft–flight control system, differences between predicted and actual aerodynamics tend to be masked by the high-gain flight control system. Indeed, the function of the flight control system designer is to make the vehicle insensitive to anticipated variations of predicted aerodynamic characteristics. Thus the aerodynamic state space models should be

regarded as representative of the X-29A vehicle; however, the limits of their accuracy are not thoroughly documented here.

The longitudinal models provide an example of the stabilization of a vehicle with a very short time-to-double amplitude (approximately 135 msec). These are practical designs which were used in actual flight test of the X-29A vehicle.

Dryden Flight Research Facility
National Aeronautics and Space Administration
Edwards, California, November 15, 1990

REFERENCES

Bauer, J.E., D.B. Crawford, D. Andrisani, and J. Gera, "Real-Time Comparison of X-29A Flight Data and Simulation Data," AIAA-87-0344, Jan. 1987.

Bendat, J.S., and A.G. Piersol, *Random Data: Analysis and Measurement Procedures*, Wiley-Interscience, New York, 1971.

Bosworth, J.T., and J.C. West, "Real-Time Open-Loop Frequency Response Analysis of Flight Test Data," AIAA-86-9738, Apr. 1986.

Bosworth, John T., *Flight-Determined Longitudinal Stability Characteristics of the X-29A Airplane Using Frequency Response Techniques*, NASA TM-4122, 1989.

Edwards, John W., *A Fortran Program for the Analysis of Linear Continuous and Sampled-Data Systems*, NASA TM X-56038, 1976.

Gera, Joseph, *Dynamics and Controls Flight Testing of the X-29A Airplane*, NASA TM-86803, 1986.

Gera, Joseph, and John T. Bosworth, "Dynamic Stability and Handling Qualities Tests on a Highly Augmented, Statically Unstable Airplane," paper in the proceedings of the 18th Annual Symposium of the Society of Flight Test Engineers, 1987, pp. 2-1–2-13.

Gera, J., J.T. Bosworth, and T.H. Cox, *X-29A Flight Test Techniques and Results: Flight Controls*, NASA TP-3121, 1991.

Kempel, Robert W., and Michael R. Earls, *Flight Control Systems Development and Flight Test Experience With the HiMAT Research Vehicles*, NASA TP-2822, 1988.

Krone, N.J., Jr., "Forward Swept Wing Flight Demonstrator," AIAA-80-1882, Aug. 1980.

Military Specification: "Flying Qualities of Piloted Airplanes," MIL-F-8785C, Nov. 1980.

Neal, T.P., and R.E. Smith, *An In-Flight Investigation to Develop Control System Design Criteria for Fighter Airplanes, Volume I*, AFFDL-TR-70-74, Dec. 1970.

Sefic, Walter J., and Cleo M. Maxwell, *X-29A Technology Demonstrator Flight Test Program Overview*, NASA TM-86809, 1986.

Spacht, G., "The Forward Swept Wing: a Unique Design Challenge," AIAA-80-1885, Aug. 1980.

Whitaker, A.B., and J. Chin, "X-29 Digital Flight Control System Design," *Active Control Systems- Review, Evaluation and Projections*, AGARD-CP-384, 1984, pp. 6-1–6-13.

TABLES

Table 1. X-29A physical characteristics.

Wing span, ft	27.2
Wing area, ft^2	185
Wing leading-edge sweep (forward), deg	29.3
Mean aerodynamic chord, ft	7.2
Vehicle empty weight, lb	14,000
Maximum fuel capacity, lb	4,000
Canard area, ft^2	37

Table 2. X-29A control surface characteristics.

Control surface	Position limit, deg	Rate limit, deg/sec
Canard	−60, 30	±100
Symmetric flap	−10, 25	± 70
Strake flap	−30, 30	± 30
Differential flap	−17.5, 17.5	± 70
Rudder	−30, 30	±125

Table 3. s-plane description of continuous dynamic elements.

Dynamic element	s-plane description
Canard actuator	$\dfrac{(0.885)(20.2)(71.4)^2(144.9)}{(s+20.2)[s^2+2(0.736)(71.4)s+(71.4)^2](s+144.9)}$
Symmetric flap actuator	$\dfrac{(20.2)(71.4)^2(144.9)}{(s+20.2)[s^2+2(0.736)(71.4)s+(71.4)^2](s+144.9)}$
Strake actuator	$\dfrac{(50)(100)(325)^2}{(s+50)(s+100)[s^2+2(0.7)(325)s+(325)^2]}$
Differential flap actuator	$\dfrac{(54.1)^2(71.4)^2}{[s^2+2(1.53)(54.1)s+(54.1)^2][s^2+2(0.735)(71.4)s+(71.4)^2]}$
Rudder actuator	$\dfrac{(54.1)^2(71.4)^2}{[s^2+2(1.53)(54.1)s+(54.1)^2][s^2+2(0.735)(71.4)s+(71.4)^2]}$
Time delay	$\dfrac{100}{s+100}$
Pitch rate fuselage vertical bending notch filter	$\dfrac{s^2+2(0.2)(68)s+(68)^2}{s^2+2(0.5)(68)s+(68)^2}$
Pitch rate fuselage second vertical bending notch filter	$\left[\dfrac{120}{133}\right]^2 \dfrac{s^2+2(0.05)(133)s+(133)^2}{s^2+2(0.50)(120)s+(120)^2}$
Pitch rate fuselage second vertical bending– wing second bending notch filter	$\left[\dfrac{160}{150}\right]^2 \dfrac{s^2+2(0.071)(150)s+(150)^2}{s^2+2(0.70)(160)s+(160)^2}$
Yaw rate fuselage lateral bending notch filter	$\dfrac{s^2+2(0.1)(70)s+(70)^2}{s^2+2(0.7)(70)s+(70)^2}$
Normal acceleration fuselage vertical bending notch filter	$\dfrac{s^2+2(0.1)(70)s+(70)^2}{s^2+2(0.7)(70)s+(70)^2}$
Normal acceleration noseboom vertical bending– canard pitch–fuselage second vertical bending notch filter	$\left[\dfrac{150}{128}\right]^2 \dfrac{s^2+2(0.10)(128)s+(128)^2}{s^2+2(0.70)(150)s+(150)^2}$
Lateral acceleration fuselage lateral bending notch filter	$\dfrac{s^2+2(0.1)(68)s+(68)^2}{s^2+2(0.5)(68)s+(68)^2}$
Canard position fuselage vertical bending notch filter	$\dfrac{s^2+2(0.14)(68)s+(68)^2}{s^2+2(0.70)(68)s+(68)^2}$
Pitch rate gyro	$\dfrac{(137)^2}{s^2+2(0.704)(137)s+(137)^2}$
Roll rate gyro	$\dfrac{(157)^2}{s^2+2(0.701)(157)s+(157)^2}$
Yaw rate gyro	$\dfrac{(137)^2}{s^2+2(0.704)(137)s+(137)^2}$

Table 4. Stick and rudder pedal feel system characteristics.

Control effector	Longitudinal stick	Lateral stick	Rudder pedal
Displacements, in.	+6.0 aft −4.0 fore	±3.2	±3.2
Gradient, lb/in.	4	2	20
Dead band	±1 percent of 6.0 in.	±1 percent of 3.2 in.	±1 percent of 3.2 in.
Transfer function	$\dfrac{0.25(18.4)^2}{s^2 + 2(0.707)(18.4)s + (18.4)^2}$	$\dfrac{0.5(13.1)^2}{s^2 + 2(0.707)(13.1)s + (13.1)^2}$	$\dfrac{0.05(37.5)^2}{s^2 + 2(0.900)(37.5)s + (37.5)^2}$

Table 5. AR mode control system gains.

Gain	UA mode	PA mode
K_c	2.0	8.0
K_{cc}	1.103 (case 2) 0.515 (case 3)	0.49
K_I	2.75	1.9
K_{FI}	−0.4	−0.8
K_{cs}	−0.65	−0.65
K_q	1.25	4.0
a	100	20
K_{ARI}	0.25	0.25
K_{RAI}	−0.25	−0.25
K_{RI}	0.65	3.0
K_P	0.06	0.15
K_{RP}	3.125	7.8125
K_{LS}	2.75	3.75

Table 6. ND mode control system gains for selected cases.

Gain	Case 2. $M = 0.70$, $h = 20,000$ ft	Case 3. $M = 0.90$, $h = 8,000$ ft
$BLEND$	0.5	1.0
$BMAX$, (deg)/(percent)	-14.16	-7.159
$C1$	5.239	3.776
$C2$	-5.169	-3.737
$C3$	-0.9301	-0.9609
$G1$, (rad/sec)/(g)	0.005389	0.04452
$G2$, (deg/sec)/(deg/sec)	-3.602	-3.216
$G3$, (deg/sec)/(deg/sec^2)	-0.1838	-0.2140
$G7$, (rad)/(g)	3.540	1.939
$G8$, (deg/sec^2)/(deg)	16.65	55.93
$GMAX$, (g)/(percent)	5.2	5.4
Gp, (deg/sec)/(percent)	80.18	90.17
$K2$, (deg/sec)/(deg/sec)	-1.175	-1.000
$K3$, (deg/sec)/(deg/sec)	-2.917	-3.000
$K4$, (deg/sec)/(g)	4.163	0.000
$K13$, (deg/sec)/(deg/sec)	1.175	1.000
$K14$, (deg/sec)/(percent)	11.75	10.00
$K16$, (deg)/(deg/sec)	0.000	0.000
$K17$, (deg)/(deg/sec)	0.8401	0.4896
$K18$, (deg)/(g)	0.000	0.000
$K27$, (deg)/(deg/sec)	-0.007544	0.01679
$K28$, (deg)/(deg)	1.000	1.000
KST, (deg)/(deg)	-0.1427	0.1359
$XKI1$, (deg)/(deg)	1.000	1.000
$XKI3$, (deg)/(deg)	0.07583	0.1116
$XKP1$, (deg)/(deg/sec)	0.2309	0.1182
$XKP3$, (deg)/(deg/sec)	0.02934	0.01568

Table 7. 1-g trim angle-of-attack and surface position values.

Mach number	Altitude, ft	Control system mode	True velocity, ft/sec	Angle of attack, deg	Canard position, deg	Symmetric flap position, deg	Strake flap position, deg
0.258	4,000	ND–PA	284	8.60	-6.55	21.80	-11.20
0.258	4,000	AR–PA	284	8.48	-6.91	20.15	-10.93
0.70	20,000	ND–UA	726	4.10	-2.93	0.87	-3.87
0.70	20,000	AR–UA	726	3.46	-0.04	1.90	0.00
0.90	8,000	ND–UA	977	2.80	-3.18	-3.05	-3.13
0.90	8,000	AR–UA	977	2.10	-0.04	-0.41	0.00

Table 8. Weight and inertia characteristics.

Mach number	Altitude, ft	Control system mode	Weight, lb	I_{xx} lb ft s^2	I_{yy} lb ft s^2	I_{zz} lb ft s^2	I_{xz} lb ft s^2
0.258	4,000	ND–PA	15,274	4,609	52,864	55,823	2,465
0.258	4,000	AR–PA	14,777	4,597	52,805	55,754	2,468
0.70	20,000	ND–UA	17,429	4,633	51,411	54,524	1,896
0.70	20,000	AR–UA	17,080	4,630	50,990	54,098	1,963
0.90	8,000	ND–UA	16,379	4,604	50,262	53,366	1,886
0.90	8,000	AR–UA	15,779	4,542	49,949	53,094	1,869

Table 9. Longitudinal state space matrices for ND–PA mode at $M = 0.258$ and $h = 4,000$ ft.

A Matrix (4x4)			
−0.4272E−01	−0.8541E+01	−0.4451E+00	−0.3216E+02
−0.7881E−03	−0.5291E+00	0.9896E+00	0.1639E−09
0.4010E−03	0.3542E+01	−0.2228E+00	0.6150E−08
0.0000E+00	0.0000E+00	0.1000E+01	0.0000E+00

B Matrix (4x3)		
−0.3385E−01	−0.9386E−01	0.4888E−02
−0.1028E−02	−0.1297E−02	−0.4054E−03
0.2718E−01	−0.5744E−02	−0.1351E−01
0.0000E+00	0.0000E+00	0.0000E+00

H Matrix (5x4)			
0.1000E+01	0.0000E+00	0.0000E+00	0.0000E+00
0.0000E+00	0.5730E+02	0.0000E+00	0.0000E+00
0.0000E+00	0.0000E+00	0.5730E+02	0.0000E+00
0.0000E+00	0.0000E+00	0.0000E+00	0.5730E+02
0.7063E−02	0.4567E+01	0.9867E−01	−0.3809E−04

F Matrix (5x3)		
0.0000E+00	0.0000E+00	0.0000E+00
0.0000E+00	0.0000E+00	0.0000E+00
0.0000E+00	0.0000E+00	0.0000E+00
0.0000E+00	0.0000E+00	0.0000E+00
0.8378E−02	0.1192E−01	0.3889E−02

Table 10. Lateral-directional state space matrices for ND–PA mode at $M = 0.258$ and $h = 4,000$ ft.

A Matrix (4x4)			
−0.1817E+00	0.1496E+00	−0.9825E+00	0.1119E+00
−0.3569E+01	−0.1704E+01	0.9045E+00	−0.5531E−06
0.1218E+01	−0.8208E−01	−0.1826E+00	−0.4630E−07
0.0000E+00	0.1000E+01	0.1513E+00	0.0000E+00

B Matrix (4x2)	
−0.4327E−03	0.3901E−03
0.3713E+00	0.5486E−01
0.2648E−01	−0.1353E−01
0.0000E+00	0.0000E+00

H Matrix (7x4)			
0.5730E+02	0.0000E+00	0.0000E+00	0.0000E+00
0.0000E+00	0.5730E+02	0.0000E+00	0.0000E+00
0.0000E+00	0.0000E+00	0.5730E+02	0.0000E+00
0.0000E+00	0.0000E+00	0.0000E+00	0.5730E+02
−0.2045E+03	−0.9763E+02	0.5182E+02	−0.3169E−04
0.6977E+02	−0.4703E+01	−0.1046E+02	−0.2653E−05
−0.1532E+01	0.5293E−01	0.3381E−01	−0.2518E−03

F Matrix (7x2)	
0.0000E+00	0.0000E+00
0.0000E+00	0.0000E+00
0.0000E+00	0.0000E+00
0.0000E+00	0.0000E+00
0.2127E+02	0.3143E+01
0.1517E+01	−0.7751E+00
−0.1551E−01	0.2188E−02

Table 11. Longitudinal state space matrices for AR–PA mode at M = 0.258 and h = 4,000 ft.

A Matrix (4x4)			
−0.4251E−01	−0.8019E+01	−0.4538E+00	−0.3216E+02
−0.7889E−03	−0.5482E+00	0.9893E+00	0.1812E−09
0.3910E−03	0.3604E+01	−0.2221E+00	0.6564E−08
0.0000E+00	0.0000E+00	0.1000E+01	0.0000E+00

B Matrix (4x3)		
−0.3430E−01	−0.9217E−01	0.4827E−02
−0.1065E−02	−0.1337E−02	−0.4219E−03
0.2734E−01	−0.5587E−02	−0.1336E−01
0.0000E+00	0.0000E+00	0.0000E+00

H Matrix (5x4)			
0.1000E+01	0.0000E+00	0.0000E+00	0.0000E+00
0.0000E+00	0.5730E+02	0.0000E+00	0.0000E+00
0.0000E+00	0.0000E+00	0.5730E+02	0.0000E+00
0.0000E+00	0.0000E+00	0.0000E+00	0.5730E+02
0.7069E−02	0.4735E+01	0.1015E+00	−0.3757E−04

F Matrix (5x3)		
0.0000E+00	0.0000E+00	0.0000E+00
0.0000E+00	0.0000E+00	0.0000E+00
0.0000E+00	0.0000E+00	0.0000E+00
0.0000E+00	0.0000E+00	0.0000E+00
0.8728E−02	0.1225E−01	0.4018E−02

Table 12. Lateral-directional state space matrices for AR–PA mode at $M = 0.258$ and $h = 4,000$ ft.

A Matrix (4x4)			
−0.1850E+00	0.1475E+00	−0.9825E+00	0.1120E+00
−0.3467E+01	−0.1710E+01	0.9029E+00	−0.5843E−06
0.1174E+01	−0.8248E−01	−0.1826E+00	−0.4428E−07
0.0000E+00	0.1000E+01	0.1492E+00	0.0000E+00

B Matrix (4x2)	
−0.4470E−03	0.4020E−03
0.3715E+00	0.5488E−01
0.2653E−01	−0.1351E−01
0.0000E+00	0.0000E+00

H Matrix (7x4)			
0.5730E+02	0.0000E+00	0.0000E+00	0.0000E+00
0.0000E+00	0.5730E+02	0.0000E+00	0.0000E+00
0.0000E+00	0.0000E+00	0.5730E+02	0.0000E+00
0.0000E+00	0.0000E+00	0.0000E+00	0.5730E+02
−0.1987E+03	−0.9798E+02	0.5173E+02	−0.3348E−04
0.6727E+02	−0.4726E+01	−0.1046E+02	−0.2537E−05
−0.1563E+01	0.5221E−01	0.3585E−01	−0.2519E−03

F Matrix (7x2)	
0.0000E+00	0.0000E+00
0.0000E+00	0.0000E+00
0.0000E+00	0.0000E+00
0.0000E+00	0.0000E+00
0.2129E+02	0.3145E+01
0.1520E+01	−0.7738E+00
−0.1553E−01	0.2290E−02

Table 13. Longitudinal state space matrices for ND–UA mode at M = 0.70 and h = 20,000 ft.

A Matrix (4x4)			
−0.1170E−01	−0.6050E+01	−0.3139E+00	−0.3211E+02
−0.1400E−03	−0.8167E+00	0.9940E+00	0.2505E−10
0.3213E−03	0.1214E+02	−0.4136E+00	0.3347E−08
0.0000E+00	0.0000E+00	0.1000E+01	0.0000E+00

B Matrix (4x3)			
−0.6054E−01	−0.1580E+00	0.1338E−01	
−0.8881E−03	−0.3604E−02	−0.5869E−03	
0.1345E+00	−0.8383E−01	−0.4689E−01	
0.0000E+00	0.0000E+00	0.0000E+00	

H Matrix (5x4)			
0.1000E+01	0.0000E+00	0.0000E+00	0.0000E+00
0.0000E+00	0.5730E+02	0.0000E+00	0.0000E+00
0.0000E+00	0.0000E+00	0.5730E+02	0.0000E+00
0.0000E+00	0.0000E+00	0.0000E+00	0.5730E+02
0.3158E−02	0.1785E+02	0.1551E+00	−0.1268E−03

F Matrix (5x3)			
0.0000E+00	0.0000E+00	0.0000E+00	
0.0000E+00	0.0000E+00	0.0000E+00	
0.0000E+00	0.0000E+00	0.0000E+00	
0.0000E+00	0.0000E+00	0.0000E+00	
0.1407E−01	0.8523E−01	0.1529E−01	

Table 14. Lateral-directional state space matrices for ND–UA mode at $M = 0.70$ and $h = 20,000$ ft.

A Matrix (4x4)			
−0.1596E+00	0.7150E−01	−0.9974E+00	0.4413E−01
−0.1520E+02	−0.2602E+01	0.1106E+01	0.0000E+00
0.6840E+01	−0.1026E+00	−0.6375E−01	0.0000E+00
0.0000E+00	0.1000E+01	0.7168E−01	0.0000E+00

B Matrix (4x2)			
−0.5980E−03	0.6718E−03		
0.1343E+01	0.2345E+00		
0.8974E−01	−0.7097E−01		
0.0000E+00	0.0000E+00		

H Matrix (7x4)			
0.5730E+02	0.0000E+00	0.0000E+00	0.0000E+00
0.0000E+00	0.5730E+02	0.0000E+00	0.0000E+00
0.0000E+00	0.0000E+00	0.5730E+02	0.0000E+00
0.0000E+00	0.0000E+00	0.0000E+00	0.5730E+02
−0.8709E+03	−0.1491E+03	0.6334E+02	0.0000E+00
0.3919E+03	−0.5878E+01	−0.3652E+01	0.0000E+00
−0.3385E+01	0.9357E−01	−0.3499E−01	−0.1769E−02

F Matrix (7x2)			
0.0000E+00	0.0000E+00		
0.0000E+00	0.0000E+00		
0.0000E+00	0.0000E+00		
0.0000E+00	0.0000E+00		
0.7695E+02	0.1344E+02		
0.5142E+01	−0.4066E+01		
−0.6342E−01	0.1029E−01		

Table 15. Longitudinal state space matrices for AR–UA mode at $M = 0.70$ and $h = 20,000$ ft.

A Matrix (4x4)			
−0.1233E−01	−0.5665E+01	−0.2702E+00	−0.3211E+02
−0.1370E−03	−0.8417E+00	0.9938E+00	0.2667E−10
0.7248E−03	0.1357E+02	−0.4111E+00	0.3494E−08
0.0000E+00	0.0000E+00	0.1000E+01	0.0000E+00

B Matrix (4x3)		
−0.1508E+00	−0.1600E+00	−0.8774E−02
−0.8211E−03	−0.3599E−02	−0.5489E−03
0.1357E+00	−0.8028E−01	−0.4549E−01
0.0000E+00	0.0000E+00	0.0000E+00

H Matrix (5x4)			
0.1000E+01	0.0000E+00	0.0000E+00	0.0000E+00
0.0000E+00	0.5730E+02	0.0000E+00	0.0000E+00
0.0000E+00	0.0000E+00	0.5730E+02	0.0000E+00
0.0000E+00	0.0000E+00	0.0000E+00	0.5730E+02
0.3076E−02	0.1842E+02	0.1562E+00	−0.1070E−03

F Matrix (5x3)		
0.0000E+00	0.0000E+00	0.0000E+00
0.0000E+00	0.0000E+00	0.0000E+00
0.0000E+00	0.0000E+00	0.0000E+00
0.0000E+00	0.0000E+00	0.0000E+00
0.1319E−01	0.8466E−01	0.1425E−01

26

Table 16. Lateral-directional state space matrices for AR–UA mode at $M = 0.70$ and $h = 20,000$ ft.

A Matrix (4x4)			
−0.1645E+00	0.6030E−01	−0.9982E+00	0.4416E−01
−0.1655E+02	−0.2590E+01	0.9970E+00	0.0000E+00
0.6779E+01	−0.1023E+00	−0.6730E−01	0.0000E+00
0.0000E+00	0.1000E+01	0.6041E−01	0.0000E+00

B Matrix (4x2)	
−0.6141E−03	0.6866E−03
0.1347E+01	0.2365E+00
0.9194E−01	−0.7056E−01
0.0000E+00	0.0000E+00

H Matrix (7x4)			
0.5730E+02	0.0000E+00	0.0000E+00	0.0000E+00
0.0000E+00	0.5730E+02	0.0000E+00	0.0000E+00
0.0000E+00	0.0000E+00	0.5730E+02	0.0000E+00
0.0000E+00	0.0000E+00	0.0000E+00	0.5730E+02
−0.9481E+03	−0.1484E+03	0.5712E+02	0.0000E+00
0.3884E+03	−0.5864E+01	−0.3856E+01	0.0000E+00
−0.3434E+01	0.9077E−01	−0.3062E−01	−0.1770E−02

F Matrix (7x2)	
0.0000E+00	0.0000E+00
0.0000E+00	0.0000E+00
0.0000E+00	0.0000E+00
0.0000E+00	0.0000E+00
0.7715E+02	0.1355E+02
0.5268E+01	−0.4043E+01
−0.6261E−01	0.1044E−01

Table 17. Longitudinal state space matrices for ND–UA mode at $M = 0.90$ and $h = 8,000$ ft.

A Matrix (4x4)			
−0.5329E−01	−0.1290E+02	−0.4938E+00	−0.3215E+02
−0.1712E−03	−0.2241E+01	0.9897E+00	0.8203E−10
−0.9569E−03	0.4474E+02	−0.9024E+00	0.1676E−07
0.0000E+00	0.0000E+00	0.1000E+01	0.0000E+00

B Matrix (4x3)		
−0.2138E+00	0.1213E+00	0.7779E−02
−0.2852E−02	−0.6017E−02	−0.9029E−03
0.4720E+00	−0.2499E+00	−0.7966E−01
0.0000E+00	0.0000E+00	0.0000E+00

H Matrix (5x4)			
0.1000E+01	0.0000E+00	0.0000E+00	0.0000E+00
0.0000E+00	0.5730E+02	0.0000E+00	0.0000E+00
0.0000E+00	0.0000E+00	0.5730E+02	0.0000E+00
0.0000E+00	0.0000E+00	0.0000E+00	0.5730E+02
0.5311E−02	0.6650E+02	0.3449E+00	−0.3093E−04

F Matrix (5x3)		
0.0000E+00	0.0000E+00	0.0000E+00
0.0000E+00	0.0000E+00	0.0000E+00
0.0000E+00	0.0000E+00	0.0000E+00
0.0000E+00	0.0000E+00	0.0000E+00
0.7090E−01	0.1907E+00	0.3006E−01

Table 18. Lateral-directional state space matrices for ND–UA mode at M = 0.90 and h = 8,000 ft.

A Matrix (4x4)			
−0.3326E+00	0.4881E−01	−0.9988E+00	0.3287E−01
−0.5313E+02	−0.6638E+01	0.1962E+01	0.0000E+00
0.1447E+02	−0.2383E+00	−0.1050E+00	0.0000E+00
0.0000E+00	0.1000E+01	0.4887E−01	0.0000E+00

B Matrix (4x2)	
−0.1726E−02	0.1099E−02
0.2382E+01	0.5309E+00
0.1591E+00	−0.1470E+00
0.0000E+00	0.0000E+00

H Matrix (7x4)			
0.5730E+02	0.0000E+00	0.0000E+00	0.0000E+00
0.0000E+00	0.5730E+02	0.0000E+00	0.0000E+00
0.0000E+00	0.0000E+00	0.5730E+02	0.0000E+00
0.0000E+00	0.0000E+00	0.0000E+00	0.5730E+02
−0.3044E+04	−0.3803E+03	0.1124E+03	0.0000E+00
0.8292E+03	−0.1365E+02	−0.6014E+01	0.0000E+00
−0.8760E+01	0.2351E+00	−0.6367E−01	−0.6329E−03

F Matrix (7x2)	
0.0000E+00	0.0000E+00
0.0000E+00	0.0000E+00
0.0000E+00	0.0000E+00
0.0000E+00	0.0000E+00
0.1365E+03	0.3042E+02
0.9115E+01	−0.8422E+01
−0.1392E+00	0.2005E−01

Table 19. Longitudinal state space matrices for AR–UA mode at $M = 0.90$ and $h = 8,000$ ft.

A Matrix (4x4)			
−0.5589E−01	0.9805E+00	−0.3856E+00	−0.3215E+02
−0.1177E−03	−0.2281E+01	0.9893E+00	0.9186E−10
−0.7405E−03	0.4579E+02	−0.8958E+00	0.1808E−07
0.0000E+00	0.0000E+00	0.1000E+01	0.0000E+00

B Matrix (4x3)		
−0.4575E+00	0.1448E−01	−0.2400E−01
−0.2737E−02	−0.6476E−02	−0.7625E−03
0.4866E+00	−0.2384E+00	−0.8361E−01
0.0000E+00	0.0000E+00	0.0000E+00

H Matrix (5x4)			
0.1000E+01	0.0000E+00	0.0000E+00	0.0000E+00
0.0000E+00	0.5730E+02	0.0000E+00	0.0000E+00
0.0000E+00	0.0000E+00	0.5730E+02	0.0000E+00
0.0000E+00	0.0000E+00	0.0000E+00	0.5730E+02
0.3660E−02	0.6787E+02	0.3533E+00	−0.2327E−04

F Matrix (5x3)		
0.0000E+00	0.0000E+00	0.0000E+00
0.0000E+00	0.0000E+00	0.0000E+00
0.0000E+00	0.0000E+00	0.0000E+00
0.0000E+00	0.0000E+00	0.0000E+00
0.6895E−01	0.2036E+00	0.2568E−01

30

Table 20. Lateral-directional state space matrices for AR–UA mode at $M = 0.90$ and $h = 8{,}000$ ft.

A Matrix (4x4)			
−0.3498E+00	0.3673E−01	−0.9993E+00	0.3289E−01
−0.5620E+02	−0.6673E+01	0.1648E+01	0.0000E+00
0.1504E+02	−0.2302E+00	−0.1188E+00	0.0000E+00
0.0000E+00	0.1000E+01	0.3675E−01	0.0000E+00

B Matrix (4x2)	
−0.1809E−02	0.1142E−02
0.2387E+01	0.5441E+00
0.1557E+00	−0.1462E+00
0.0000E+00	0.0000E+00

H Matrix (7x4)			
0.5730E+02	0.0000E+00	0.0000E+00	0.0000E+00
0.0000E+00	0.5730E+02	0.0000E+00	0.0000E+00
0.0000E+00	0.0000E+00	0.5730E+02	0.0000E+00
0.0000E+00	0.0000E+00	0.0000E+00	0.5730E+02
−0.3220E+04	−0.3823E+03	0.9444E+02	0.0000E+00
0.8616E+03	−0.1319E+02	−0.6806E+01	0.0000E+00
−0.9185E+01	0.2299E+00	−0.5163E−01	−0.6332E−03

F Matrix (7x2)	
0.0000E+00	0.0000E+00
0.0000E+00	0.0000E+00
0.0000E+00	0.0000E+00
0.0000E+00	0.0000E+00
0.1368E+03	0.3118E+02
0.8921E+01	−0.8379E+01
−0.1393E+00	0.2079E−01

Table 21. Accelerometer locations.

Accelerometer	Wing station, in.	Buttock line, in.	Waterline, in.
Normal	463.00	2.50	52.5
Lateral	462.75	4.25	52.0

Table 22. Center of gravity location for selected cases.

Mach number	Altitude, ft	Control system mode	Wing station, in.	Buttock line, in.	Waterline, in.
0.258	4,000	ND–PA	452.33	0.0	63.41
0.258	4,000	AR–PA	452.74	0.0	63.32
0.70	20,000	ND–UA	445.62	0.0	65.21
0.70	20,000	AR–UA	447.13	0.0	64.91
0.90	8,000	ND–UA	449.98	0.0	65.22
0.90	8,000	AR–UA	451.40	0.0	64.91

Canard

Wing flap

Strake flap

48 ft 1 in.

Rudder

F-5A nose
section

14 ft
9.5 in.

27 ft 2.44 in.
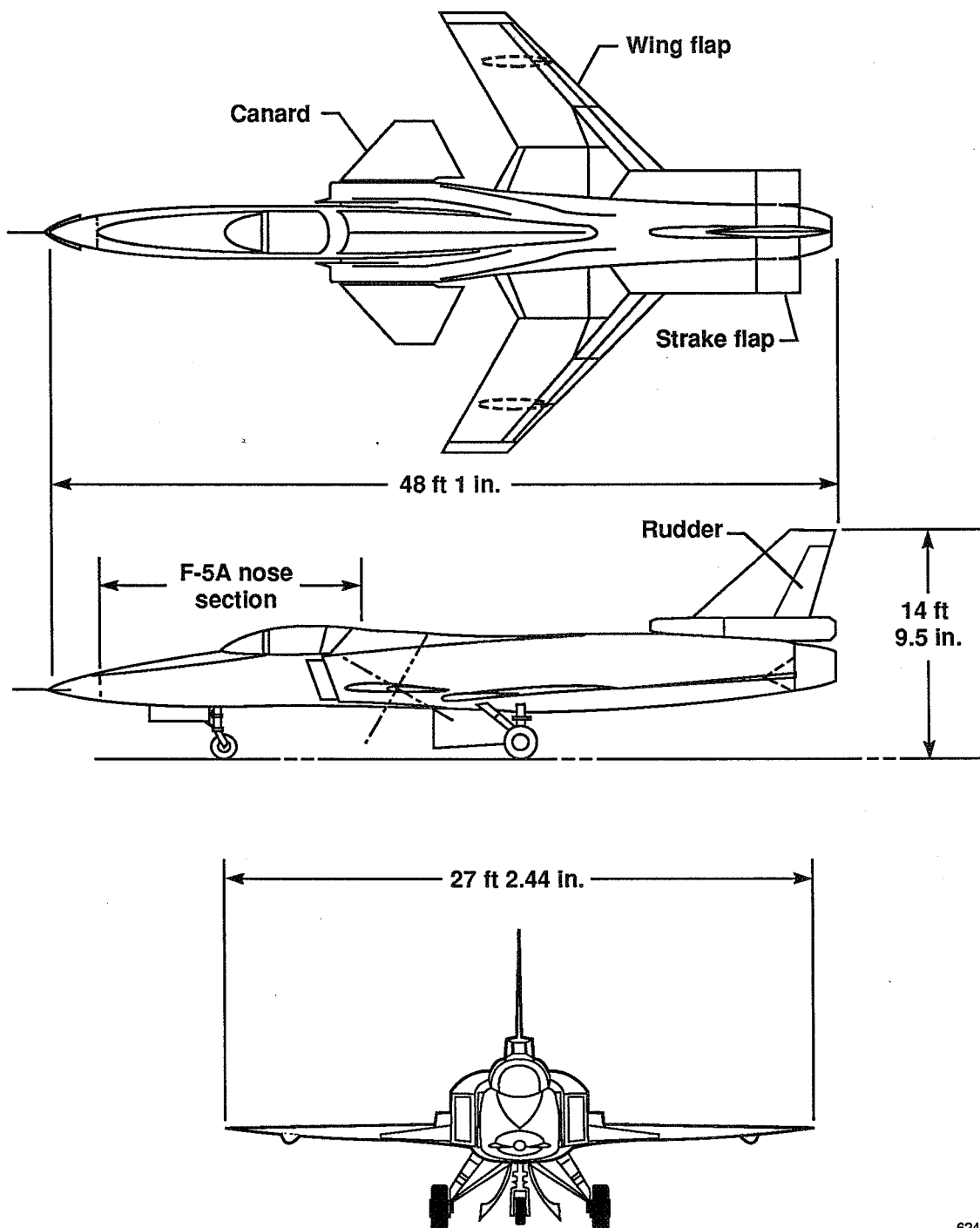
6247

Figure 1. X-29A airplane.
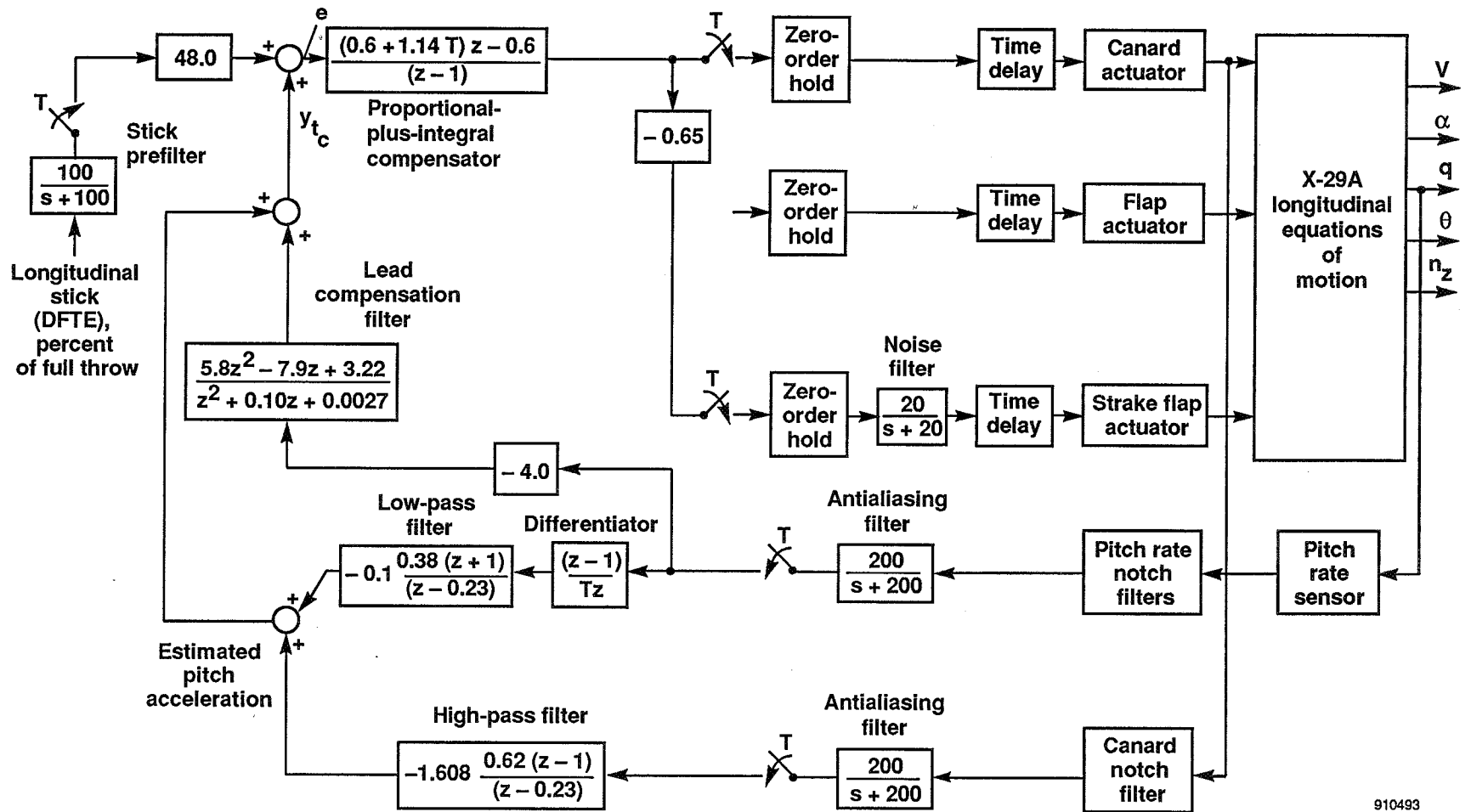
Figure 2. Longitudinal ND mode for powered approach flight.
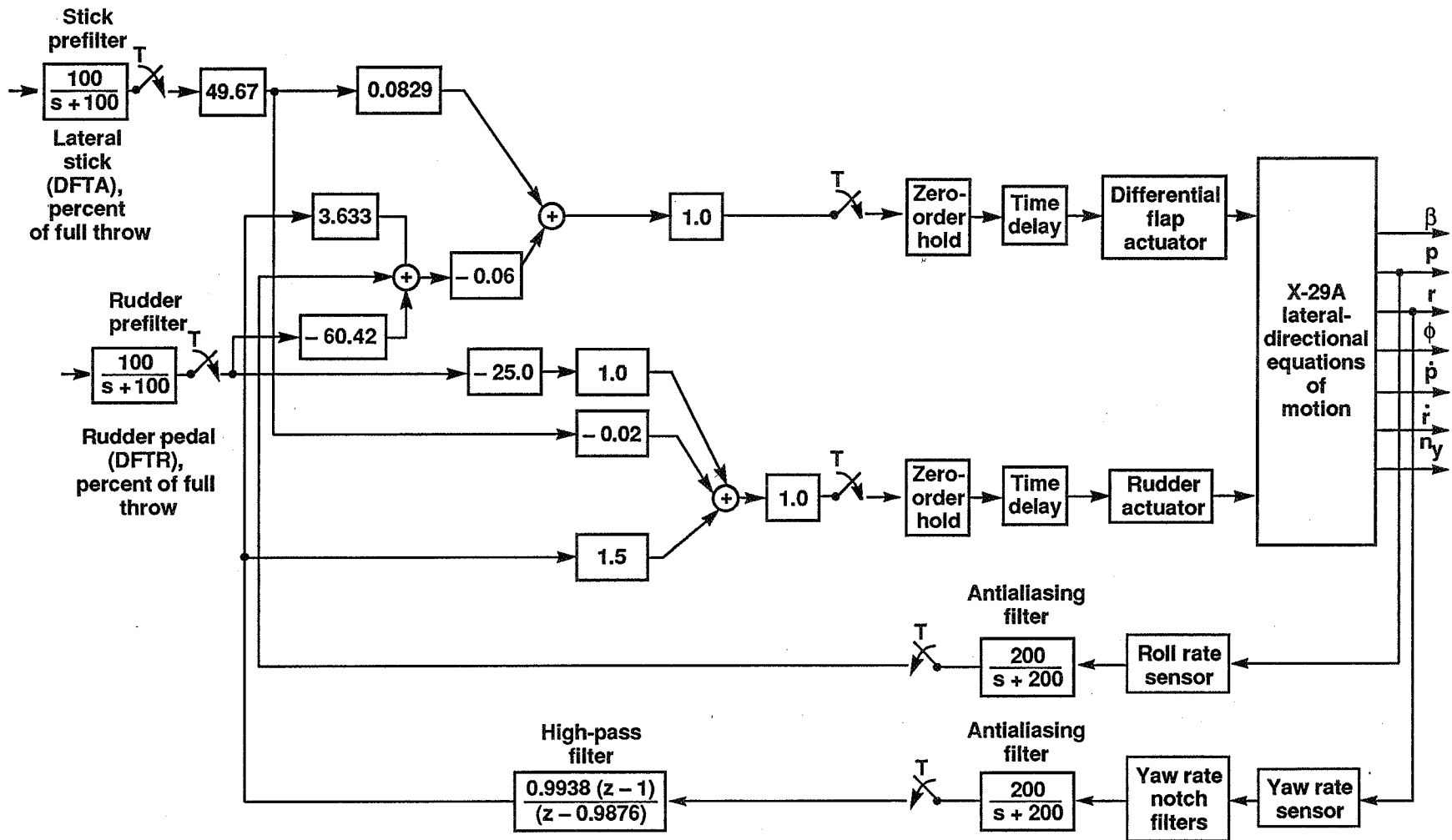
Figure 3. Lateral-directional ND mode for powered approach flight.
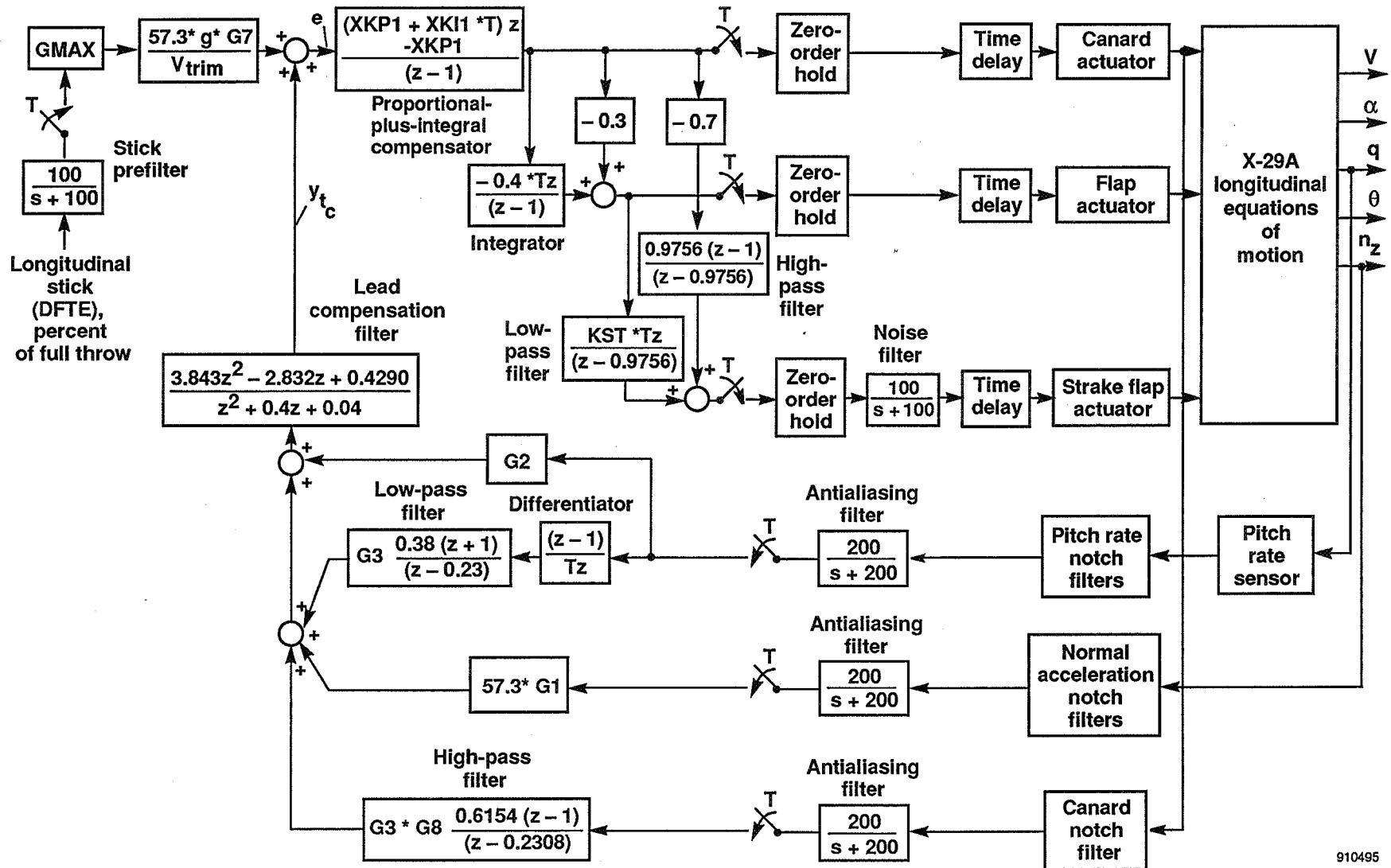
910494

Figure 4. Longitudinal ND mode for up-and-away flight.

910495

Figure 5. Lateral-directional ND mode for up-and-away flight.
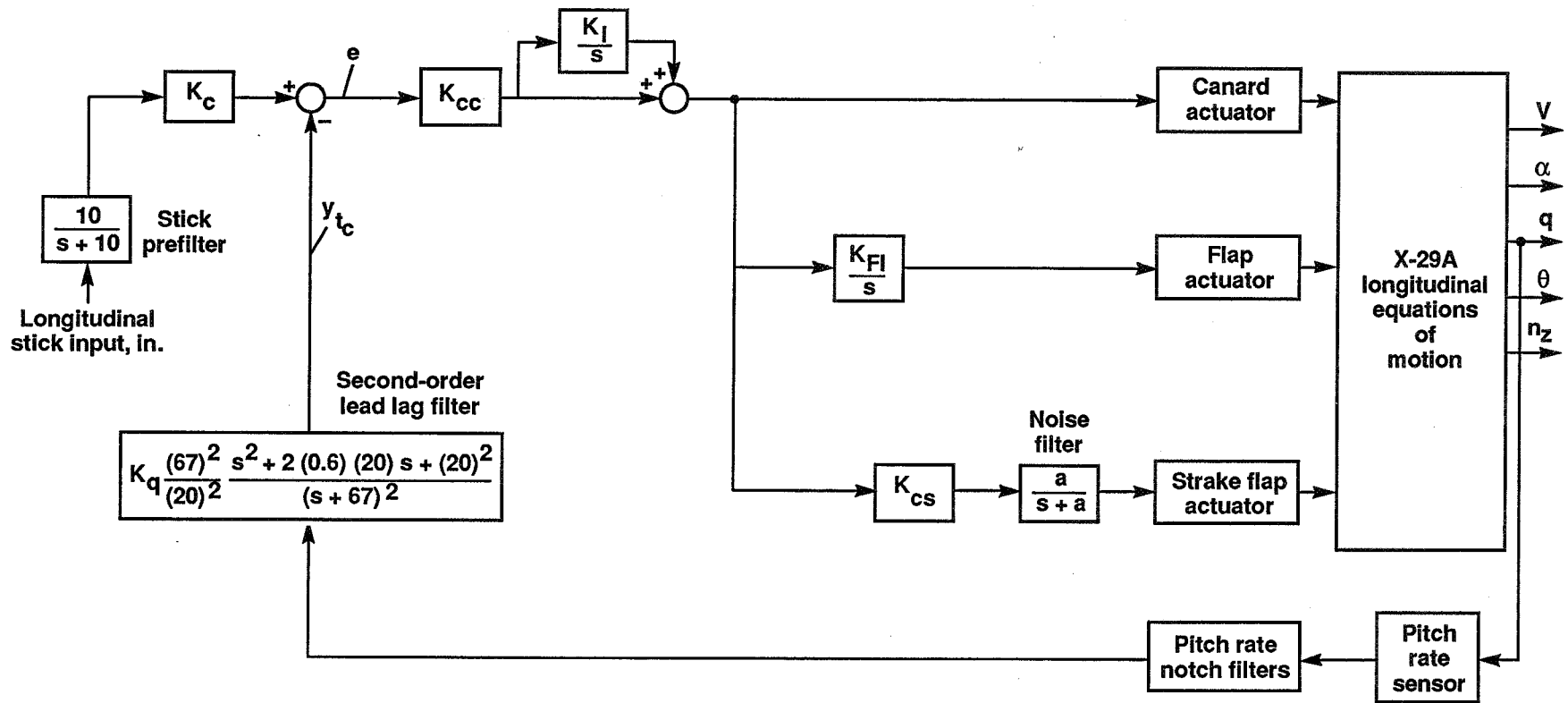
910496

37

Figure 6. Longitudinal AR mode.
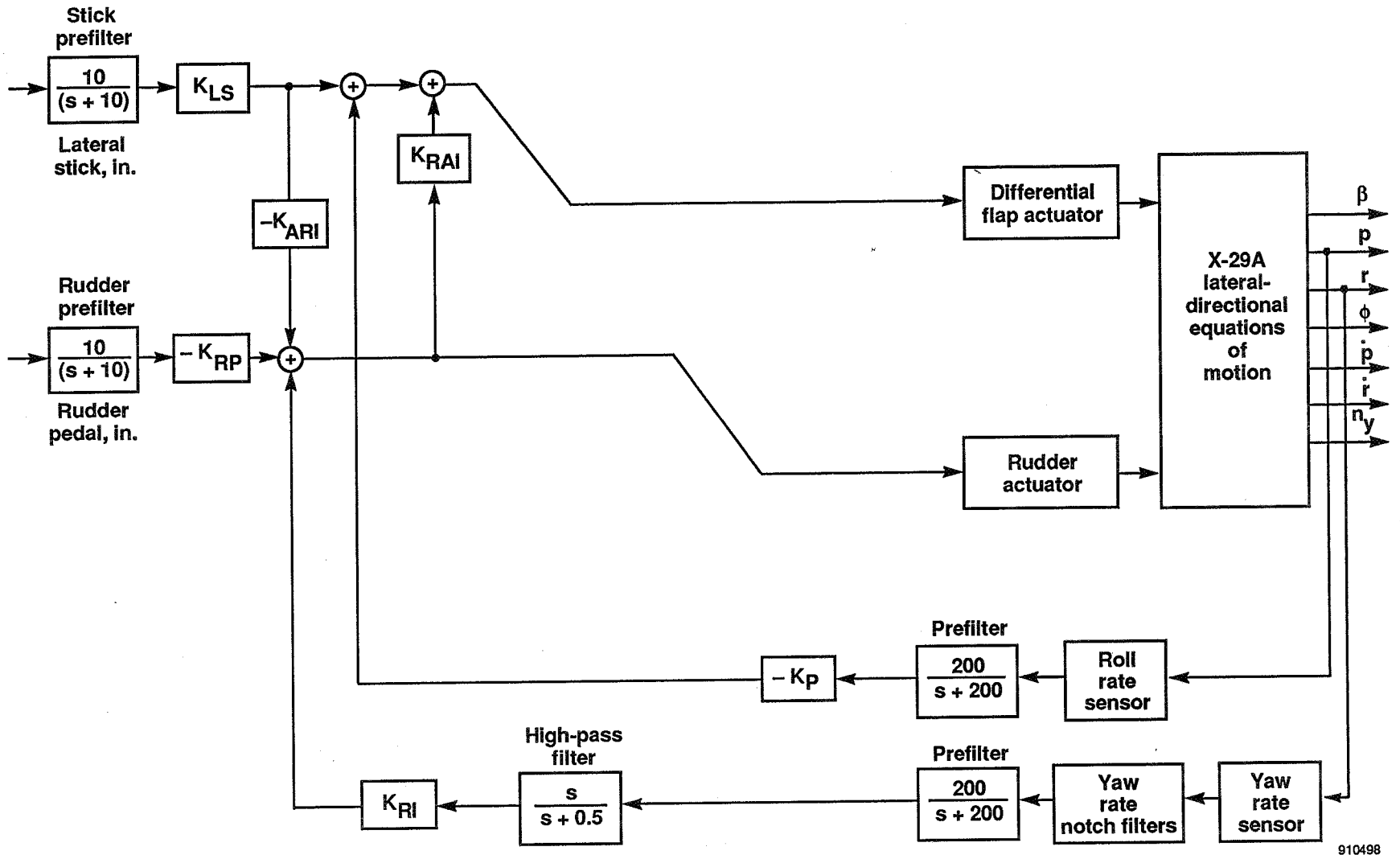
Figure 7. Lateral-directional AR mode.
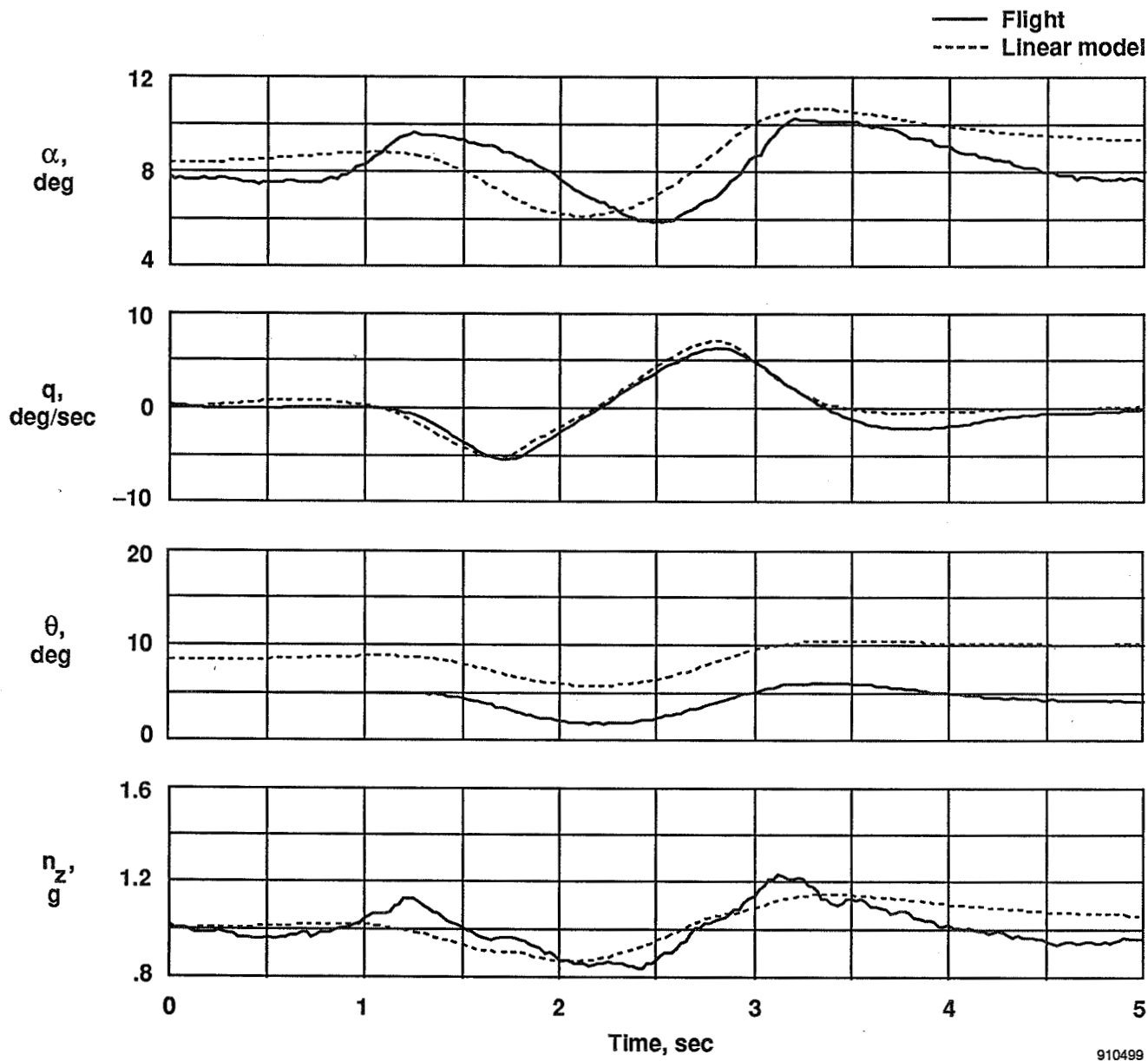
910498

(a)

Figure 8. Response to pitch doublet in the ND–PA mode; $M = 0.258$, $h = 4,000$ ft.
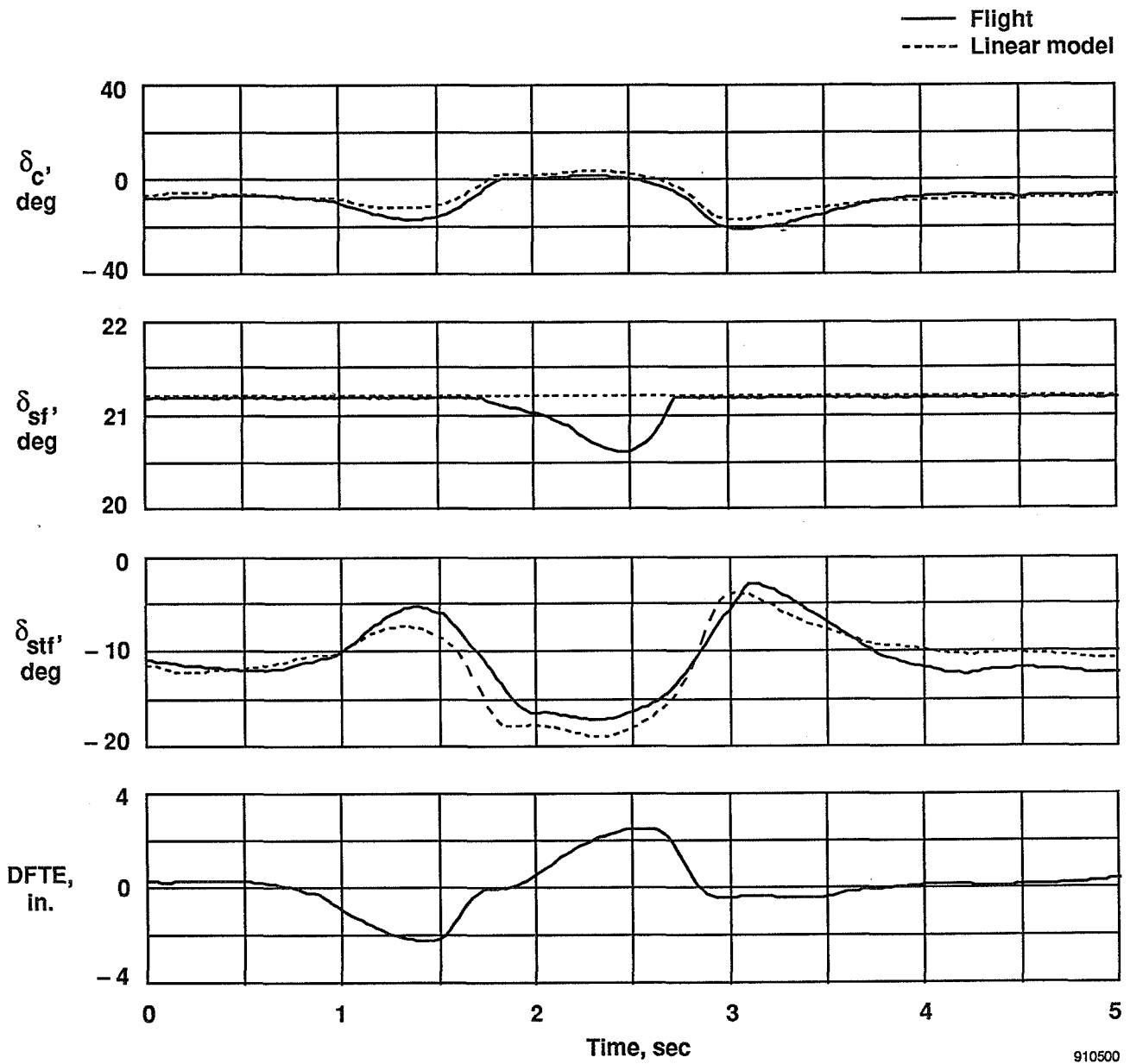
40

(b)

Figure 8. Concluded.
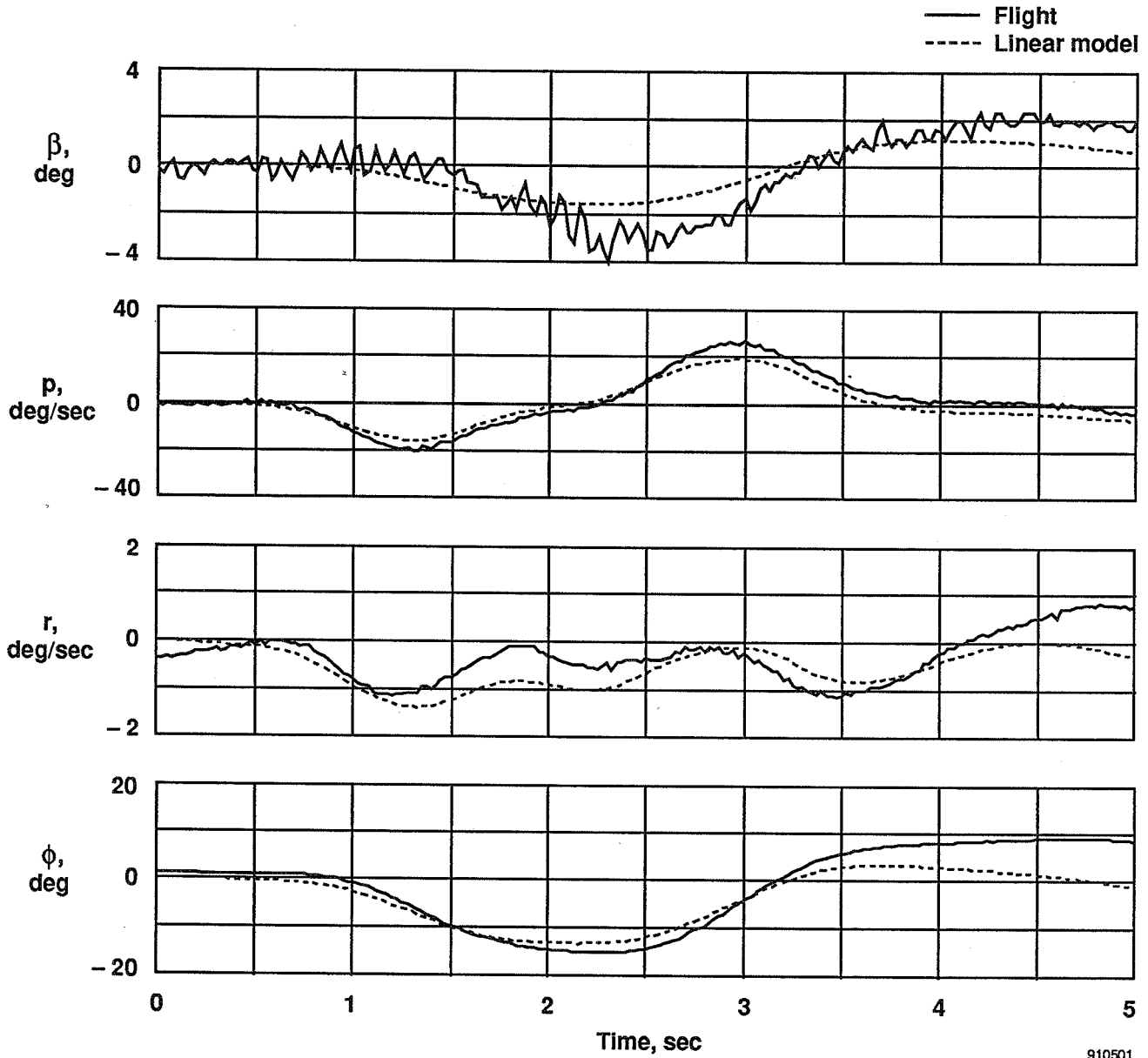
(a)

Figure 9. Response to roll doublet in the ND–PA mode; $M = 0.258$, $h = 4,000$ ft.

42
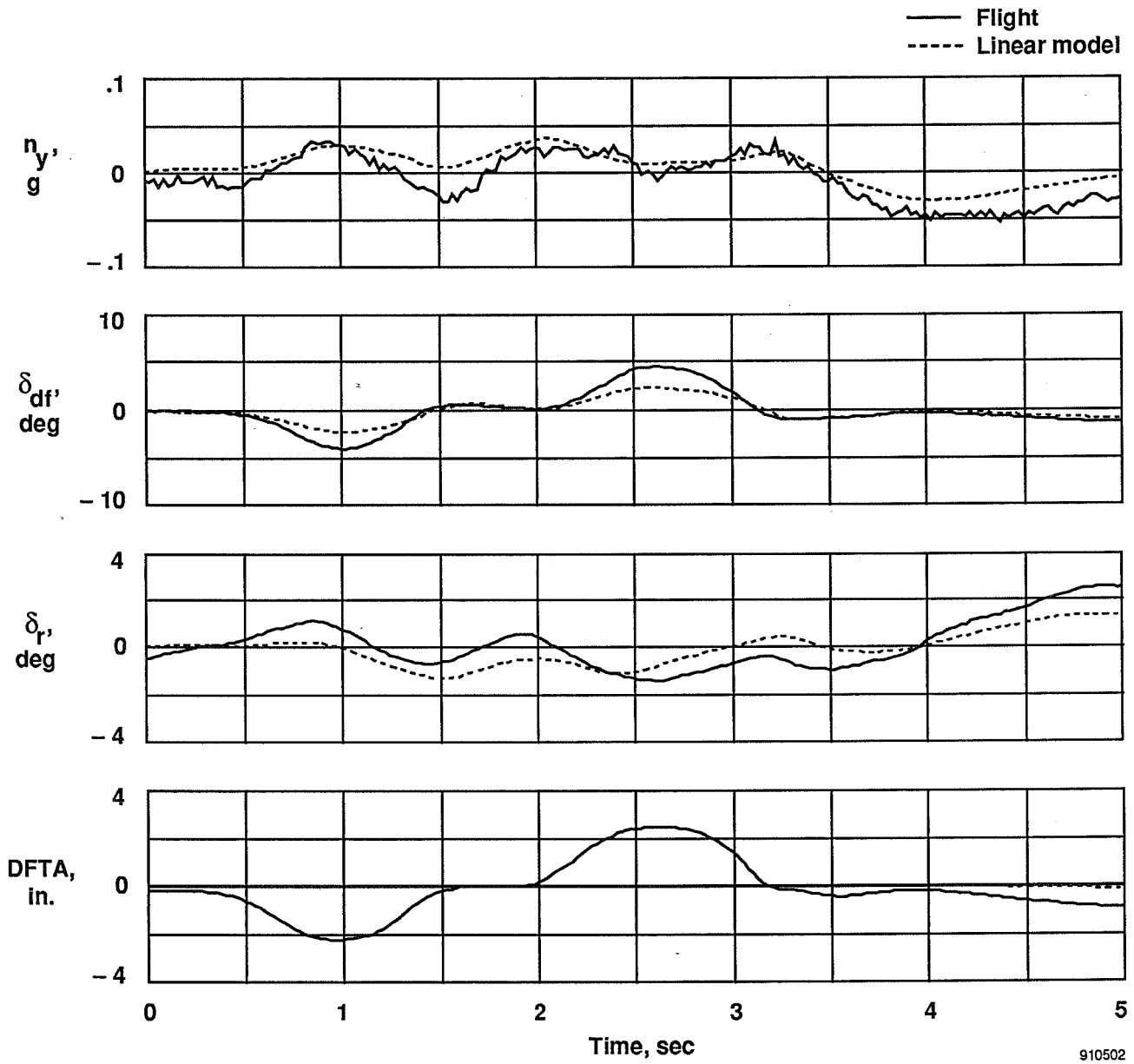
(b)

Figure 9. Continued.
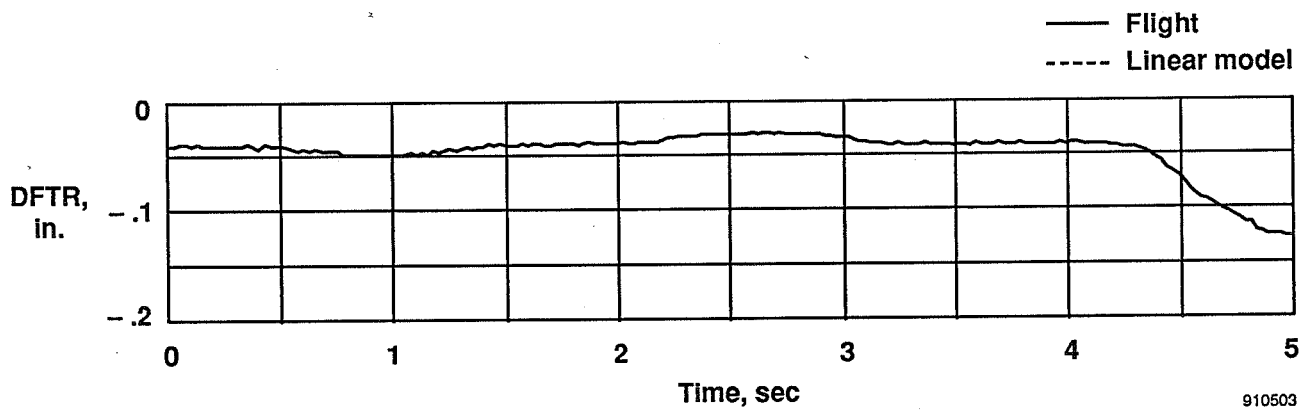
(c)

Figure 9. Concluded.
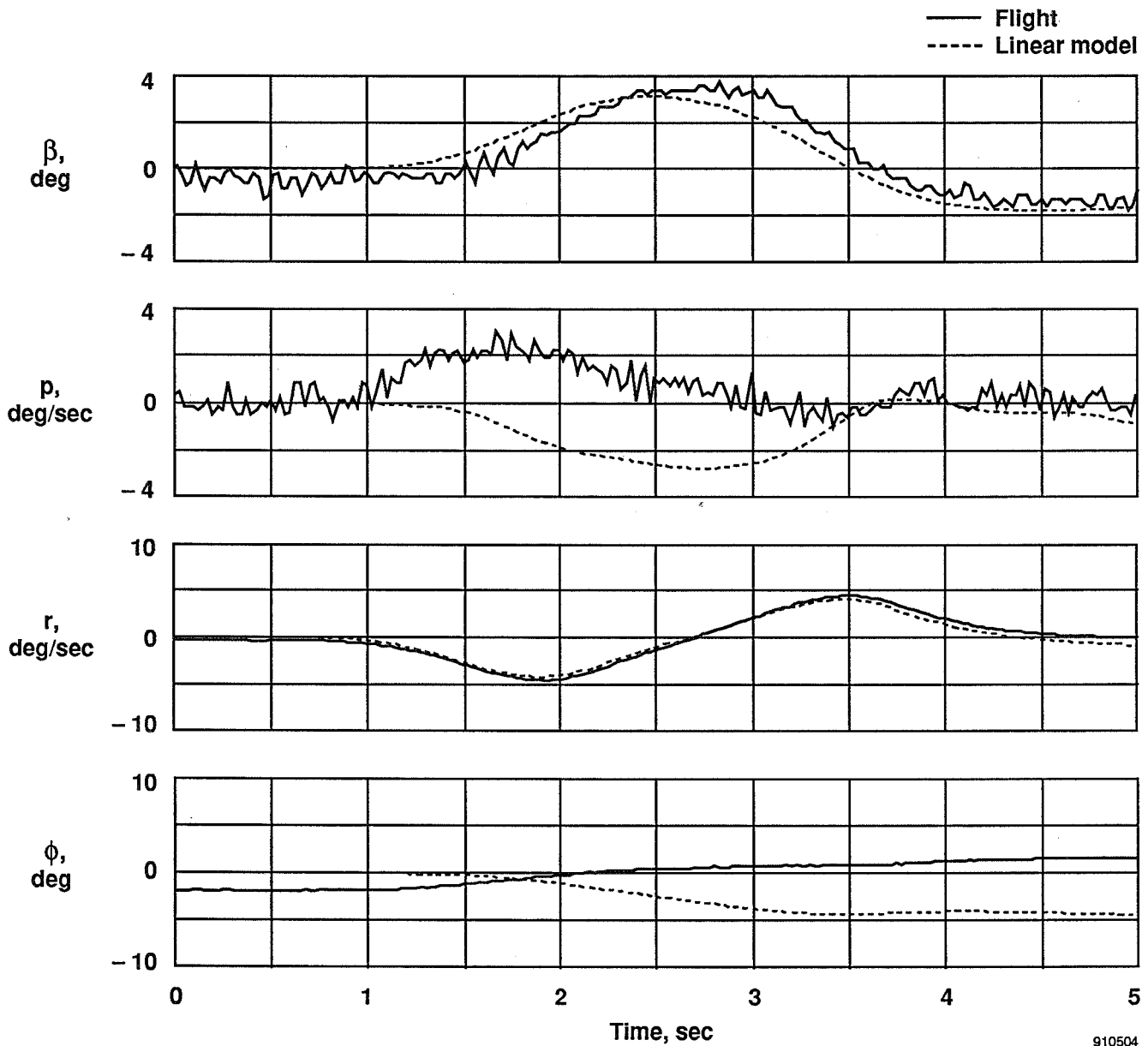
Figure 10. Response to yaw doublet in the ND–PA mode; $M = 0.258$, $h = 4,000$ ft.
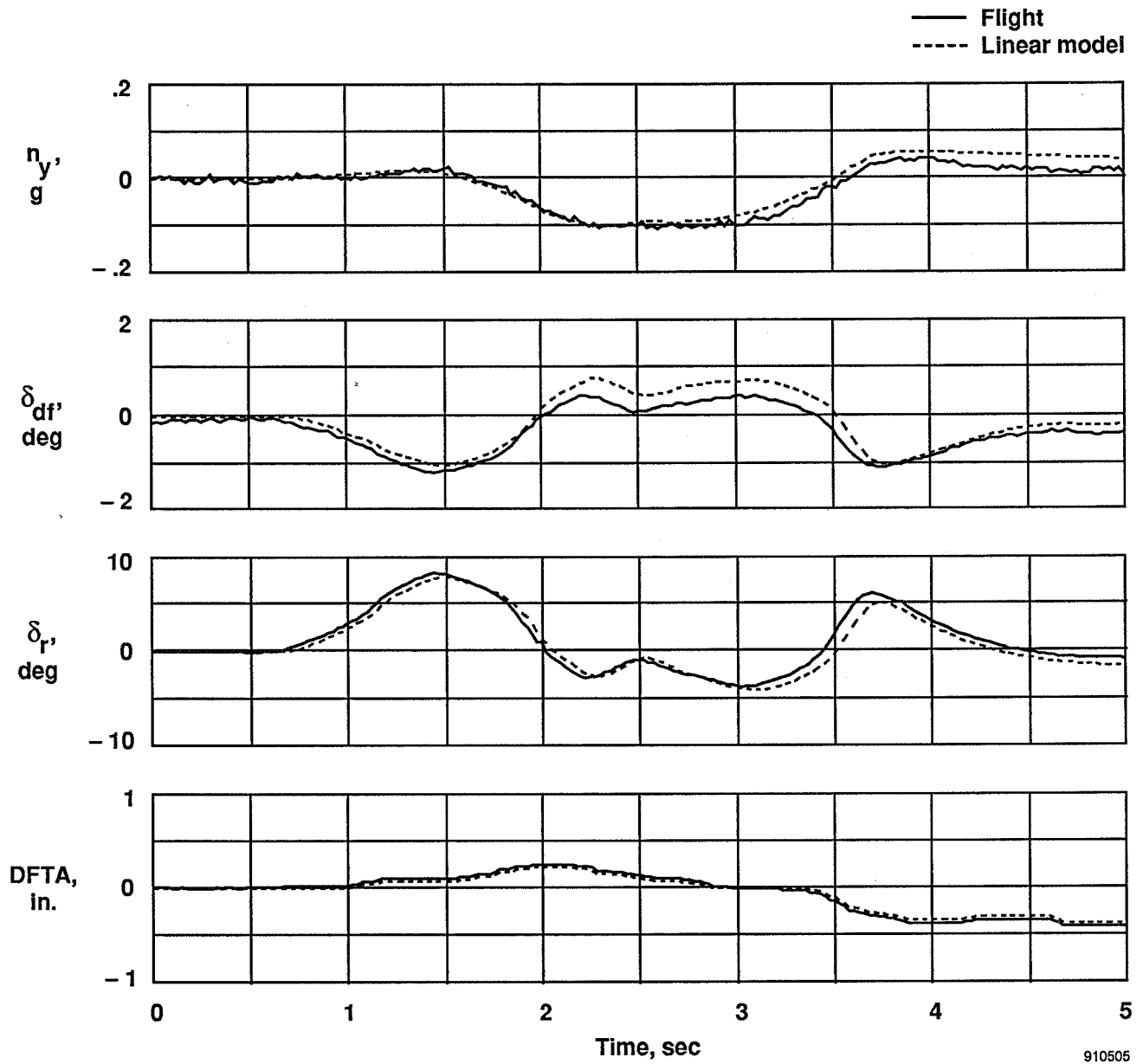
(b)

Figure 10. Continued.
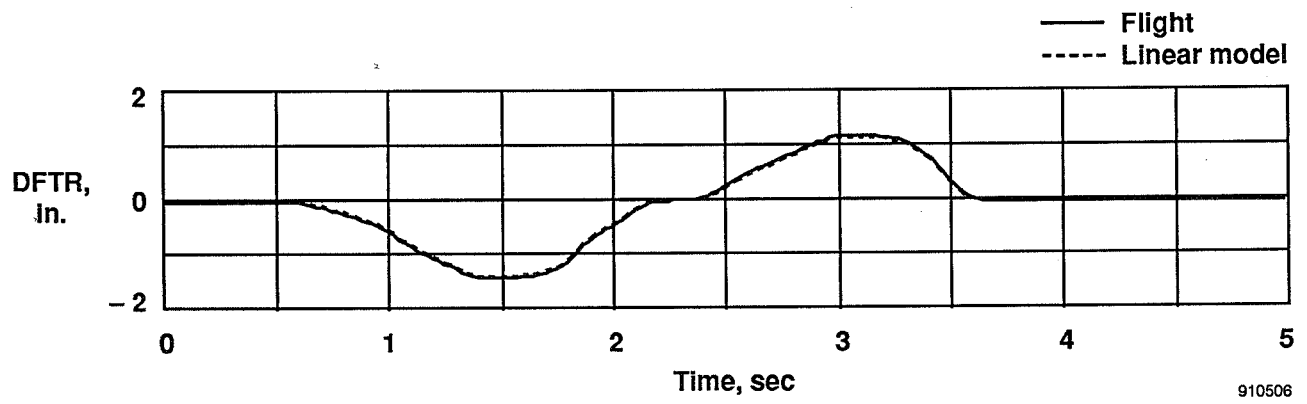
(c)

Figure 10. Concluded.
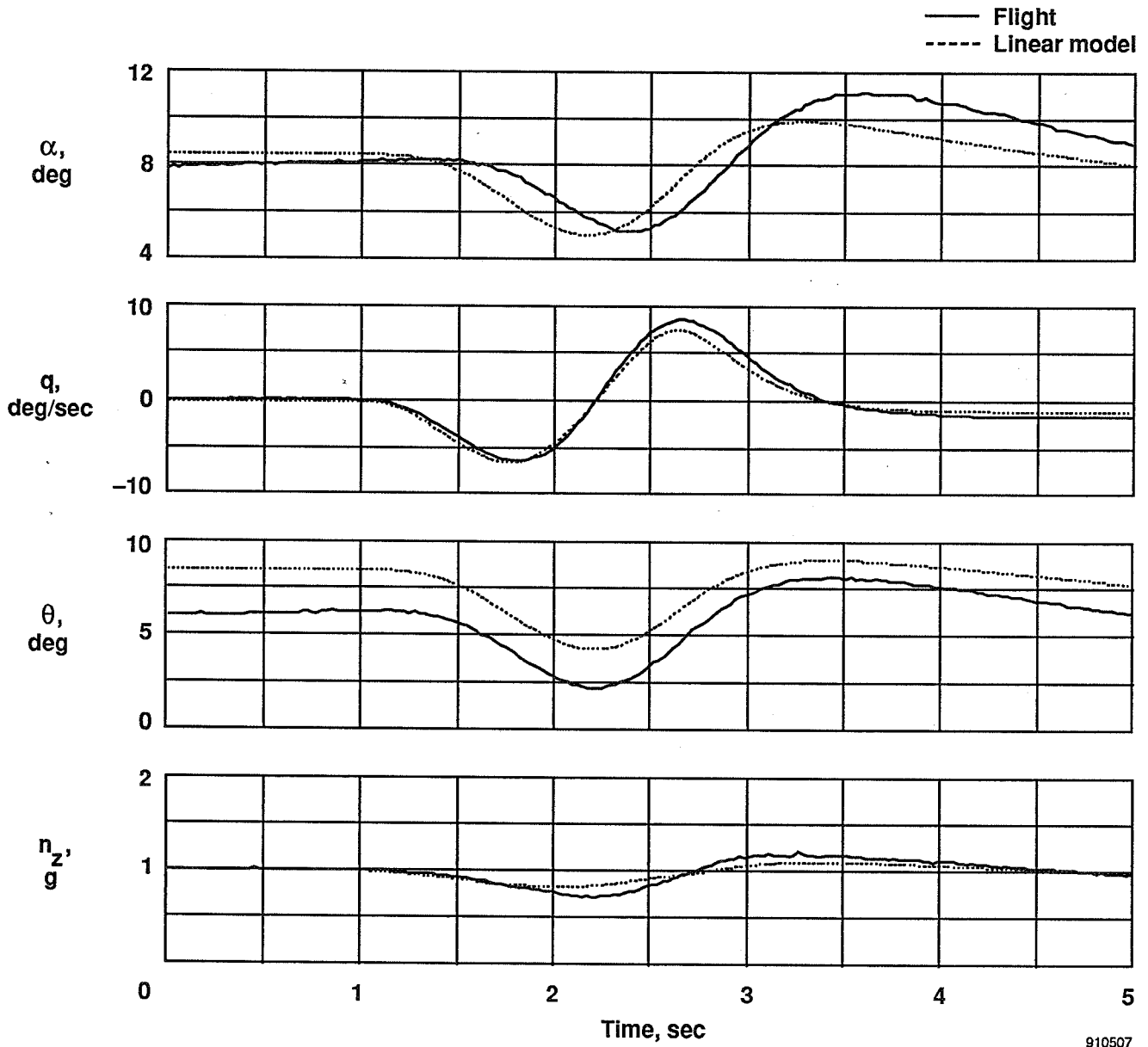
(a)

Figure 11. Response to pitch doublet in the AR–PA mode; $M = 0.258$, $h = 4{,}000$ ft.
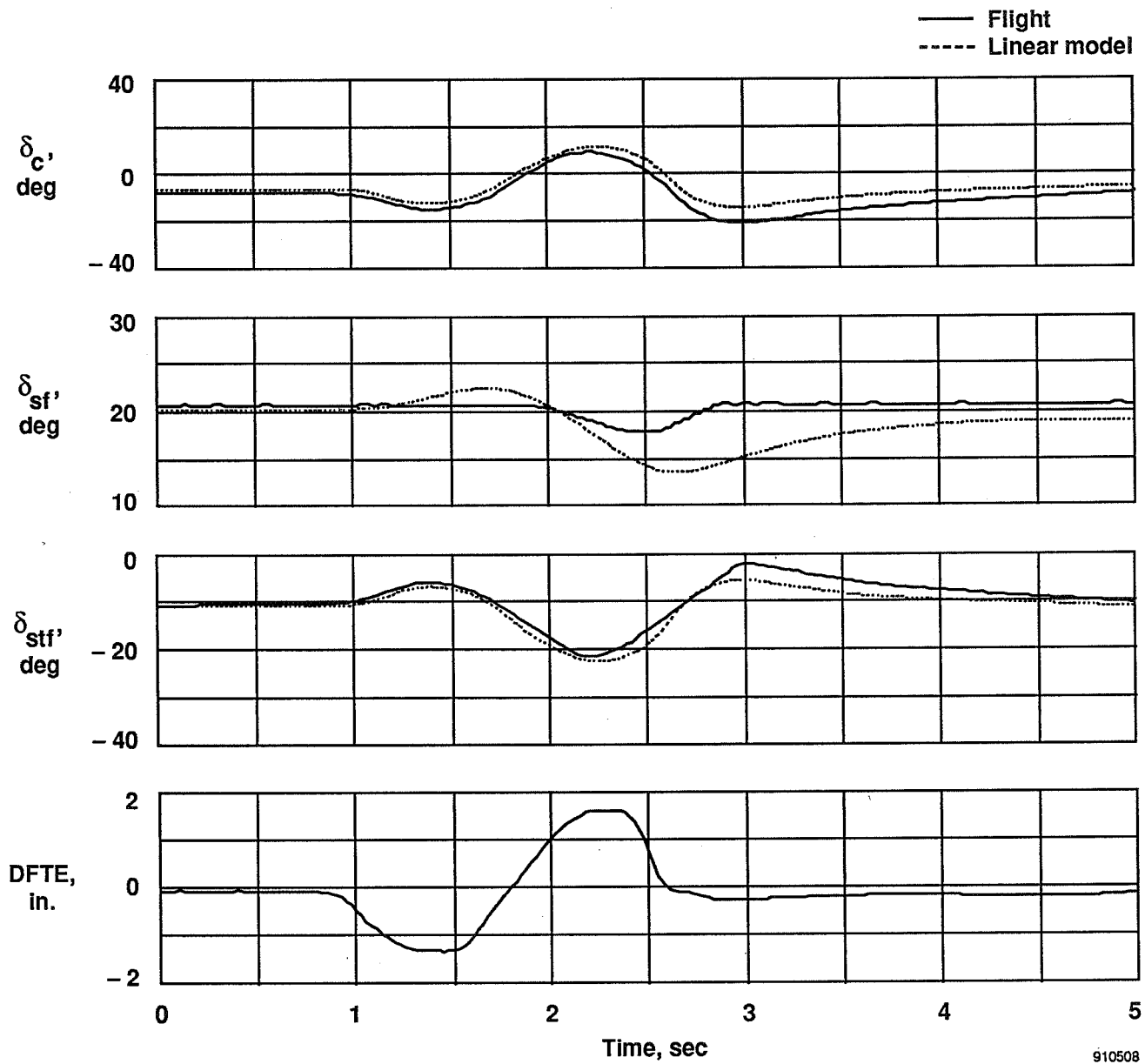
(b)

Figure 11. Concluded.
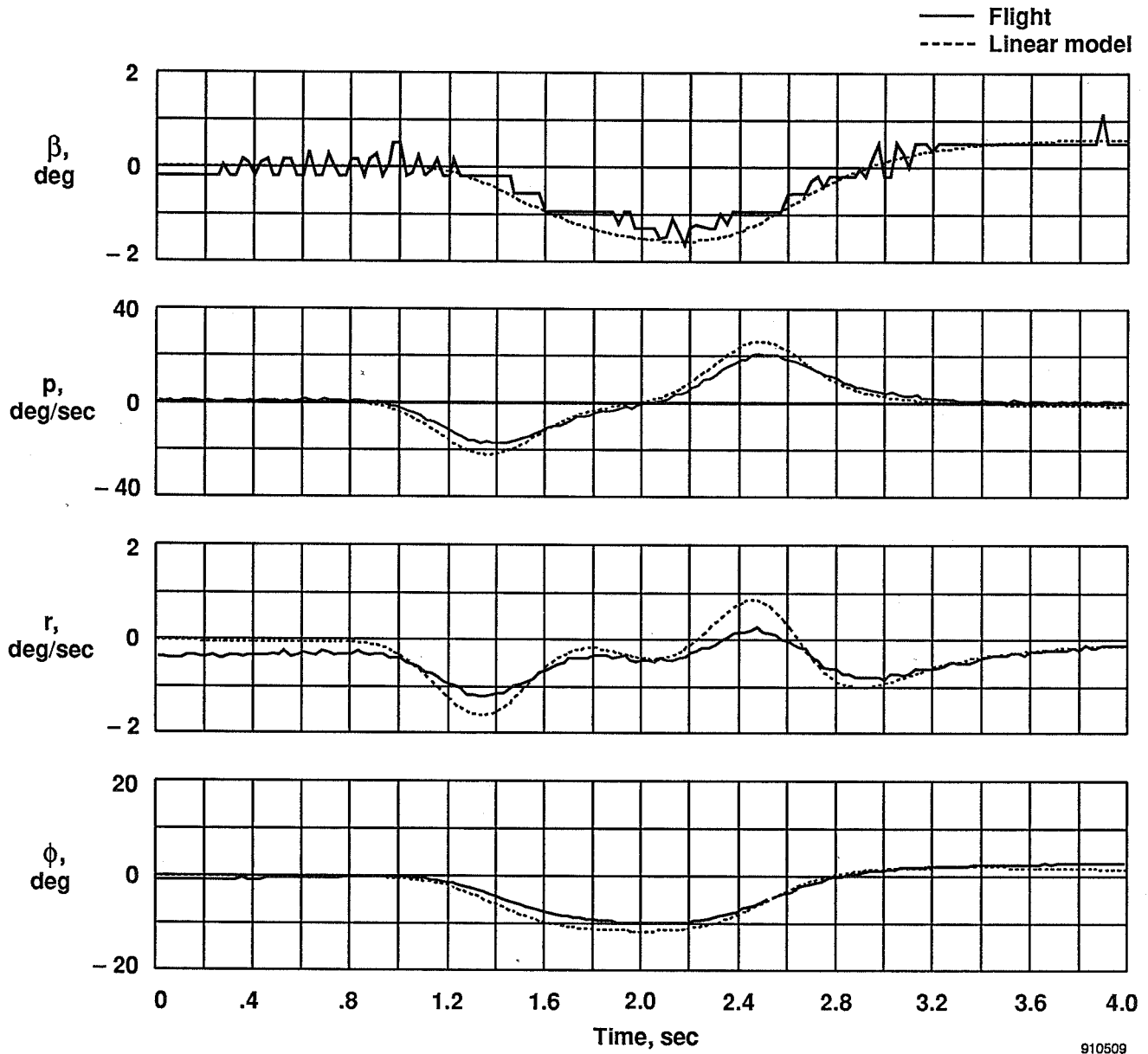
Figure 12. Response to roll doublet in the AR–PA mode; $M = 0.258$, $h = 4,000$ ft.

(a)

910509

50
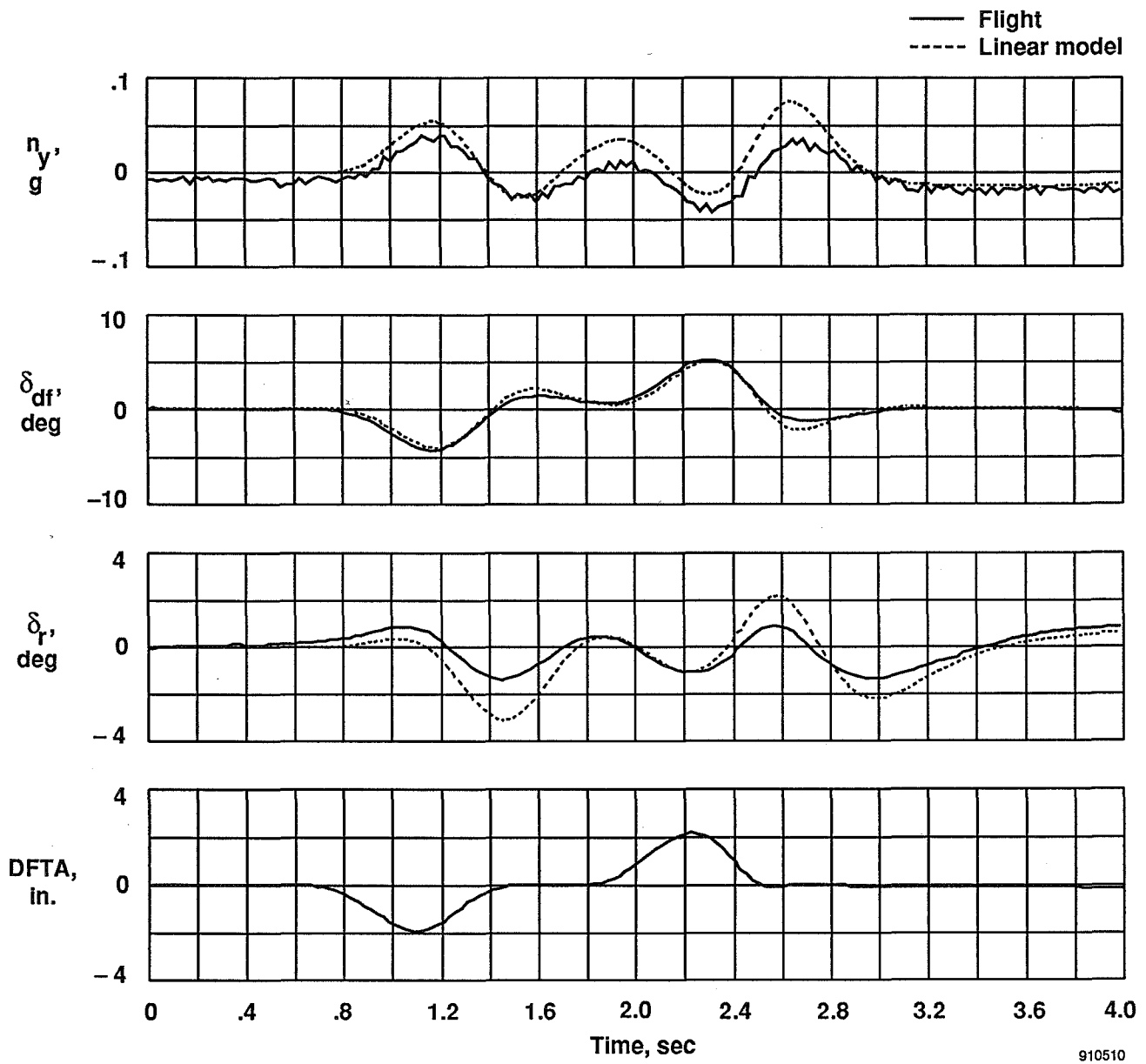
(b)

Figure 12. Continued.
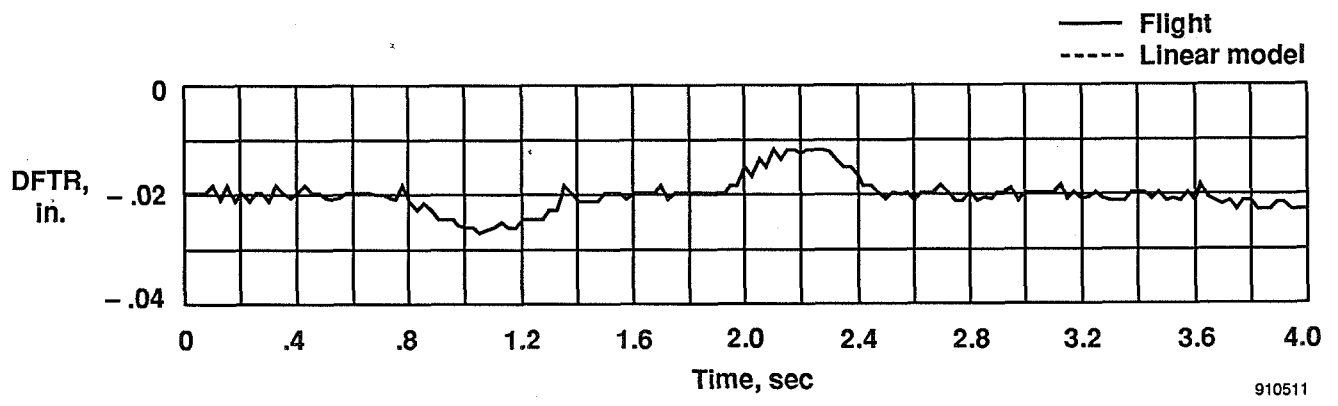
910510

(c)

Figure 12. Concluded.
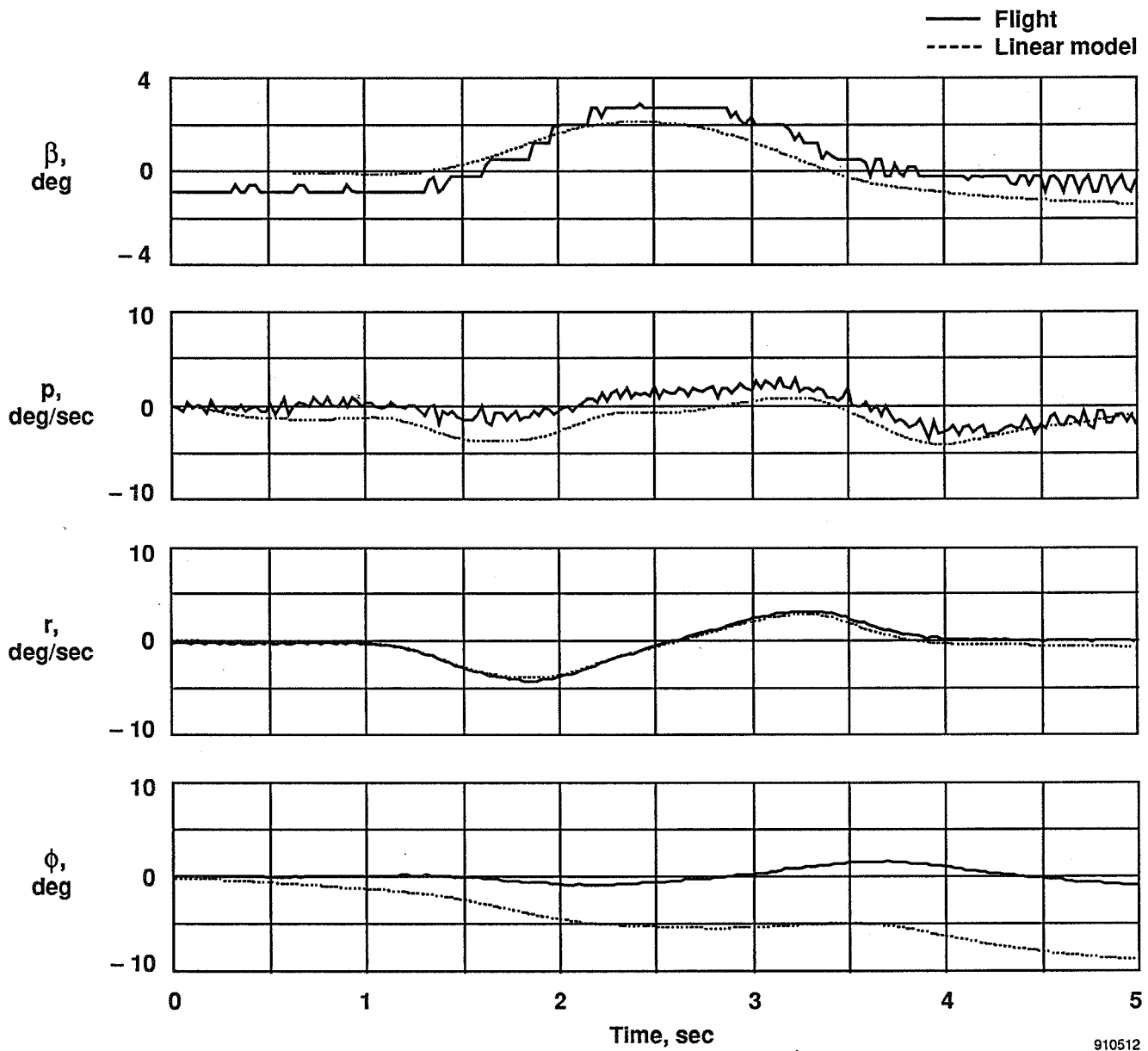
Figure 13. Response to yaw doublet in the AR–PA mode; $M = 0.258$, $h = 4,000$ ft.

(a)
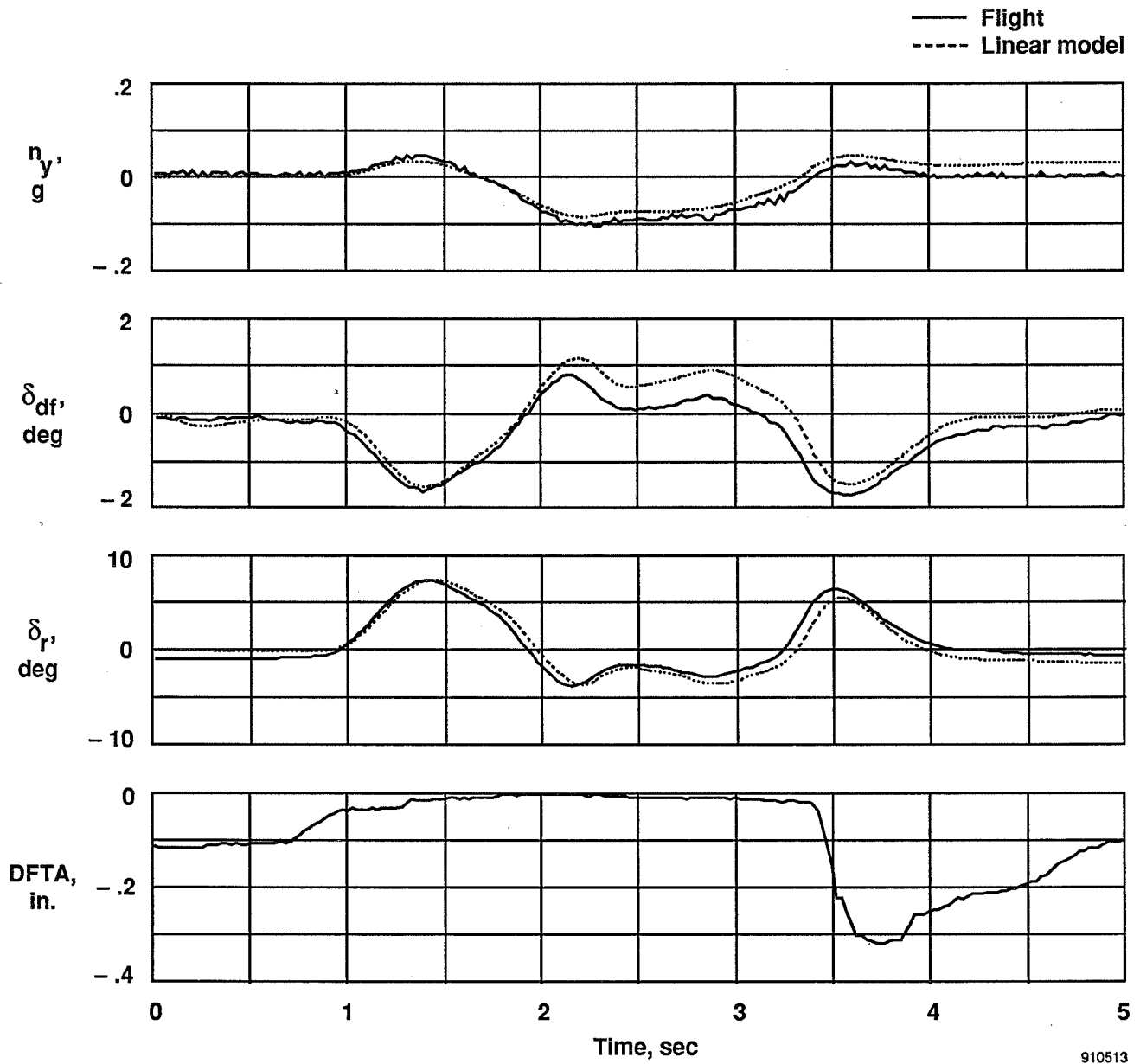
910512

53

(b)

Figure 13. Continued.
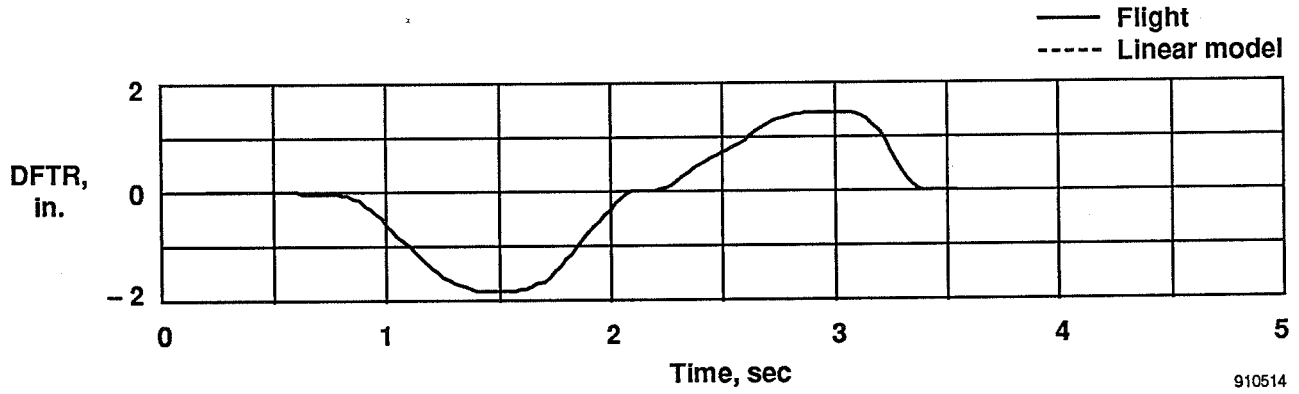
910513

54

(c)

Figure 13. Concluded.
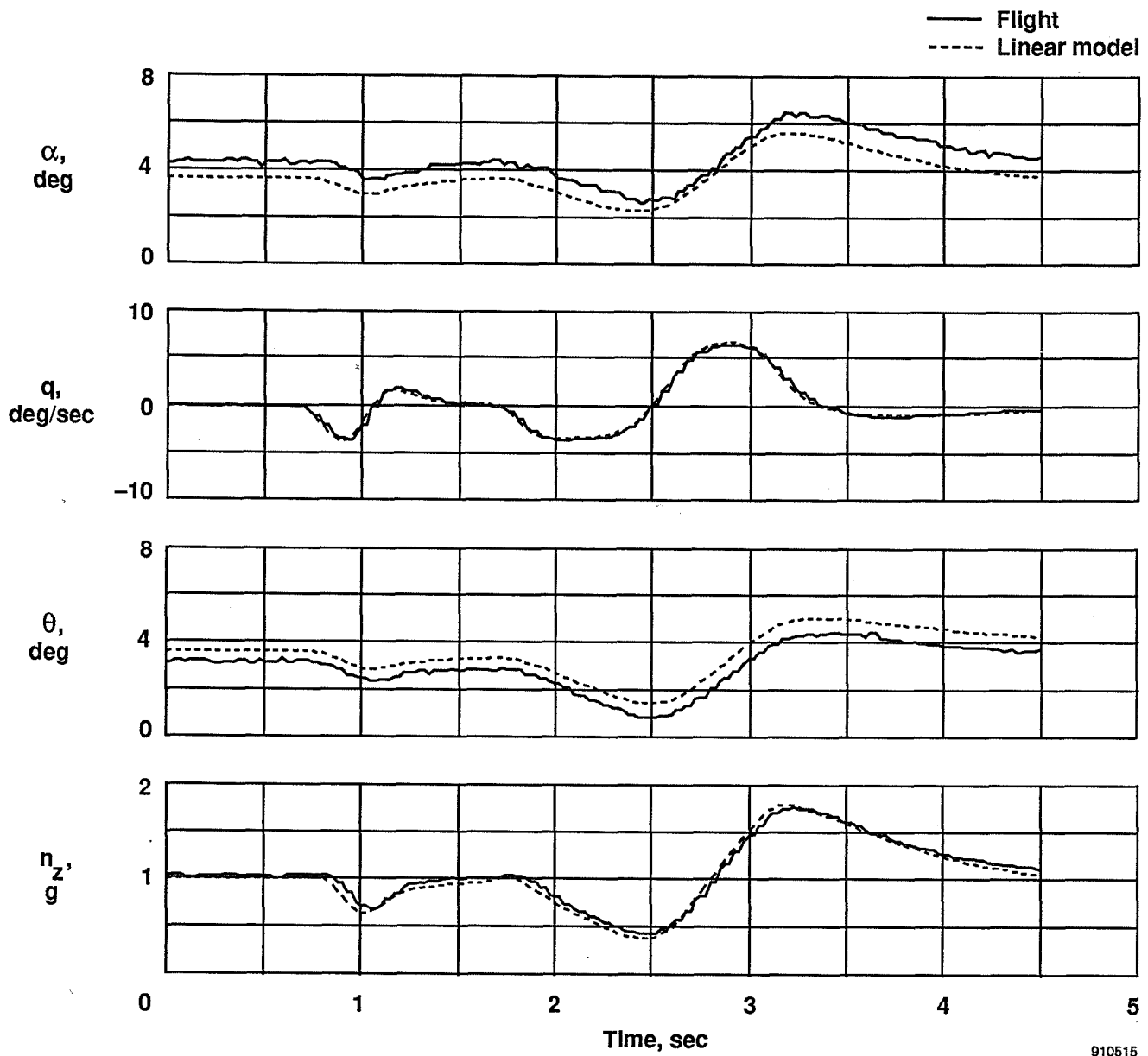
Figure 14. Response to pitch doublet in the ND–UA mode; $M = 0.70$, $h = 20,000$ ft.
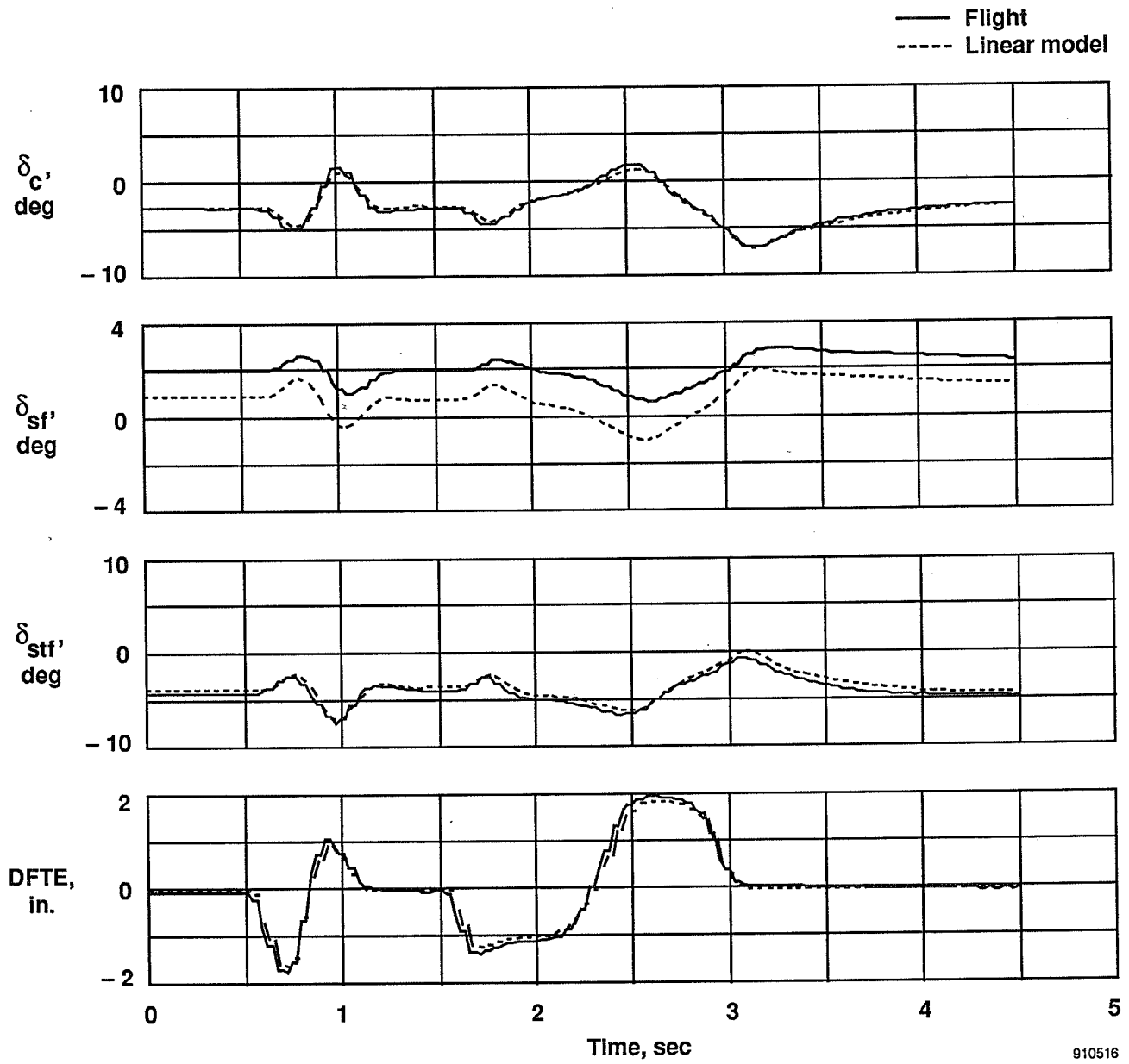
56

(b)

Figure 14. Concluded.
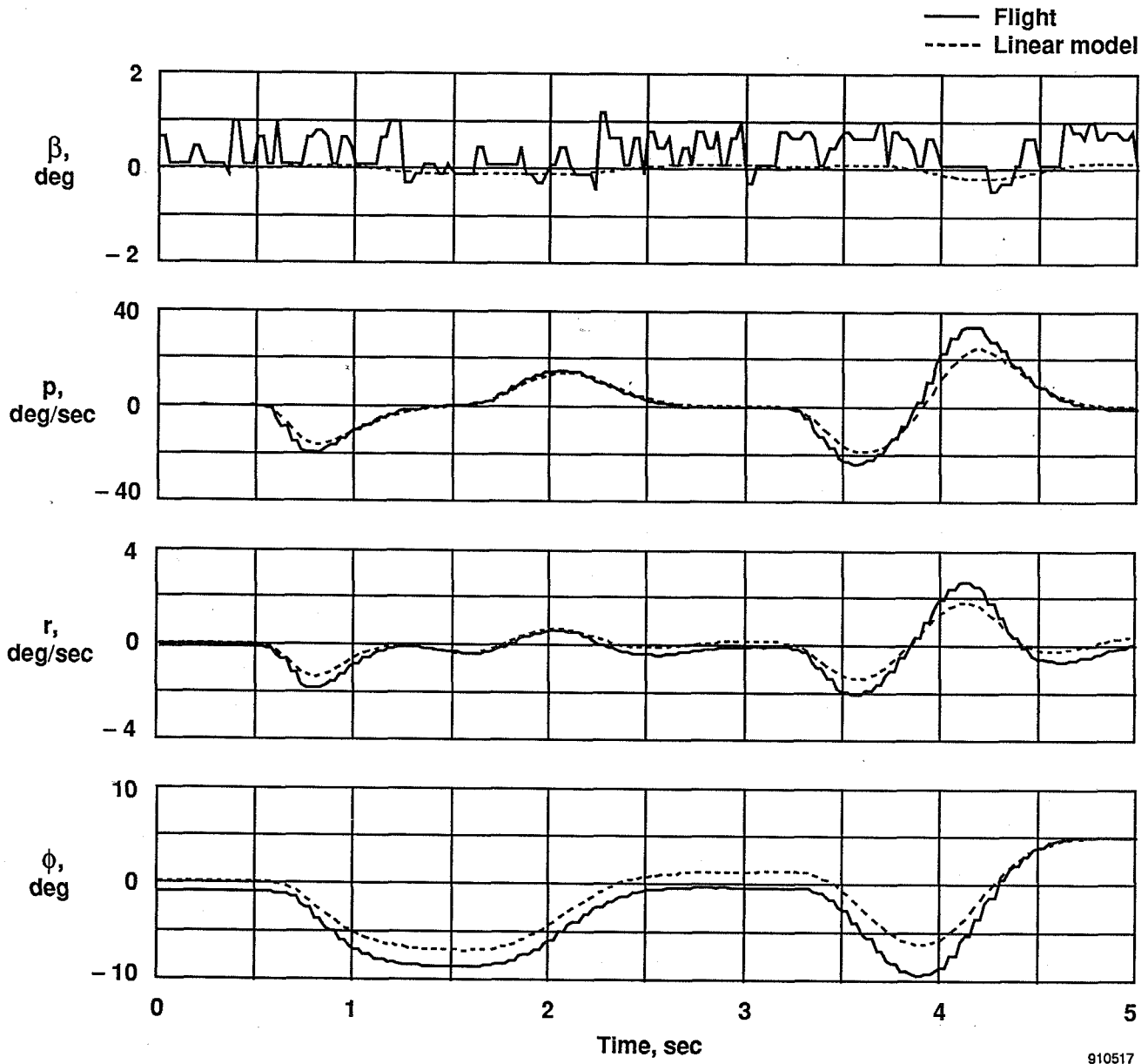
(a)

Figure 15. Response to roll doublet in the ND–UA mode; $M = 0.70$, $h = 20,000$ ft.
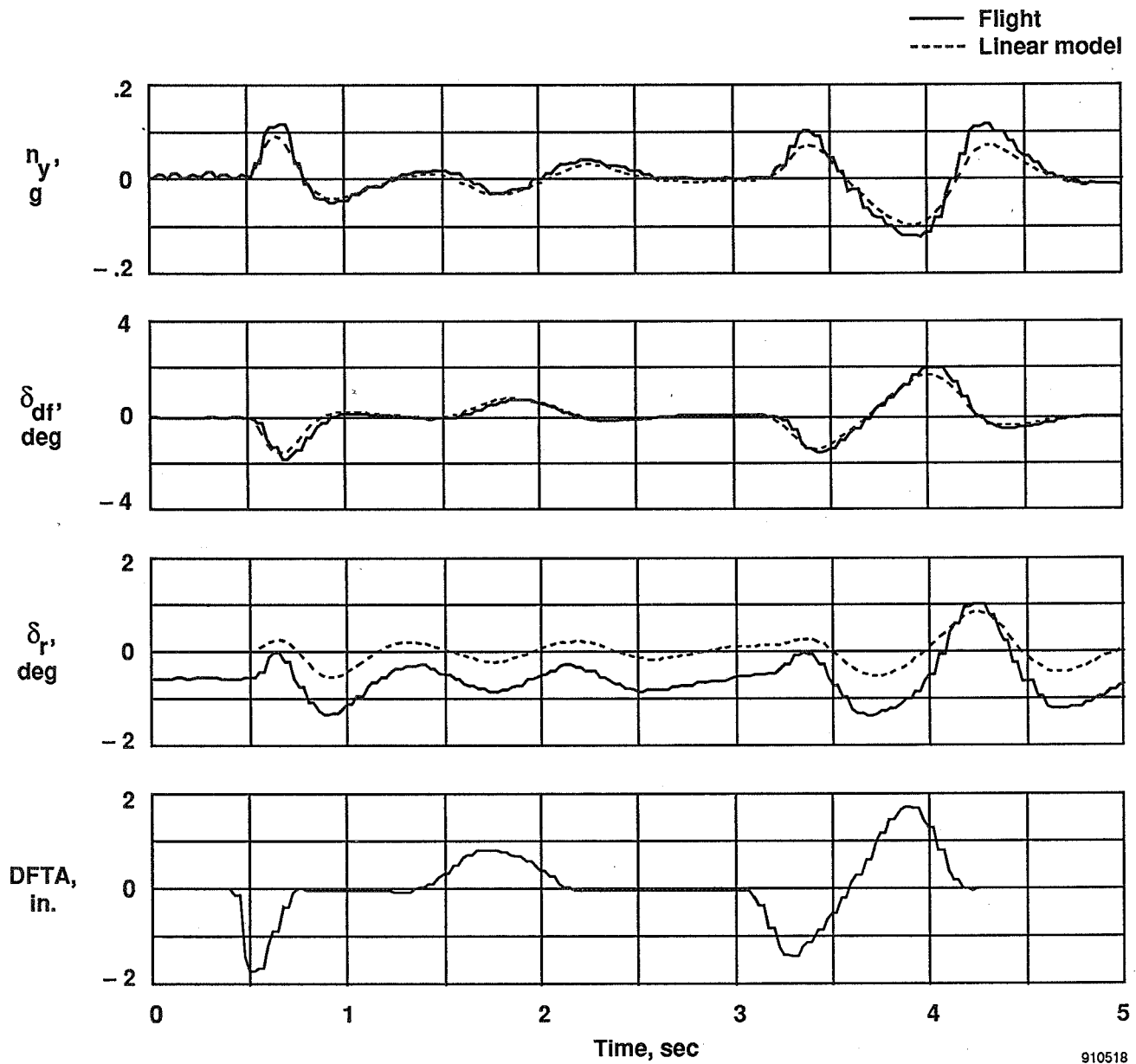
(b)

Figure 15. Continued.

59
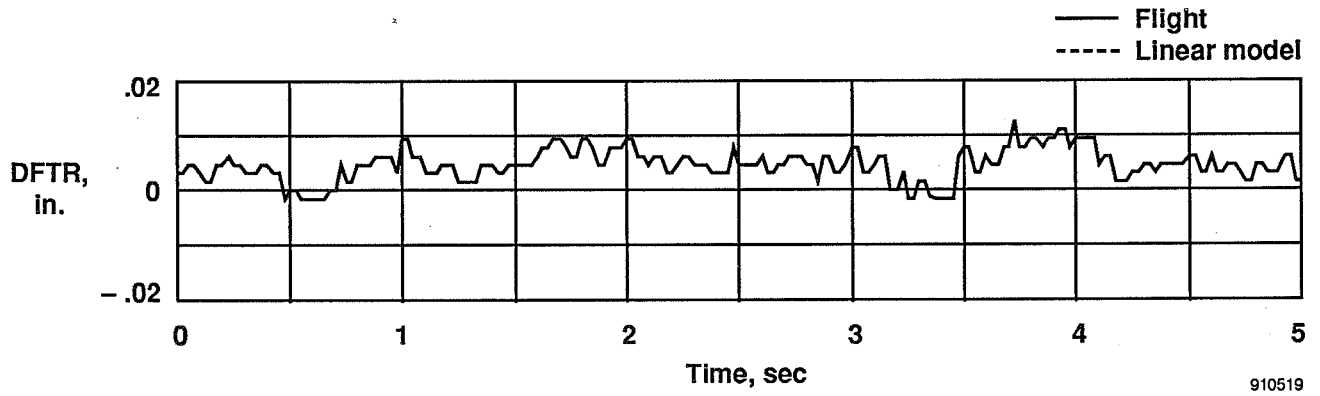
(c)

Figure 15. Concluded.
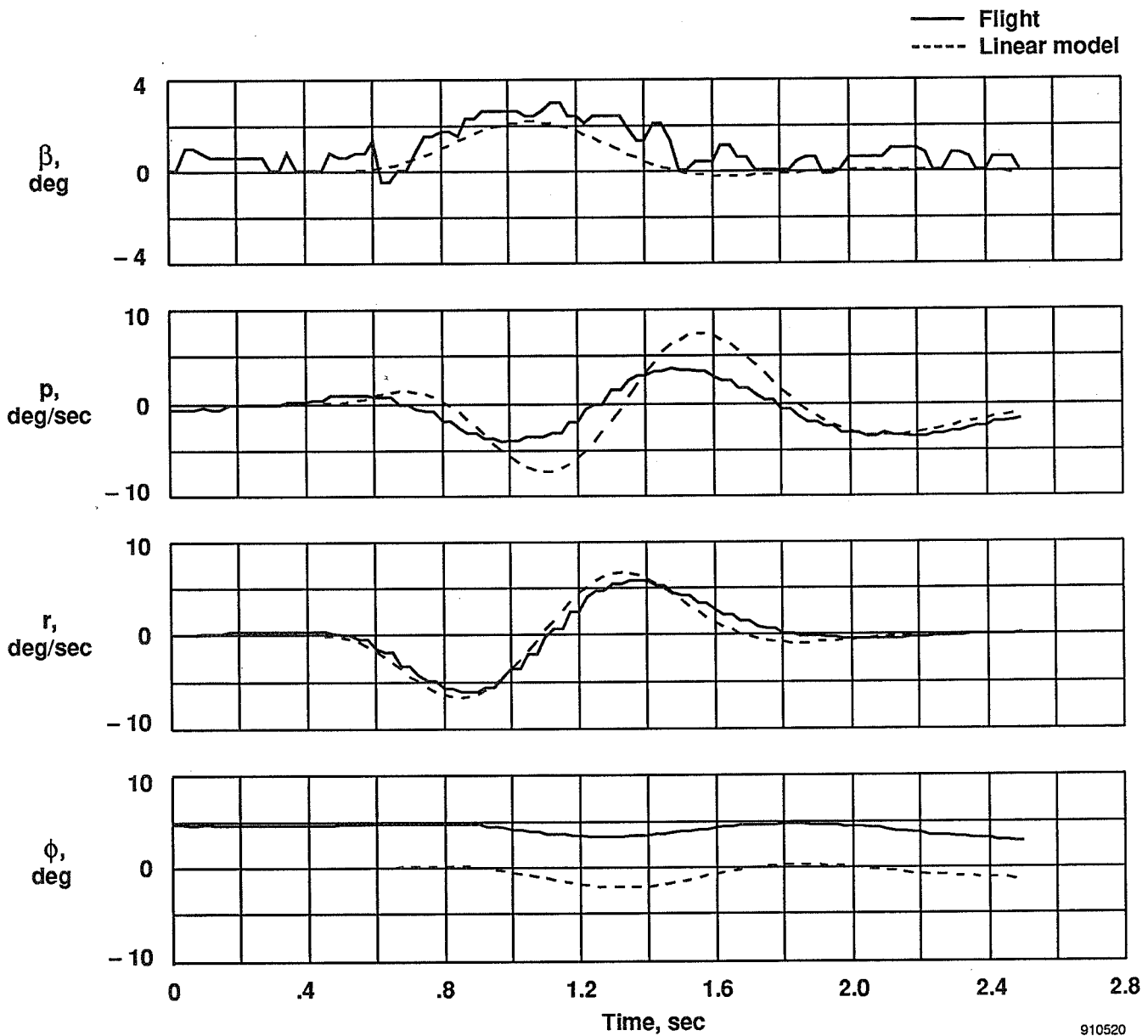
(a)

Figure 16. Response to yaw doublet in the ND–UA mode; $M = 0.70$, $h = 20,000$ ft.
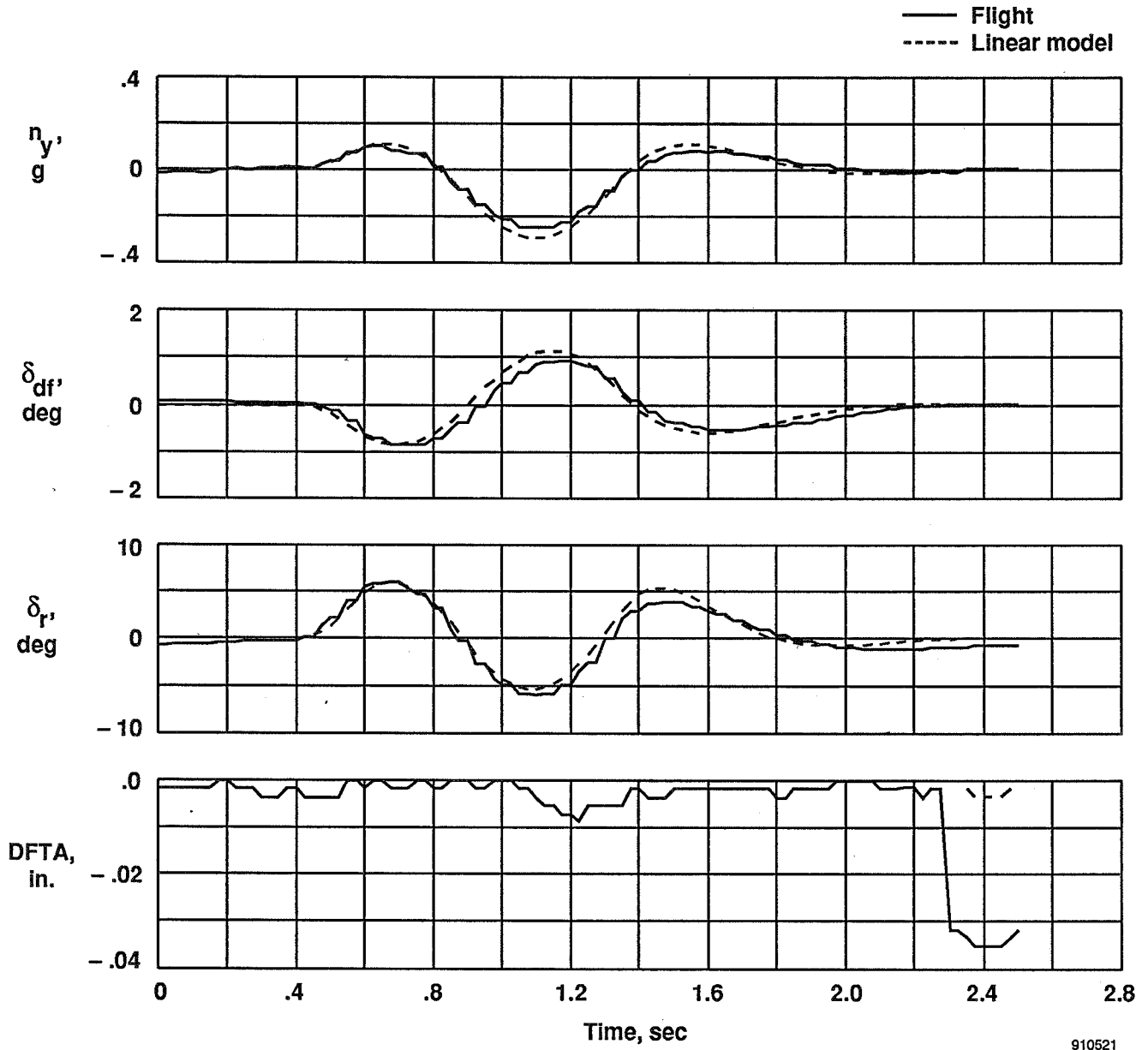
(b)

Figure 16. Continued.
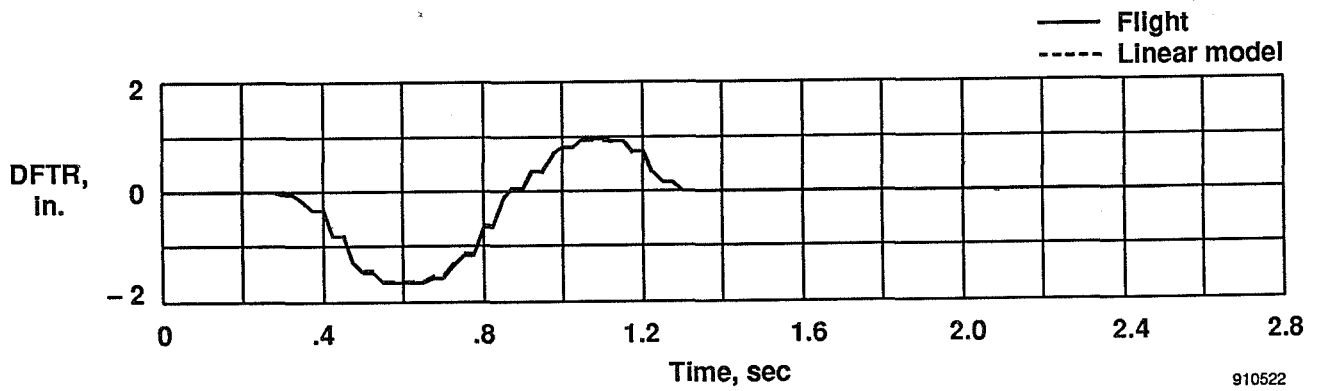
(c)

Figure 16. Concluded.
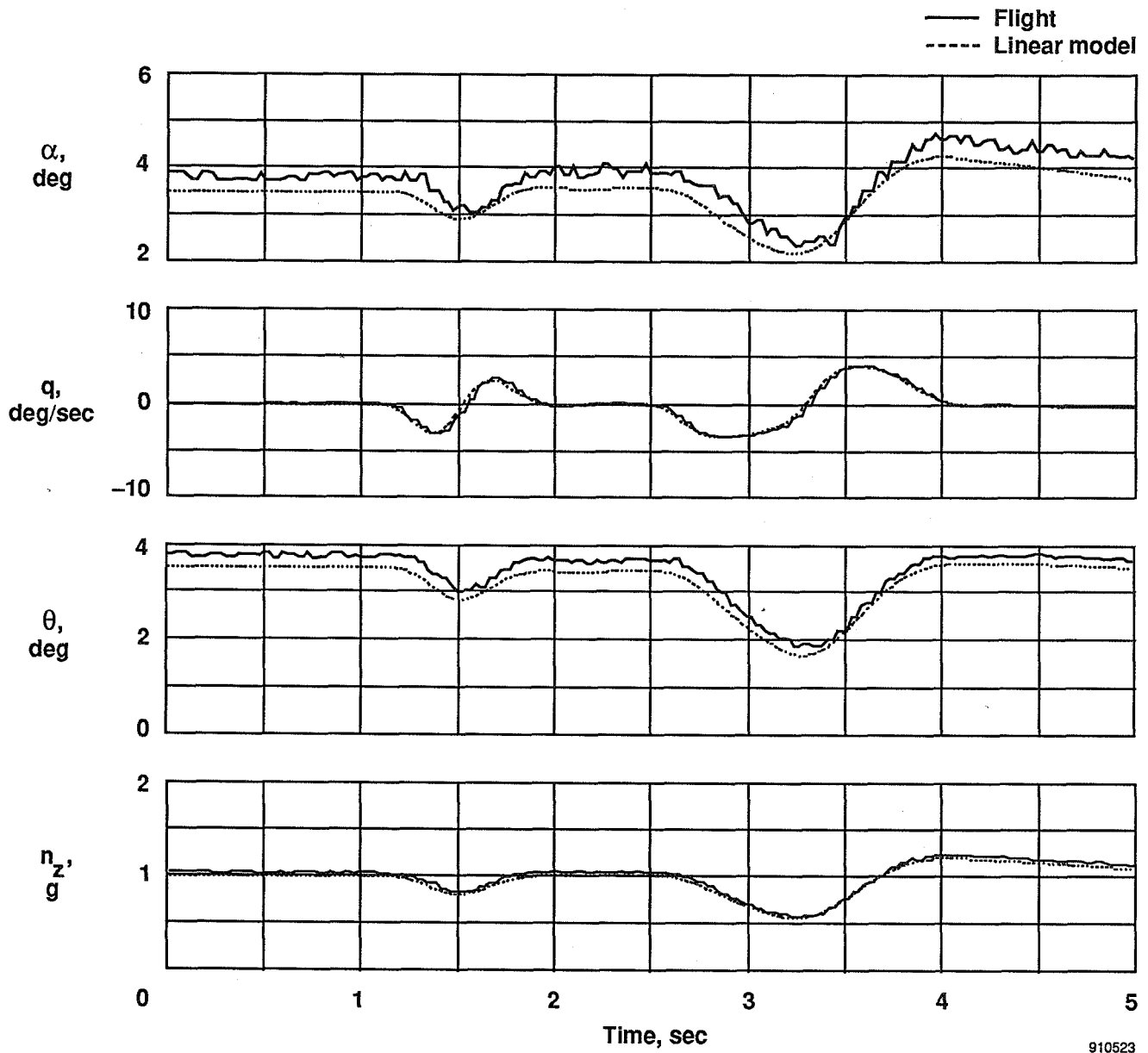
(a)

Figure 17. Response to pitch doublet in the AR–UA mode; $M = 0.70$, $h = 20,000$ ft.

64
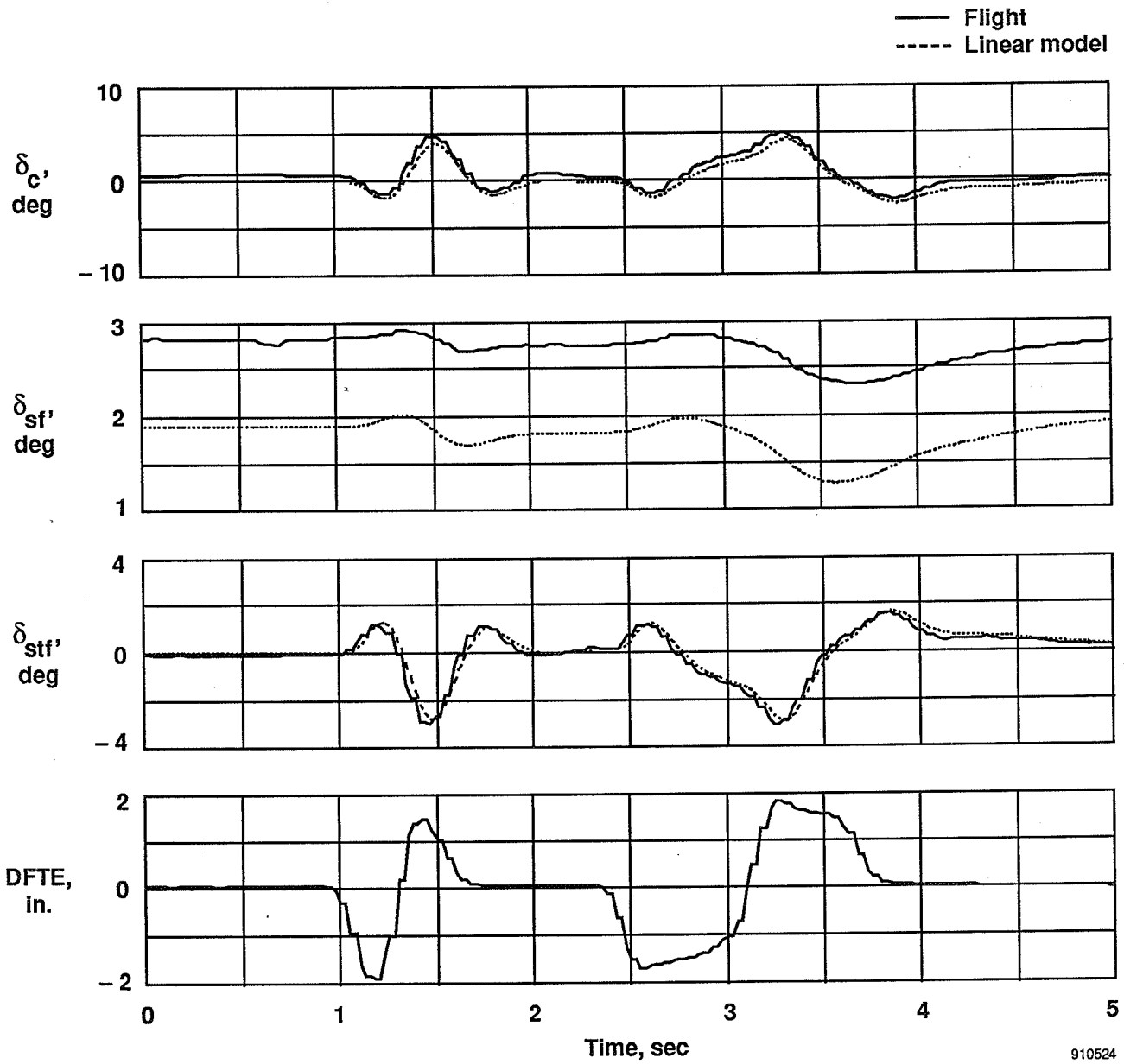
(b)

Figure 17. Concluded.
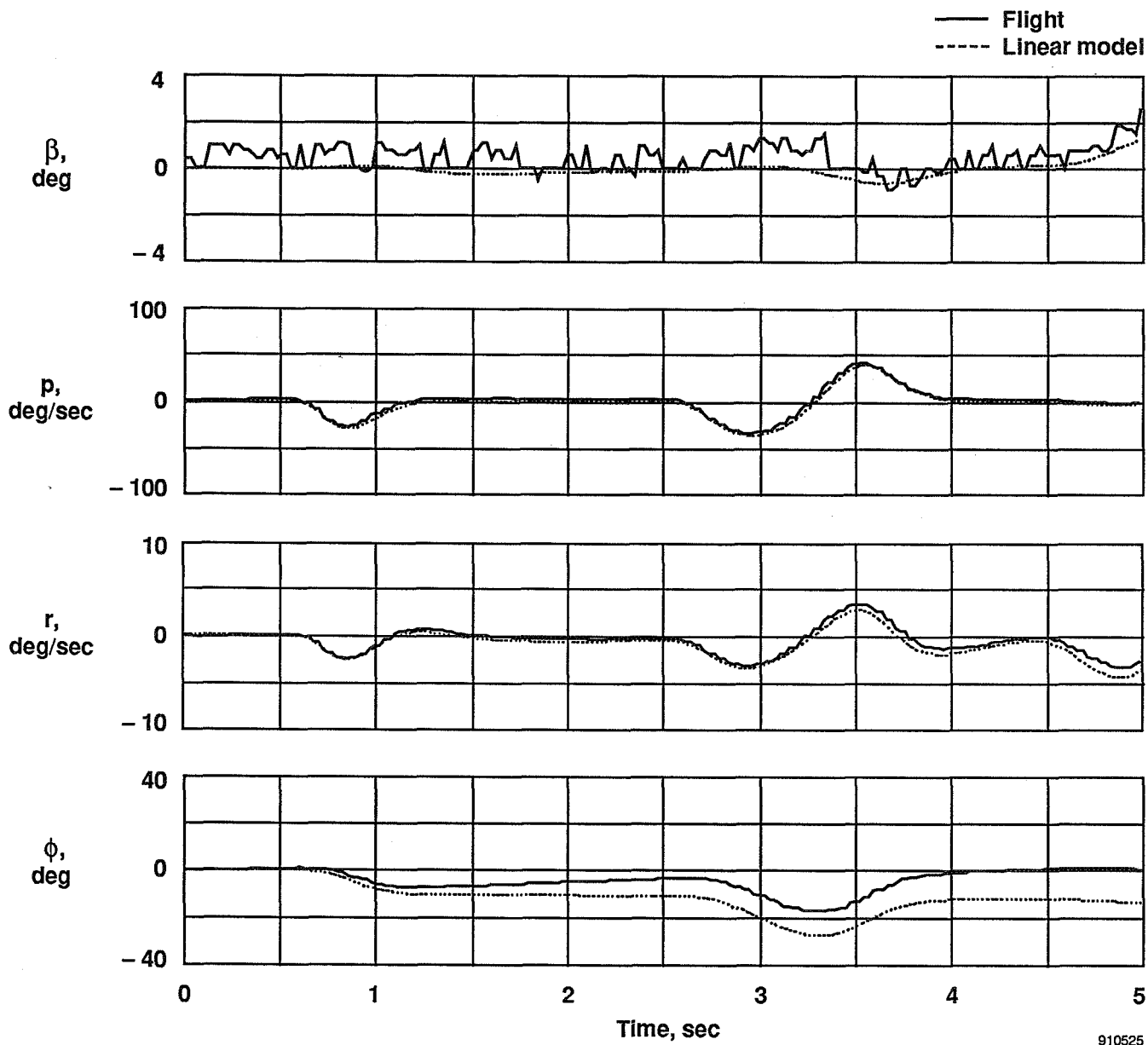
(a)

Figure 18. Response to roll doublet in the AR–UA mode; $M = 0.70$, $h = 20,000$ ft.
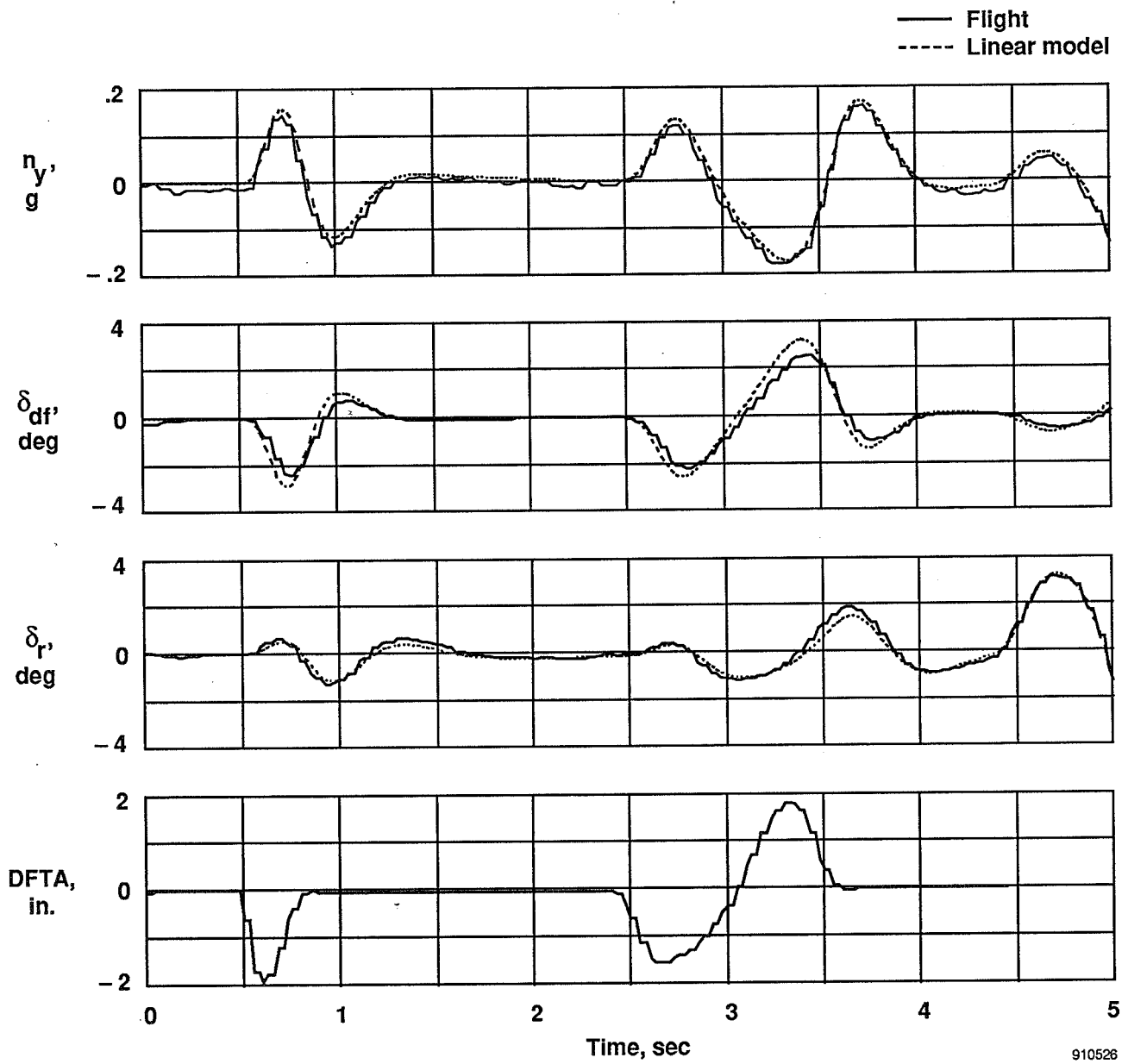
(b)

Figure 18. Continued.
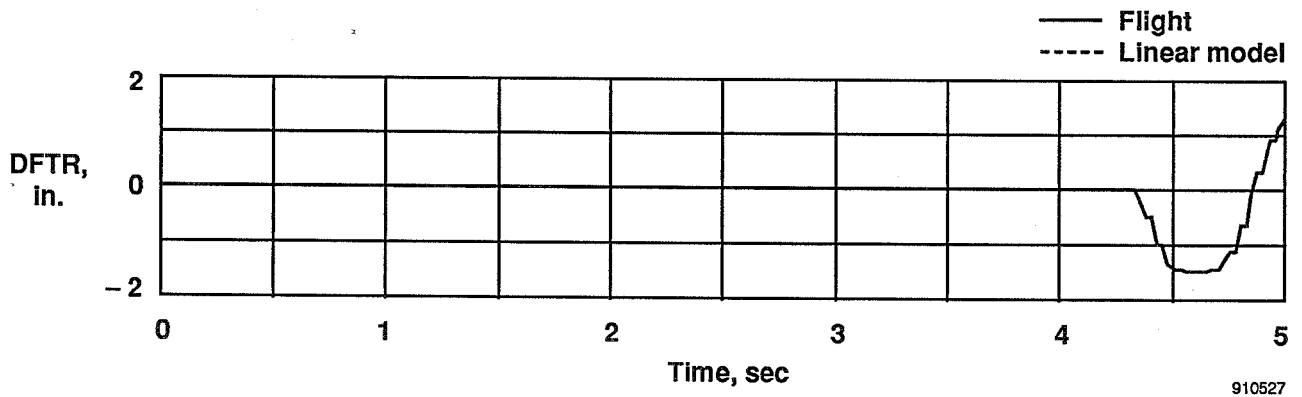
(c)

Figure 18. Concluded.
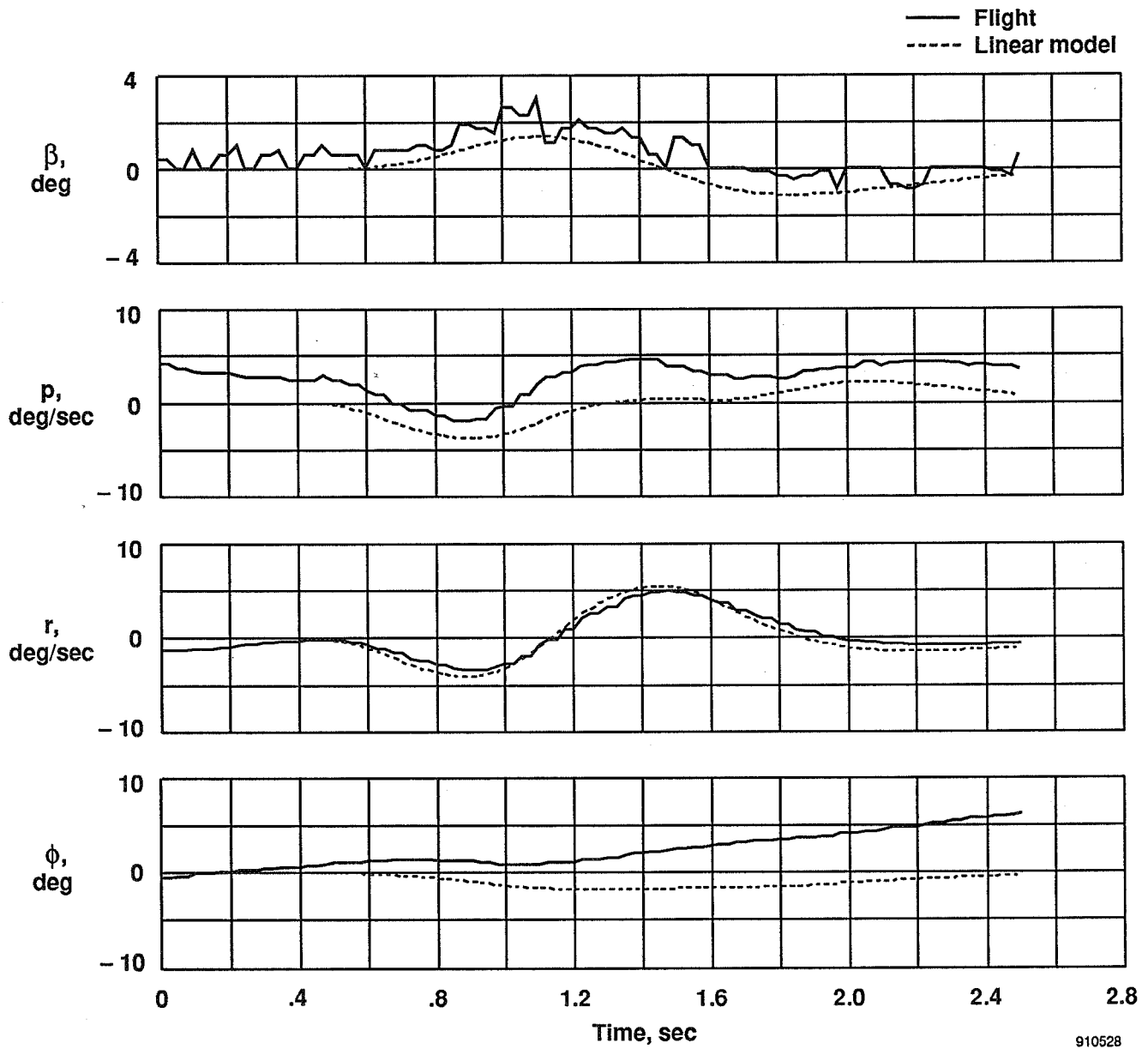
(a)

Figure 19. Response to yaw doublet in the AR–UA mode; $M = 0.70$, $h = 20,000$ ft.

69
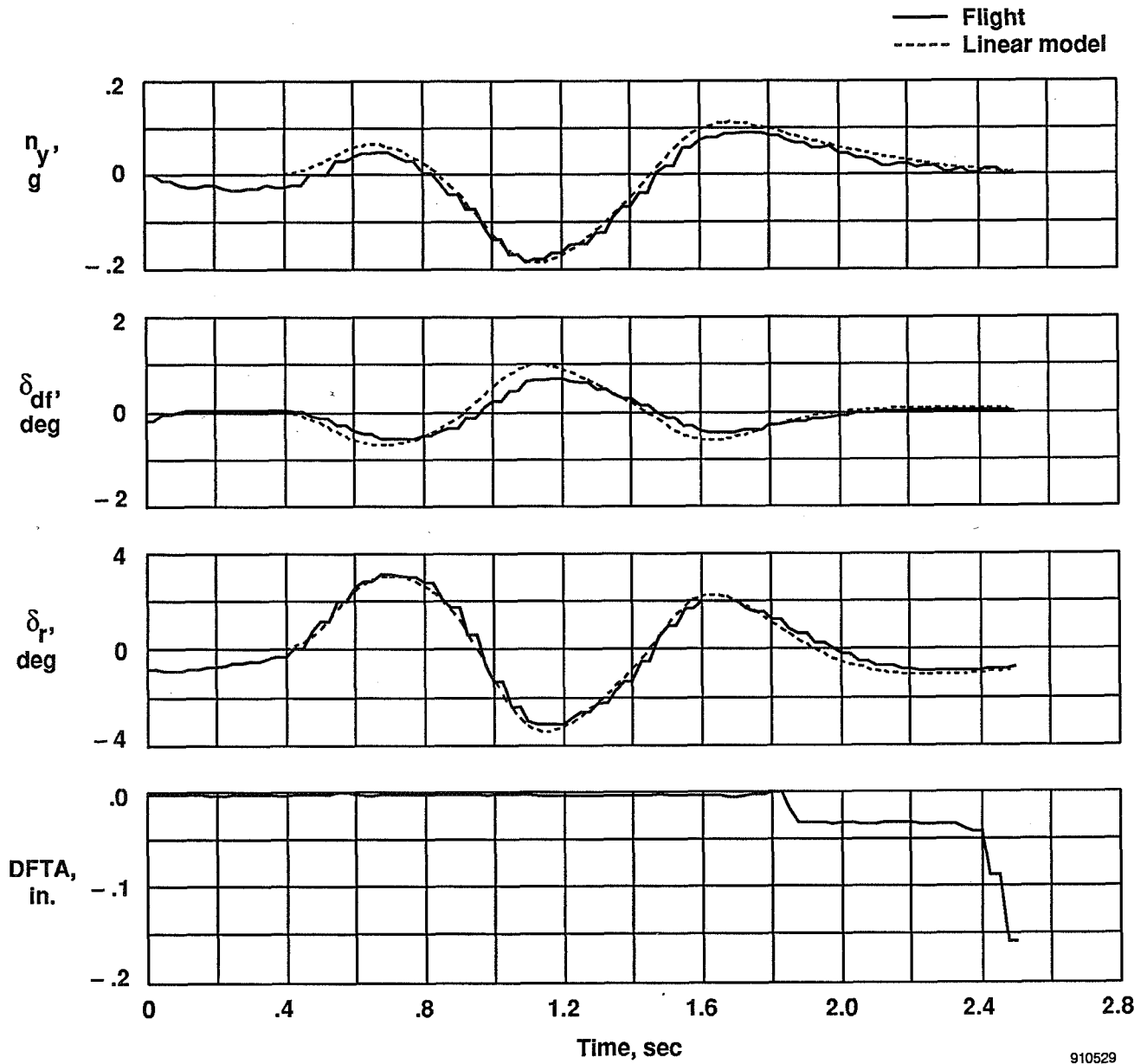
Figure 19. Continued.
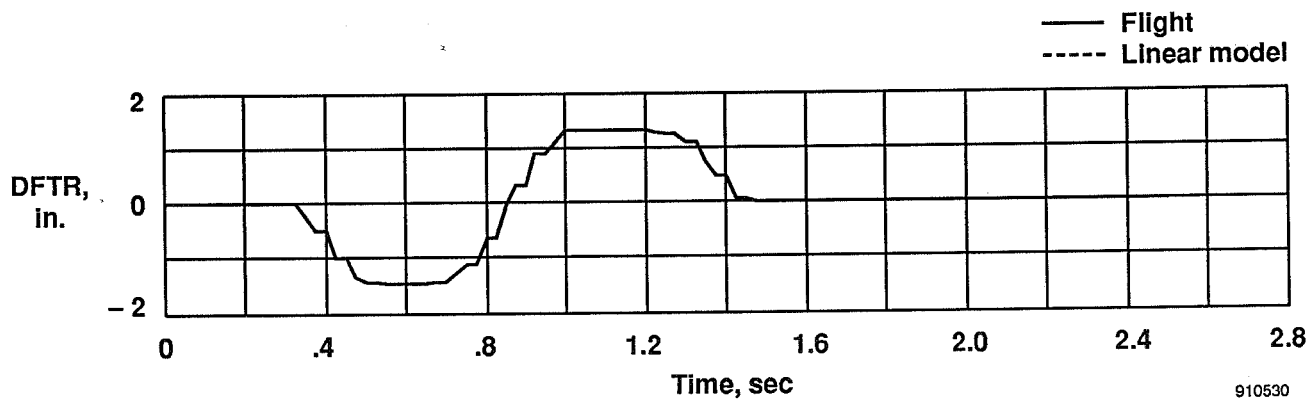
70

(c)

Figure 19. Concluded.
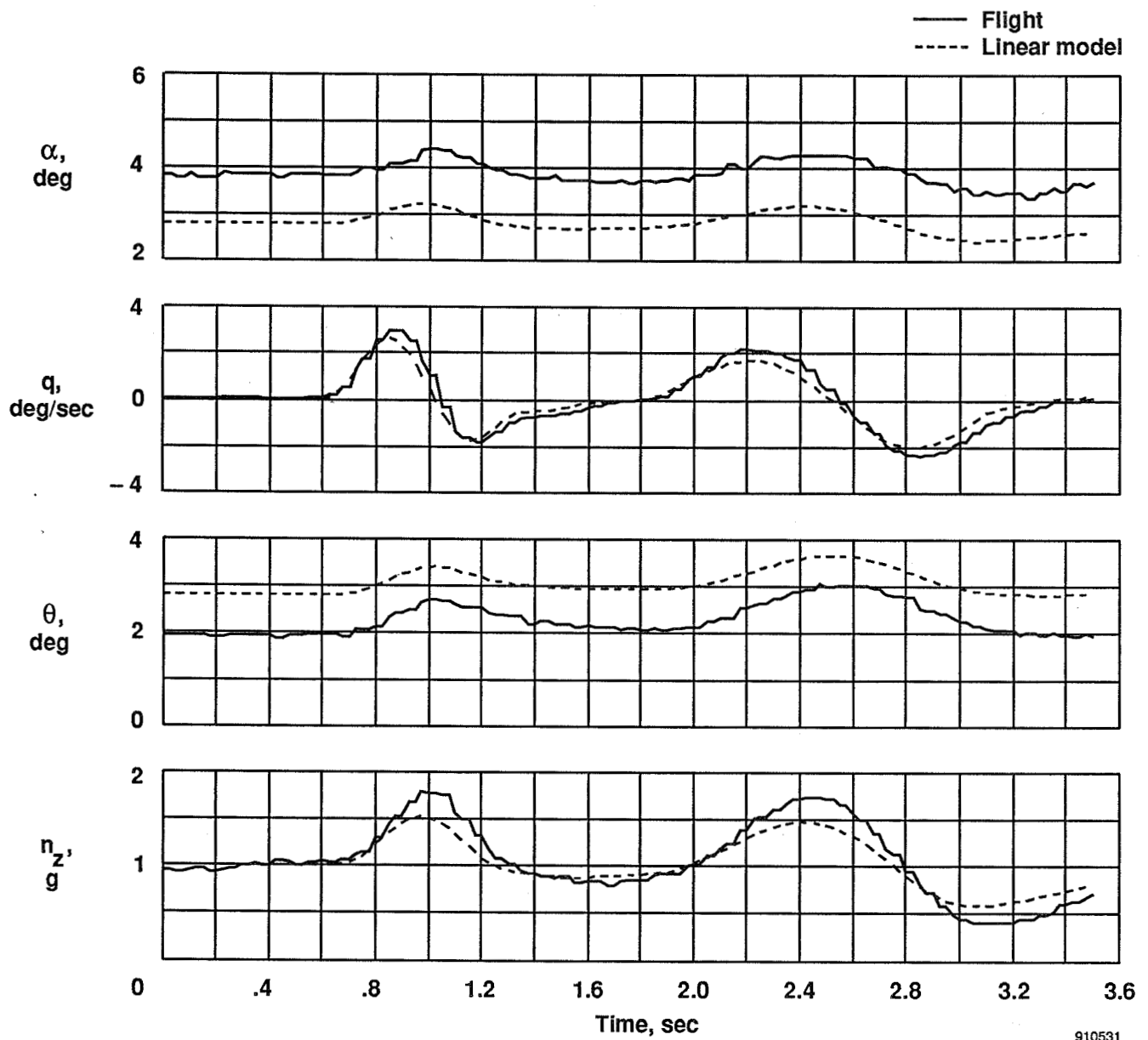
(a)

Figure 20. Response to pitch doublet in the ND–UA mode; $M = 0.90$, $h = 8,000$ ft.
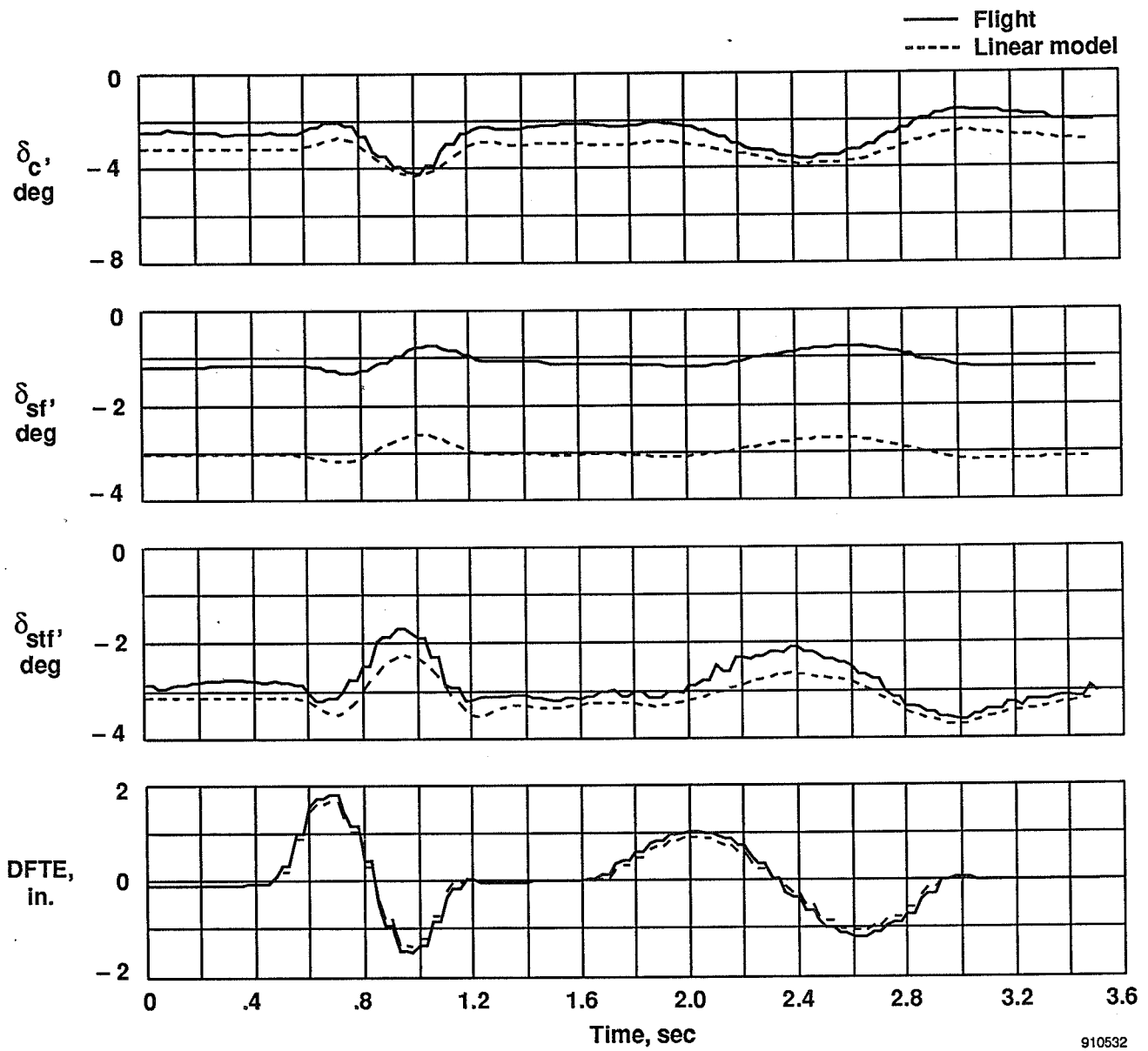
(b)

Figure 20. Concluded.
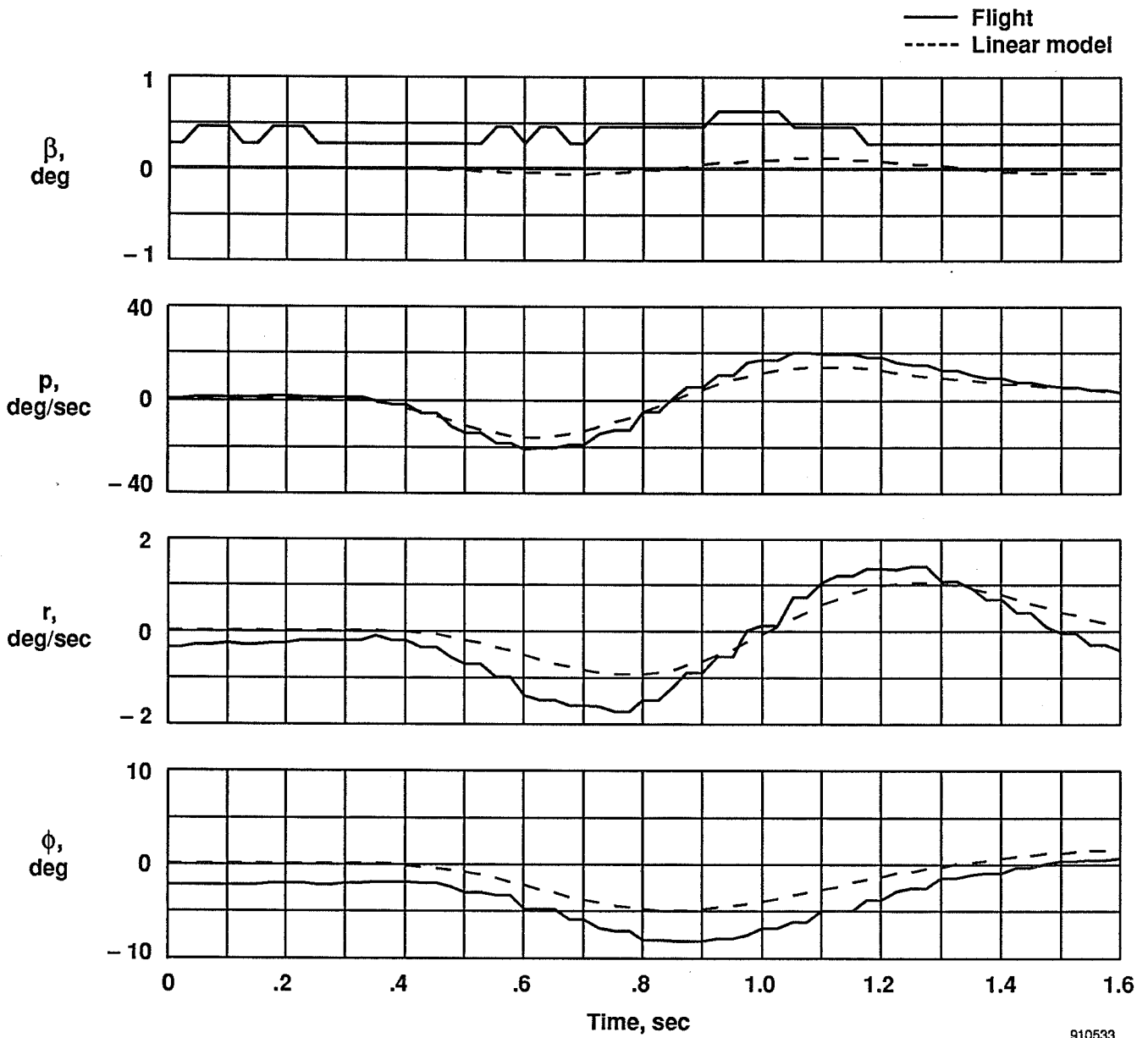
Figure 21. Response to roll doublet in the ND–UA mode; $M = 0.90$, $h = 8,000$ ft.

(a)
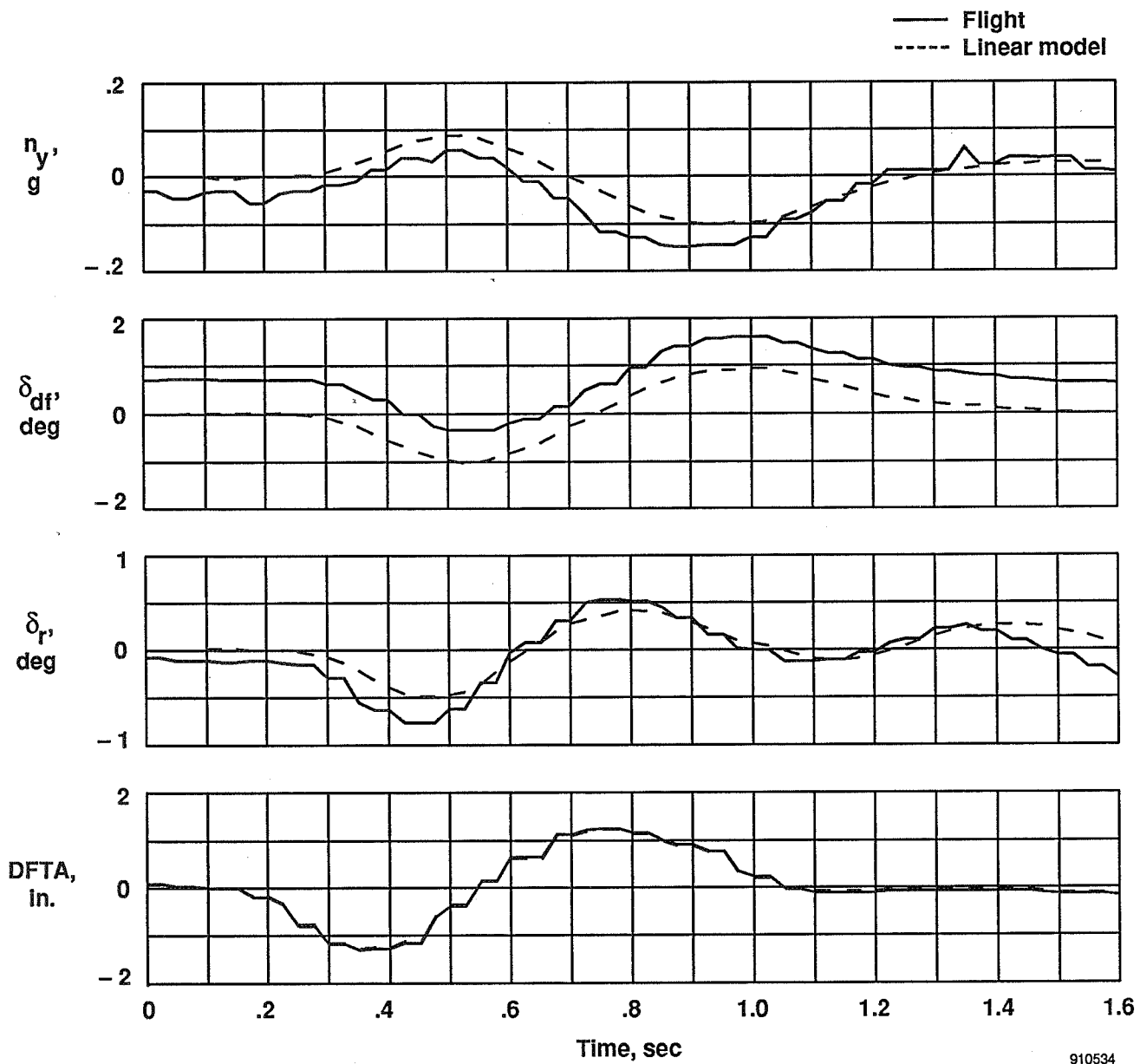
(b)

Figure 21. Continued.
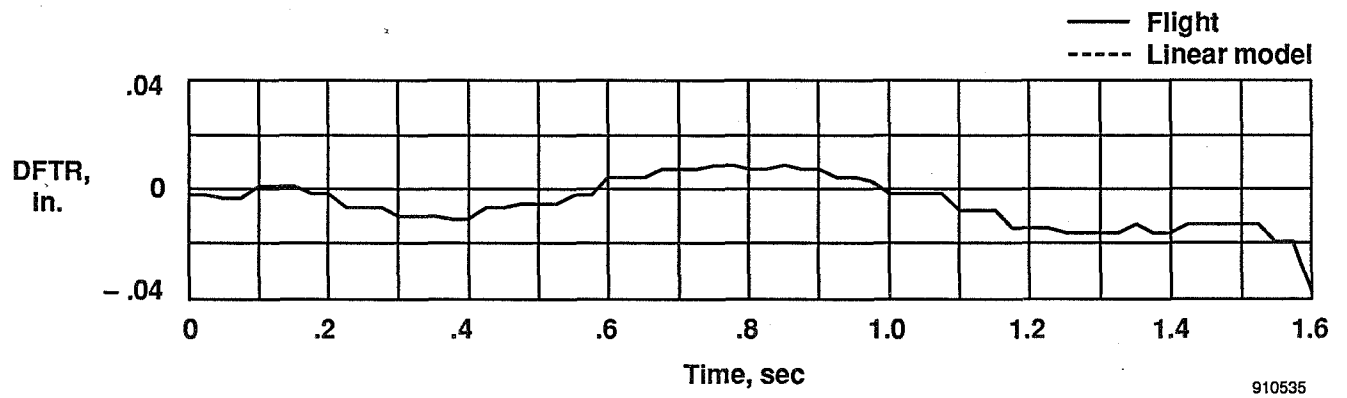
(c)

Figure 21. Concluded.
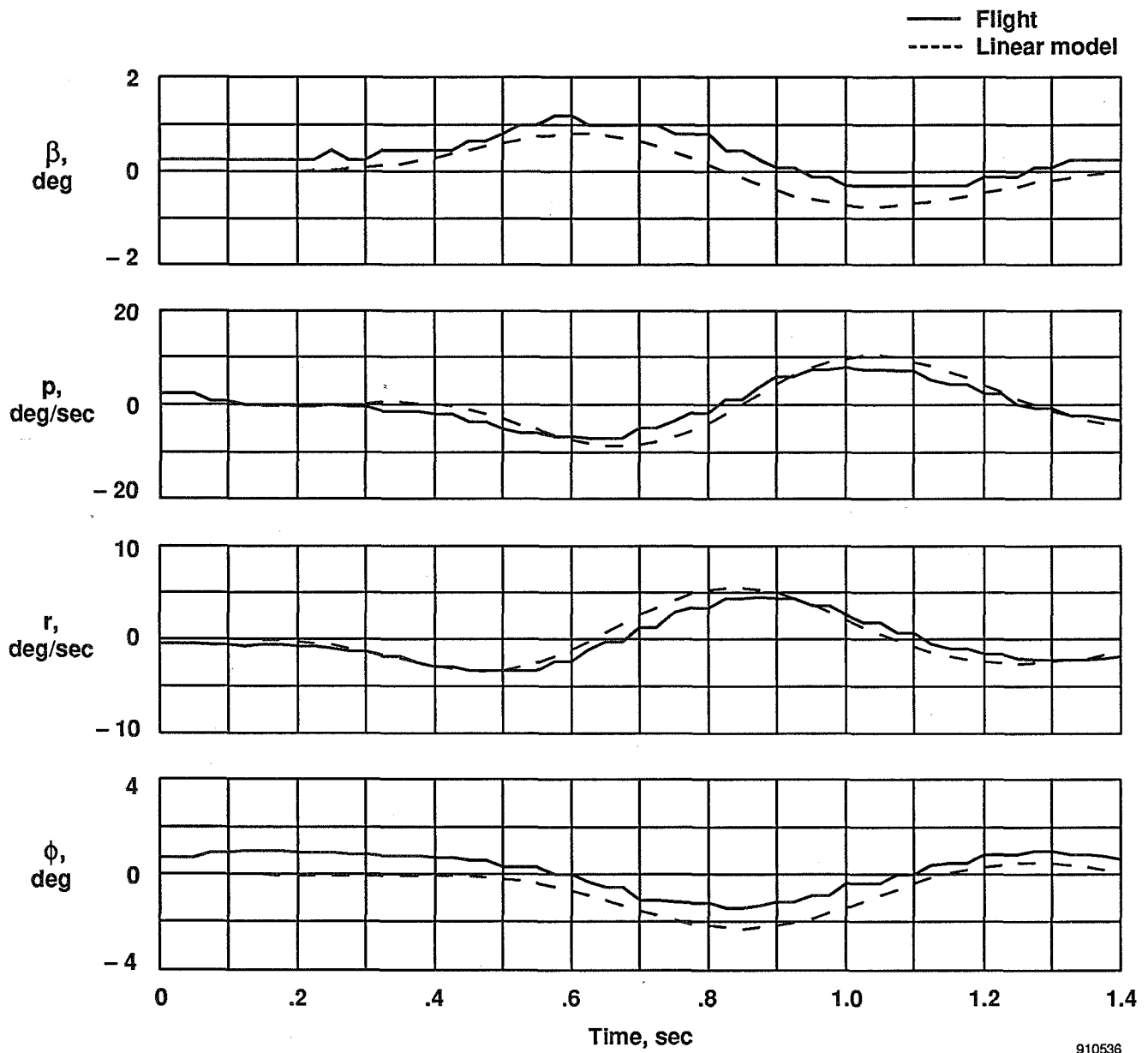
(a)

Figure 22. Response to yaw doublet in the ND–UA mode; $M = 0.90$, $h = 8,000$ ft.
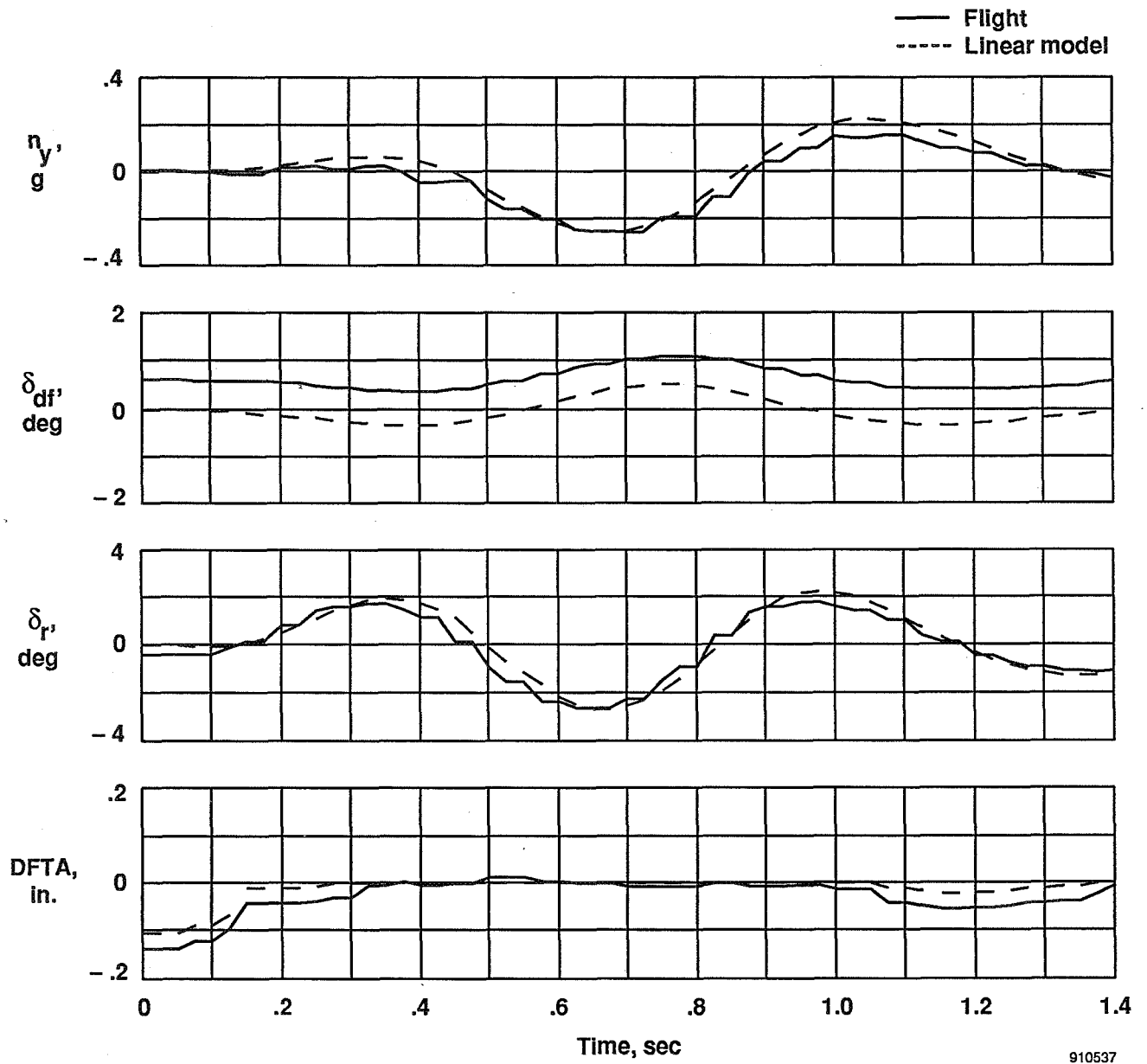
77

(b)

Figure 22. Continued.
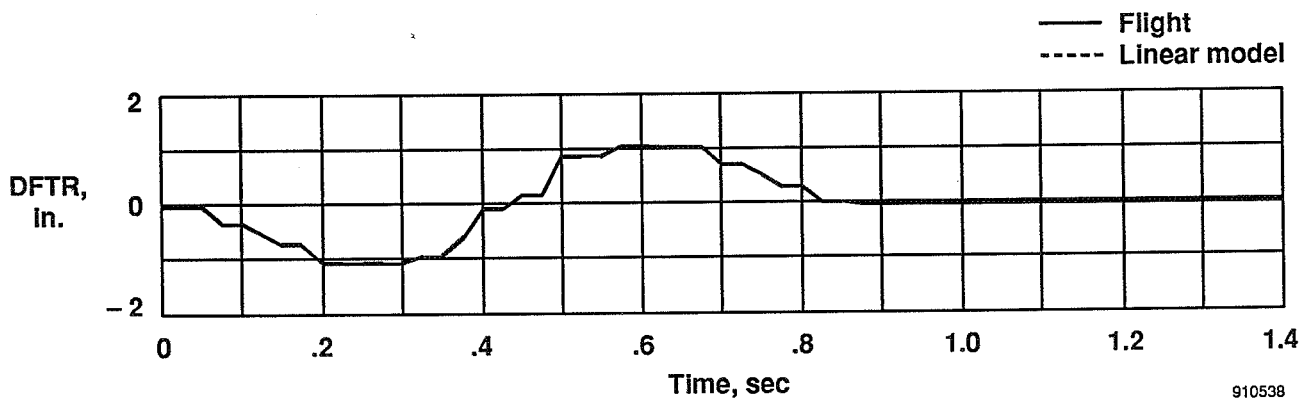
(c)

Figure 22. Concluded.
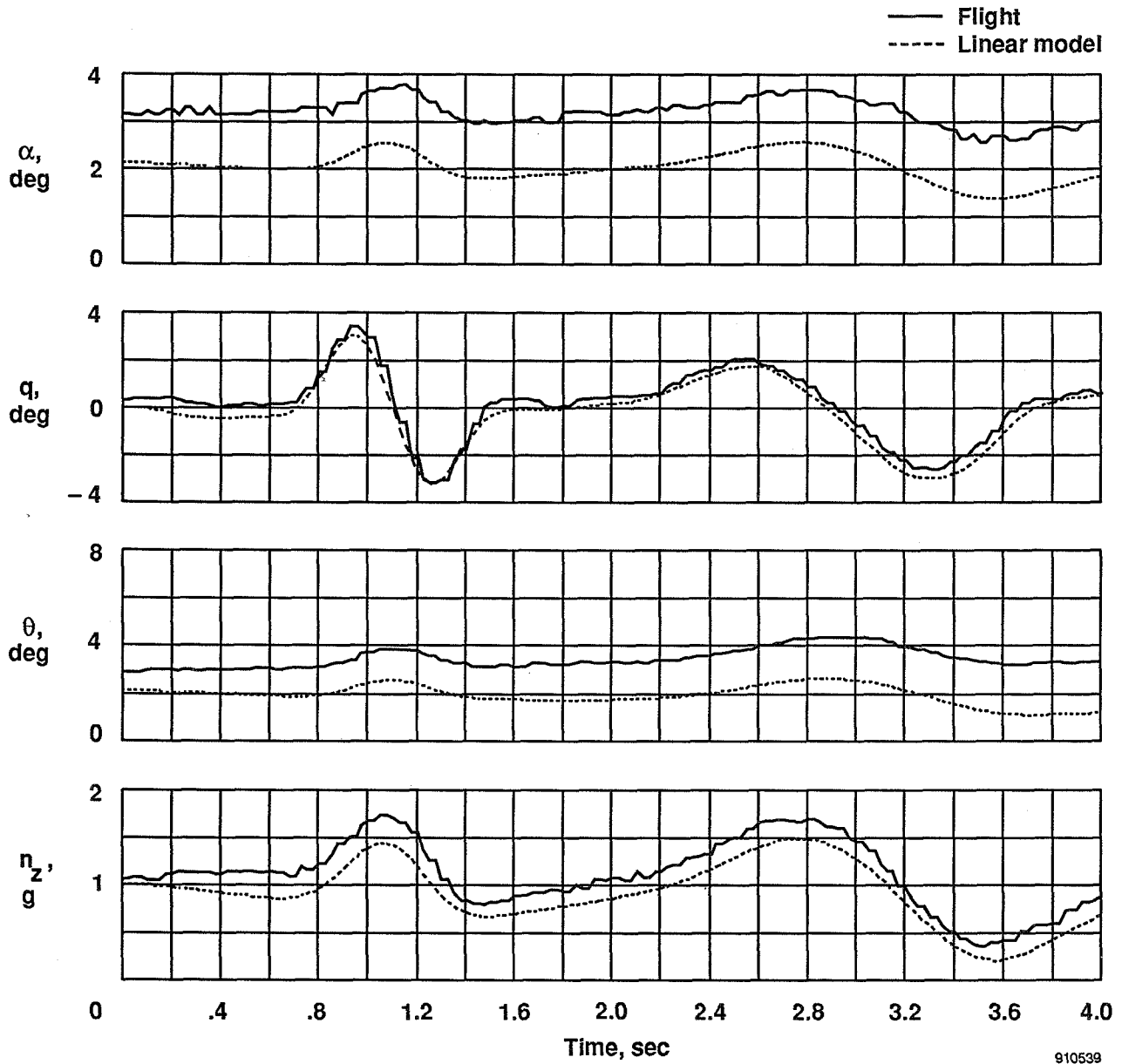
(a)

Figure 23. Response to pitch doublet in the AR–UA mode; $M = 0.90$, $h = 8,000$ ft.
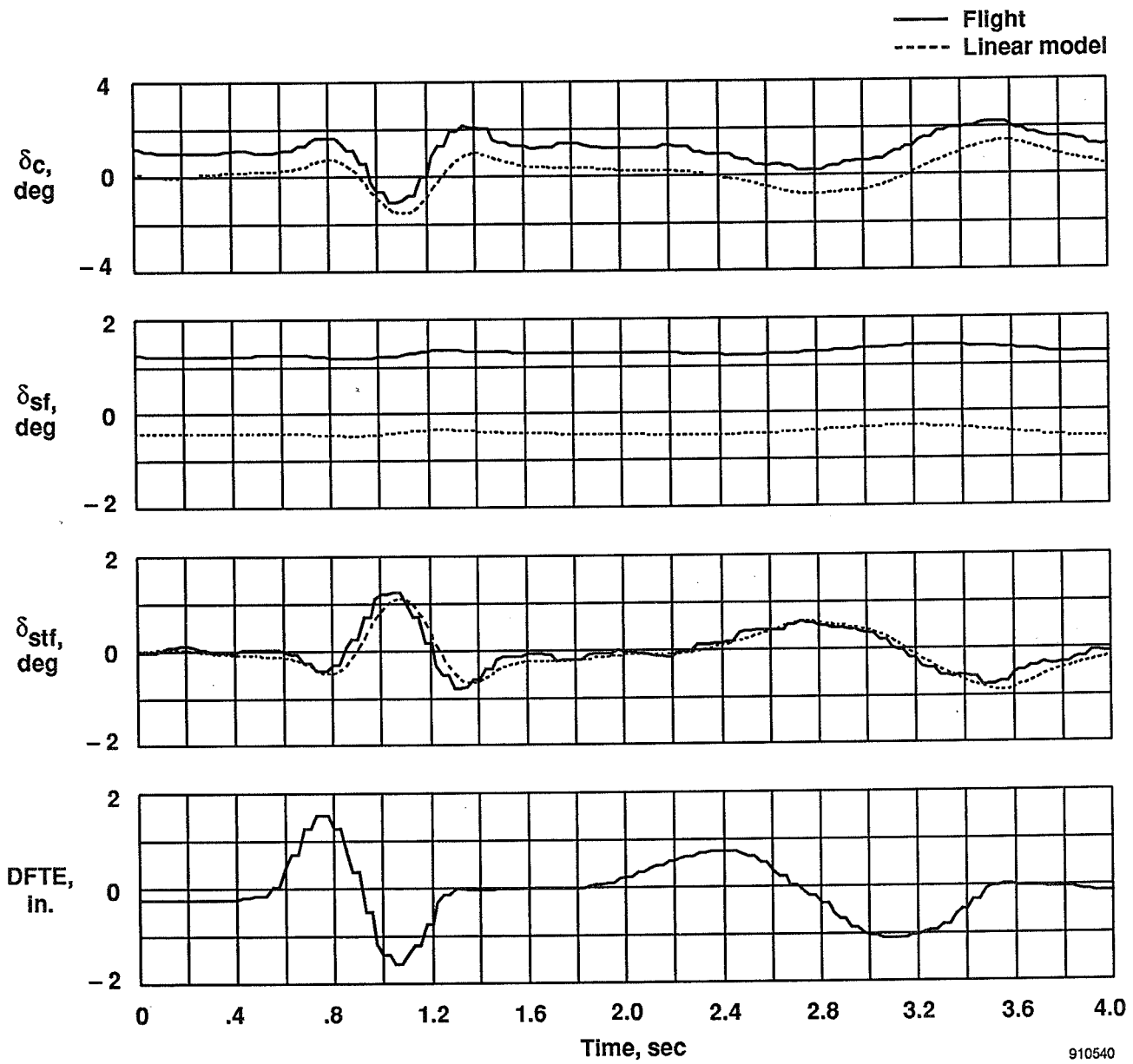
(b)

Figure 23. Concluded.
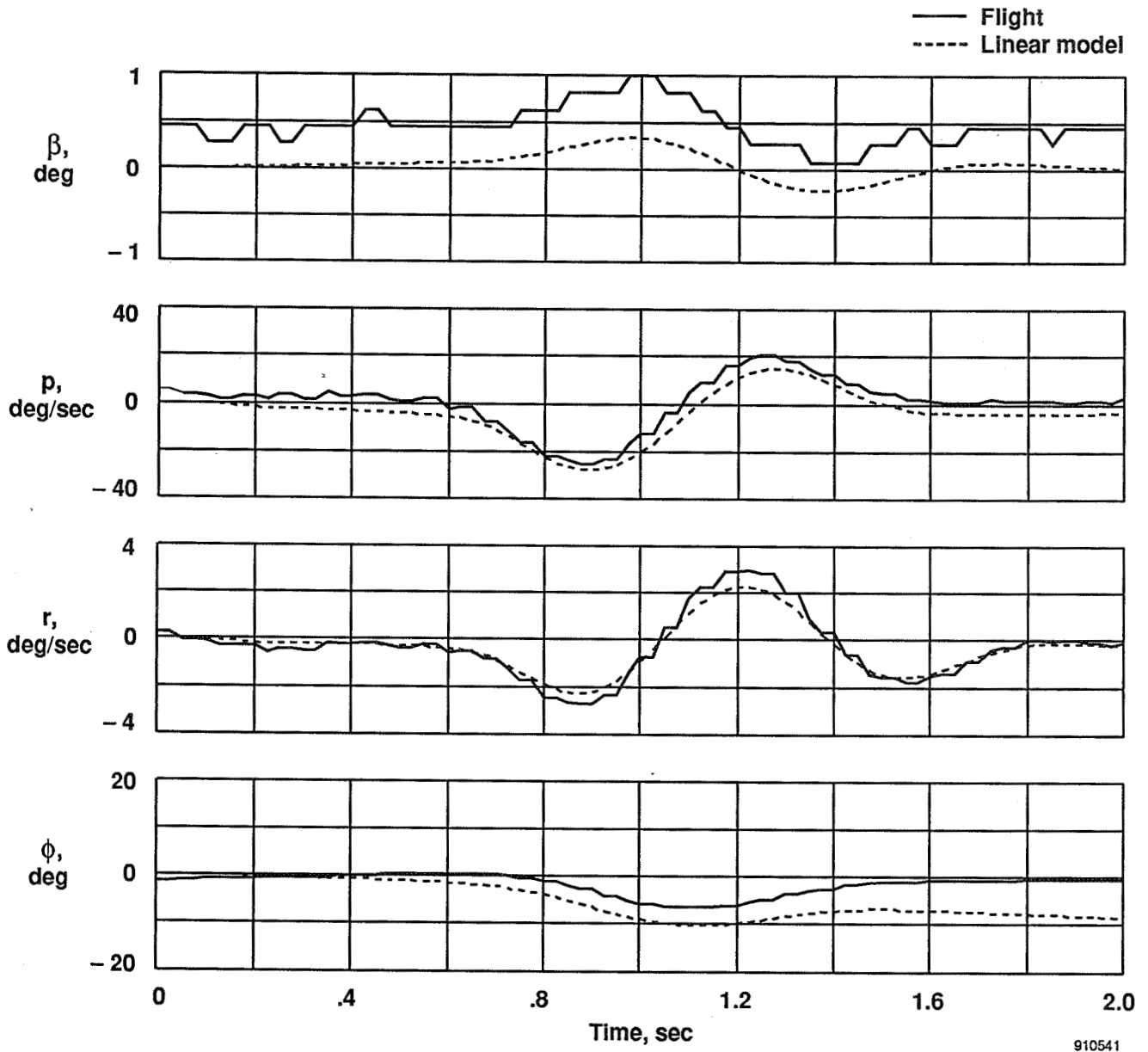
(a)

Figure 24. Response to roll doublet in the AR–UA mode; $M = 0.90$, $h = 8,000$ ft.
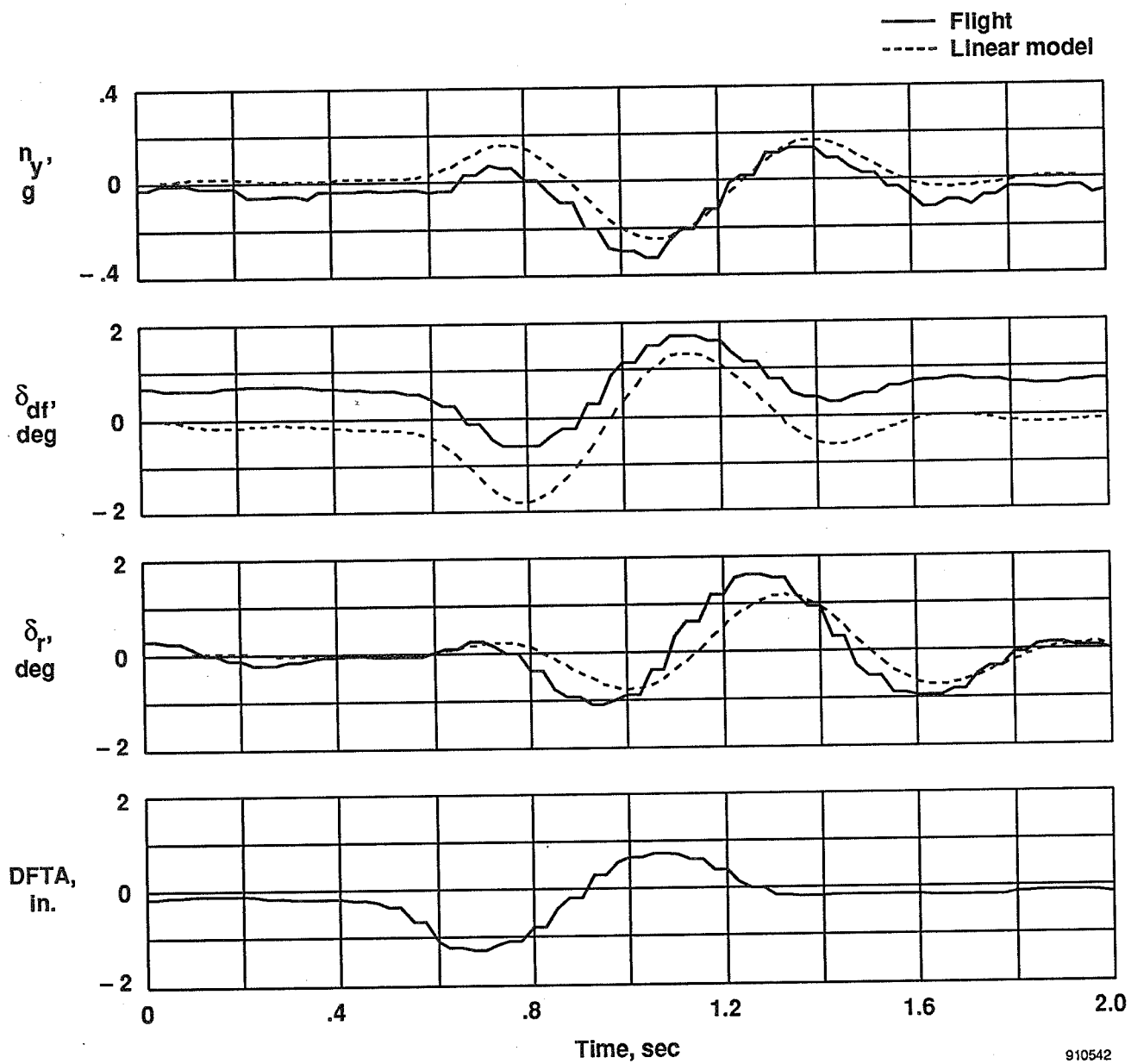
(b)

Figure 24. Continued.
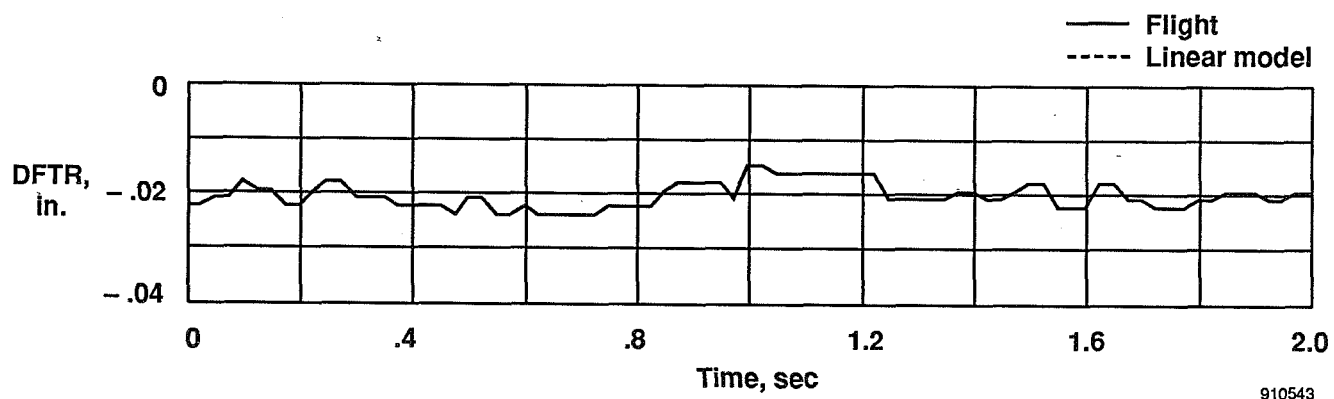
910542

83

(c)

Figure 24. Concluded.
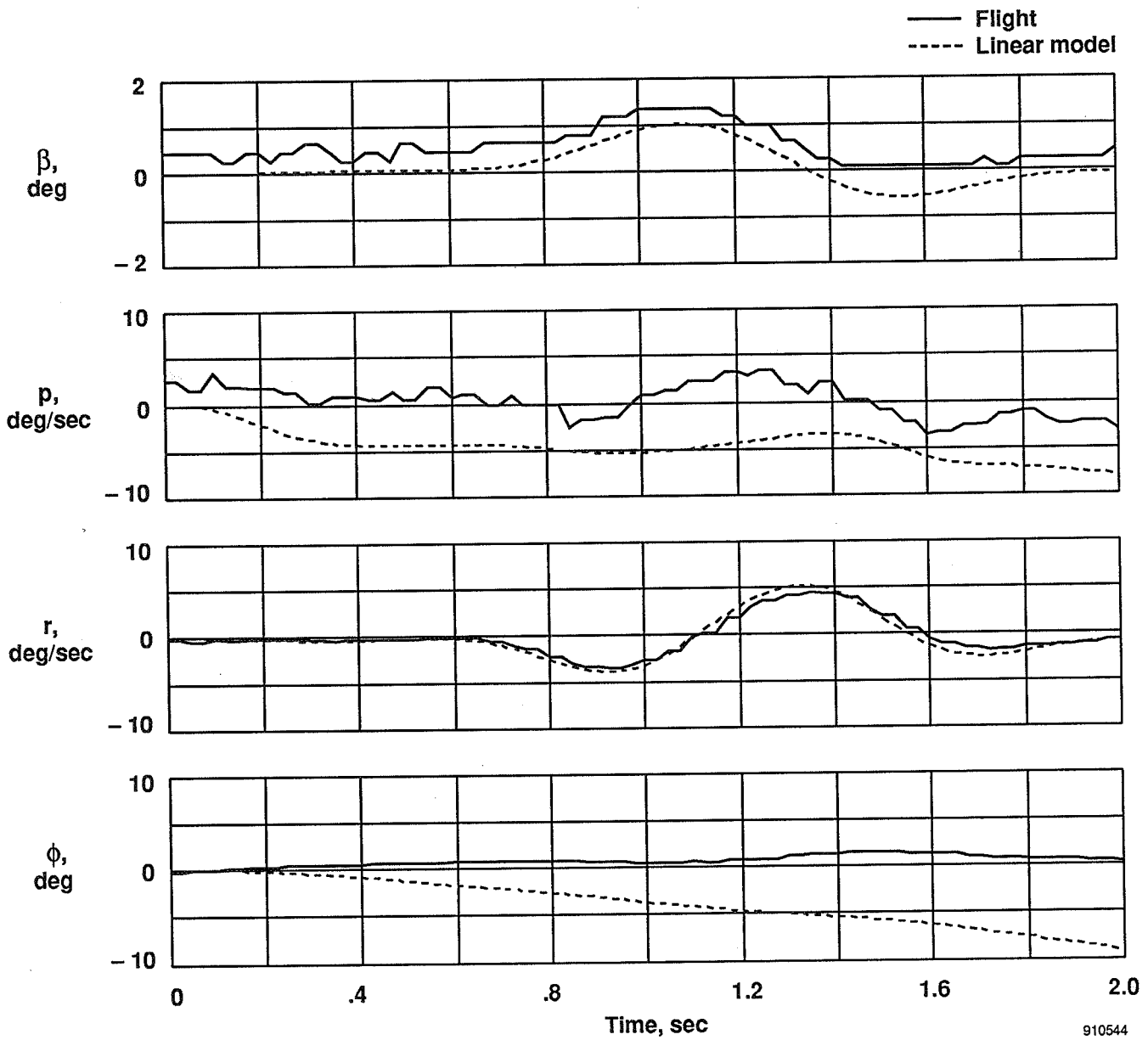
(a)

Figure 25. Response to yaw doublet in the AR–UA mode; $M = 0.90$, $h = 8,000$ ft.

85
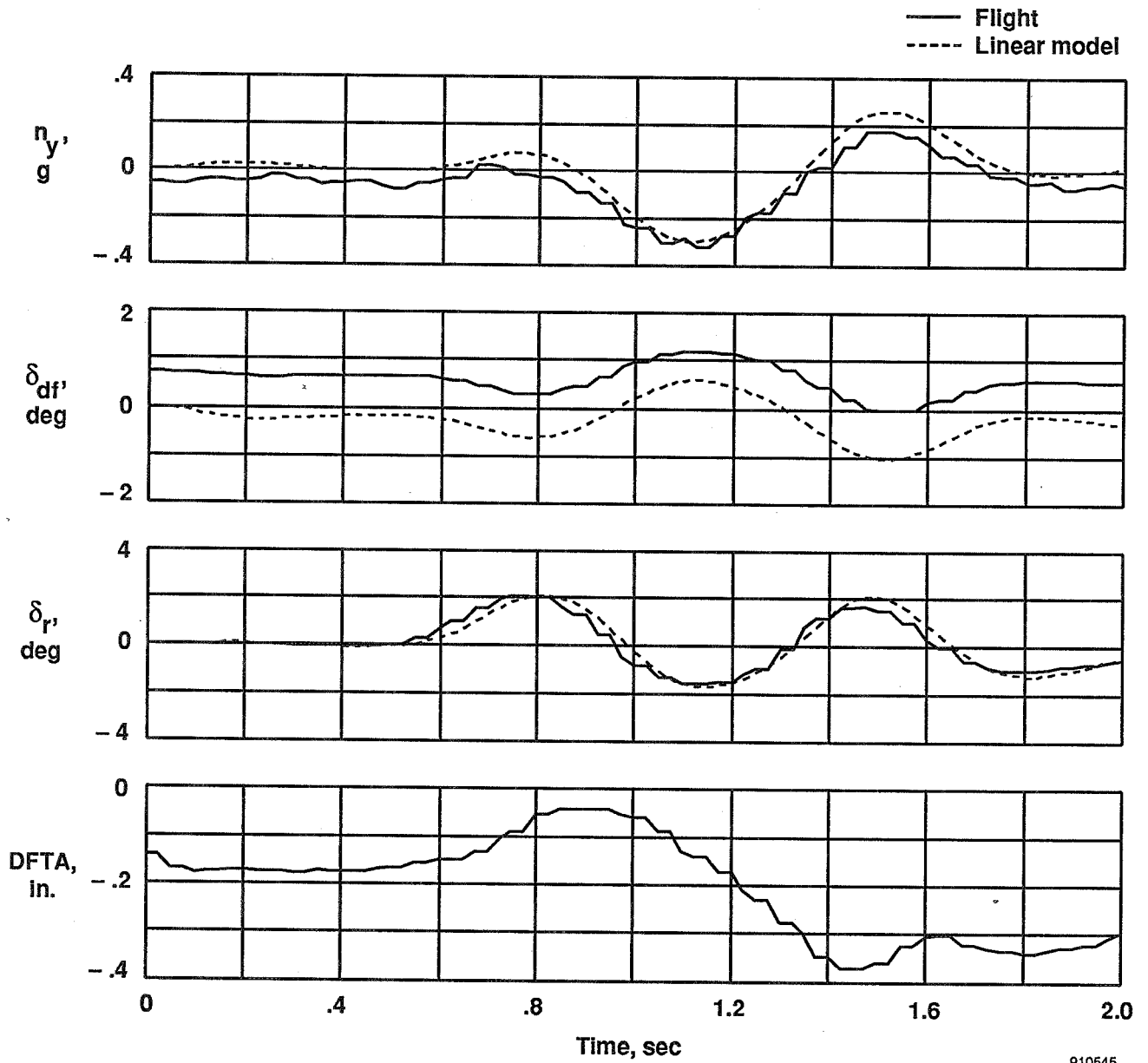
(b)

Figure 25. Continued.
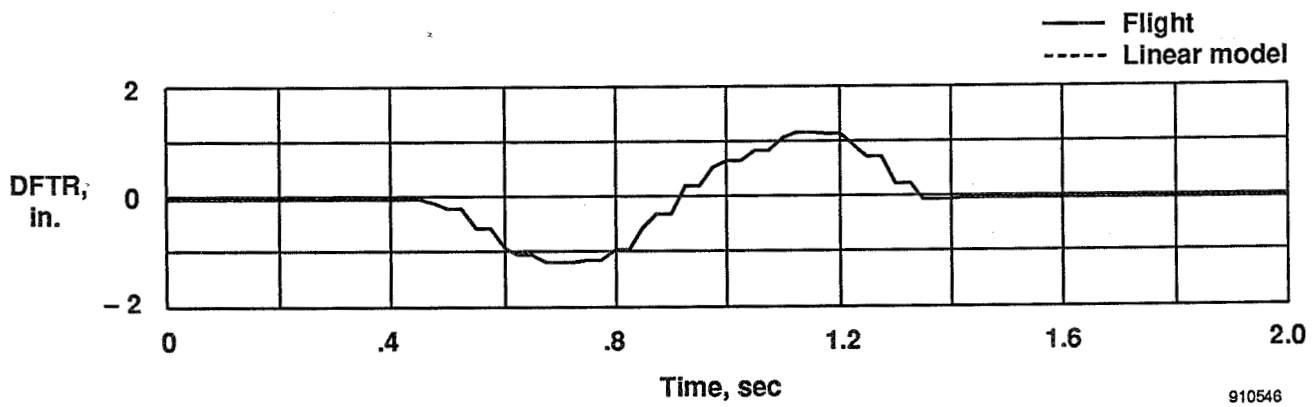
(c)

Figure 25. Concluded.
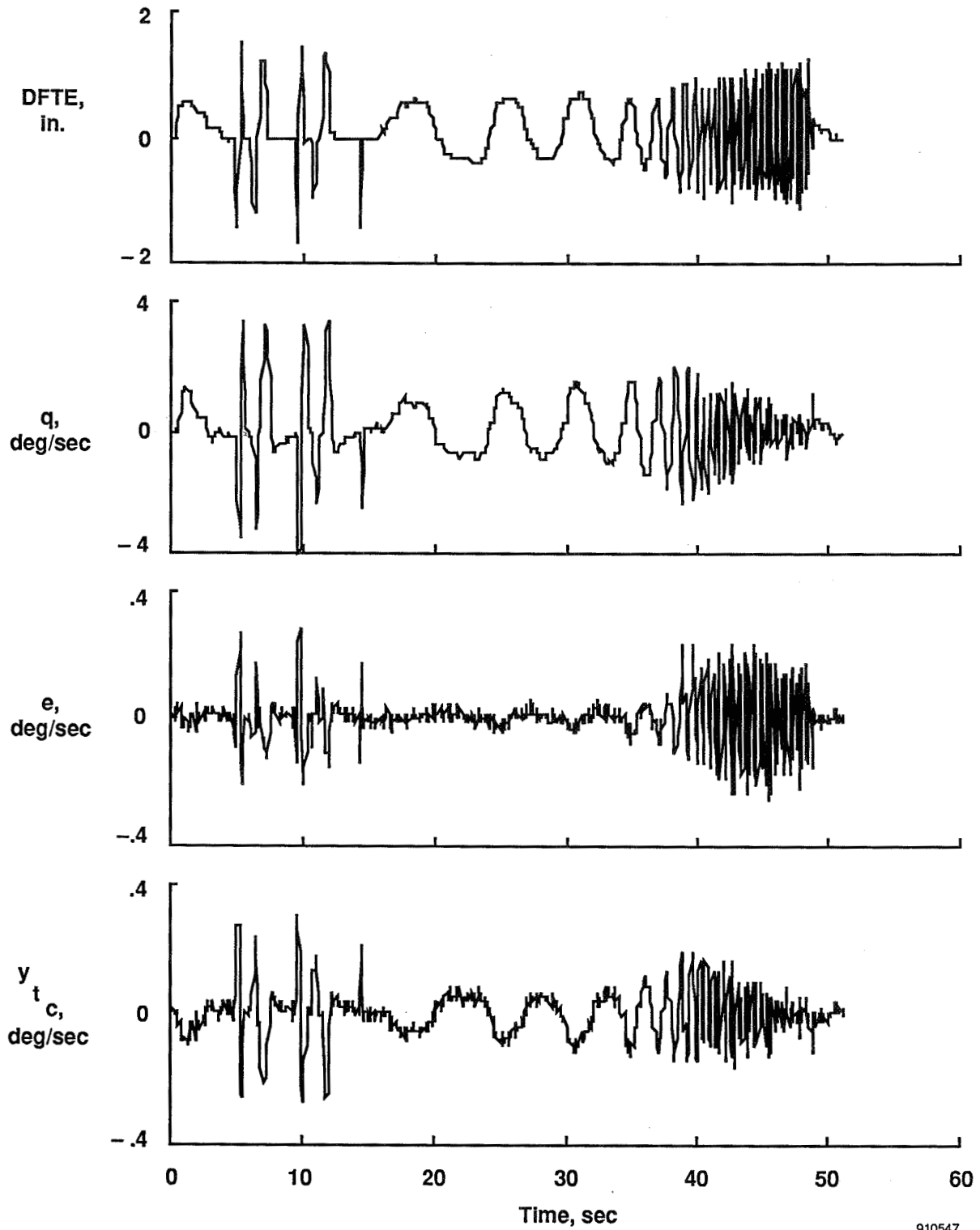
Figure 26. Time history of pilot-generated frequency sweep.

910547
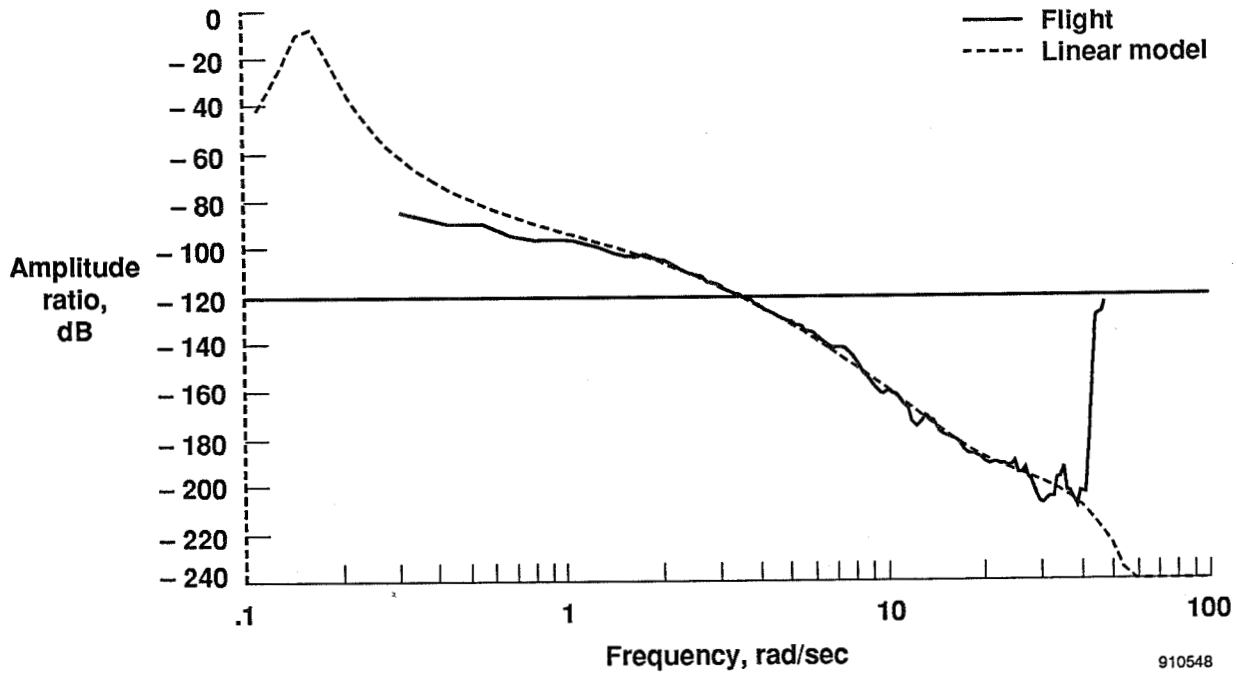
(a)
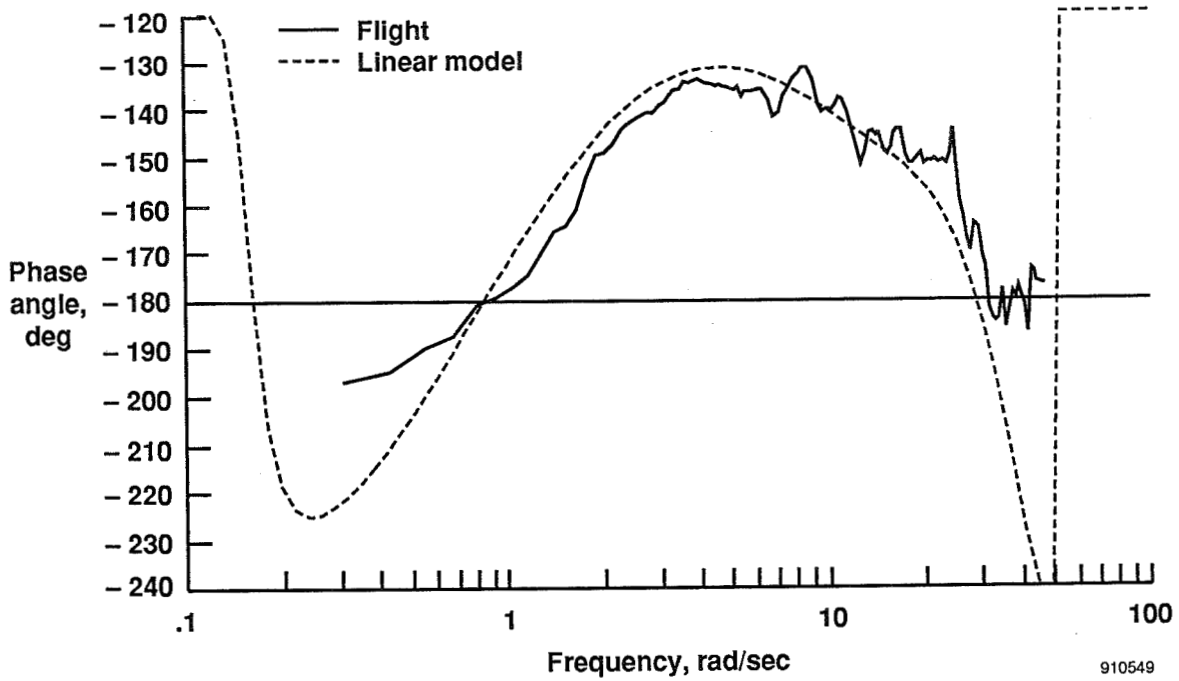
(b)

Figure 27. Open-loop frequency response ($\frac{y_{tc}}{e}$), AR–PA mode; $M = 0.258$, $h = 4,000$ ft.

89
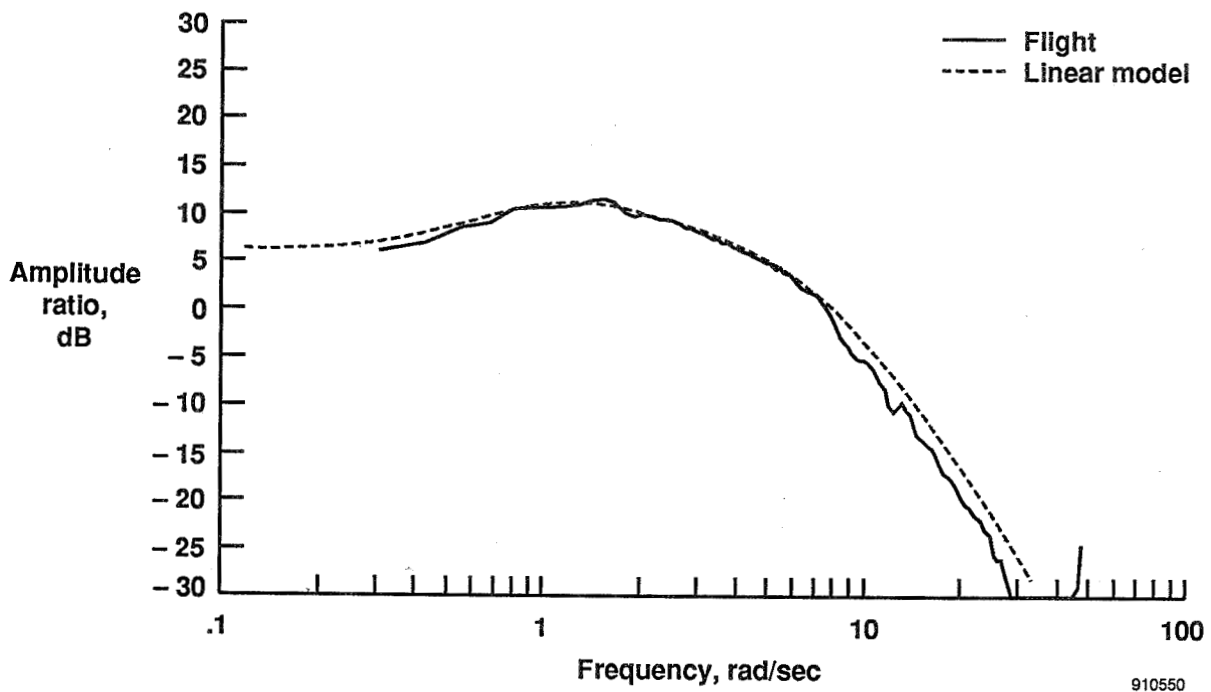
(a)
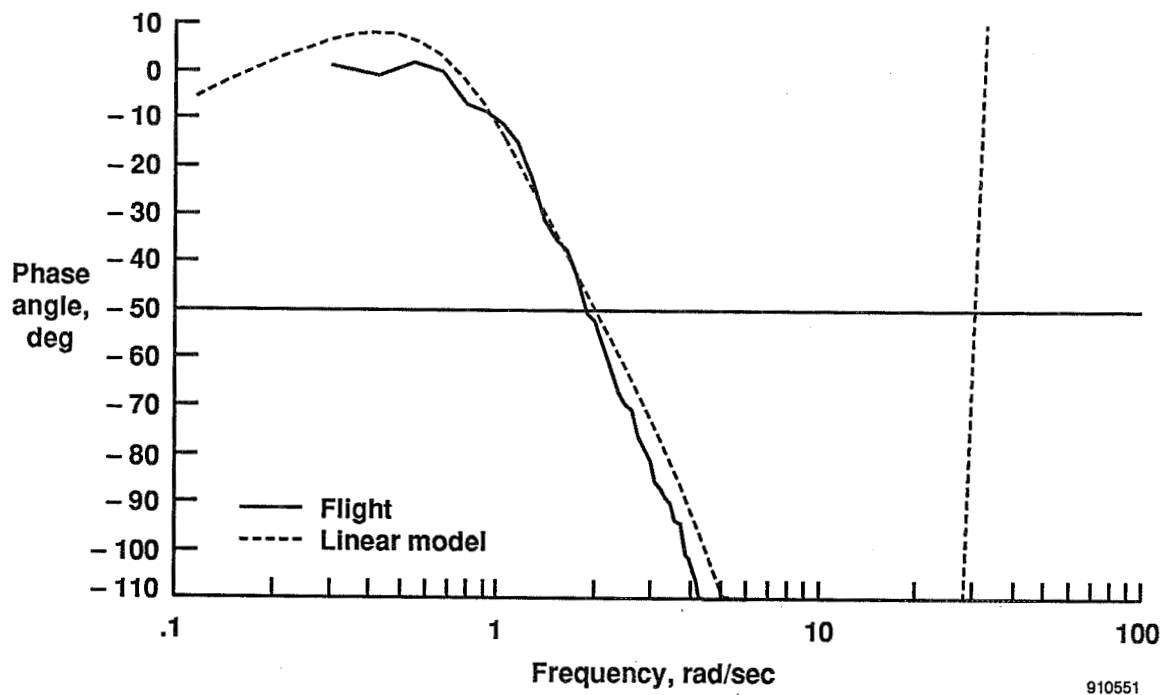
(b)

Figure 28. Pitch rate due to longitudinal stick ($\frac{q}{DFTE}$), AR–PA mode; $M = 0.258$, $h = 4,000$ ft.

C-2
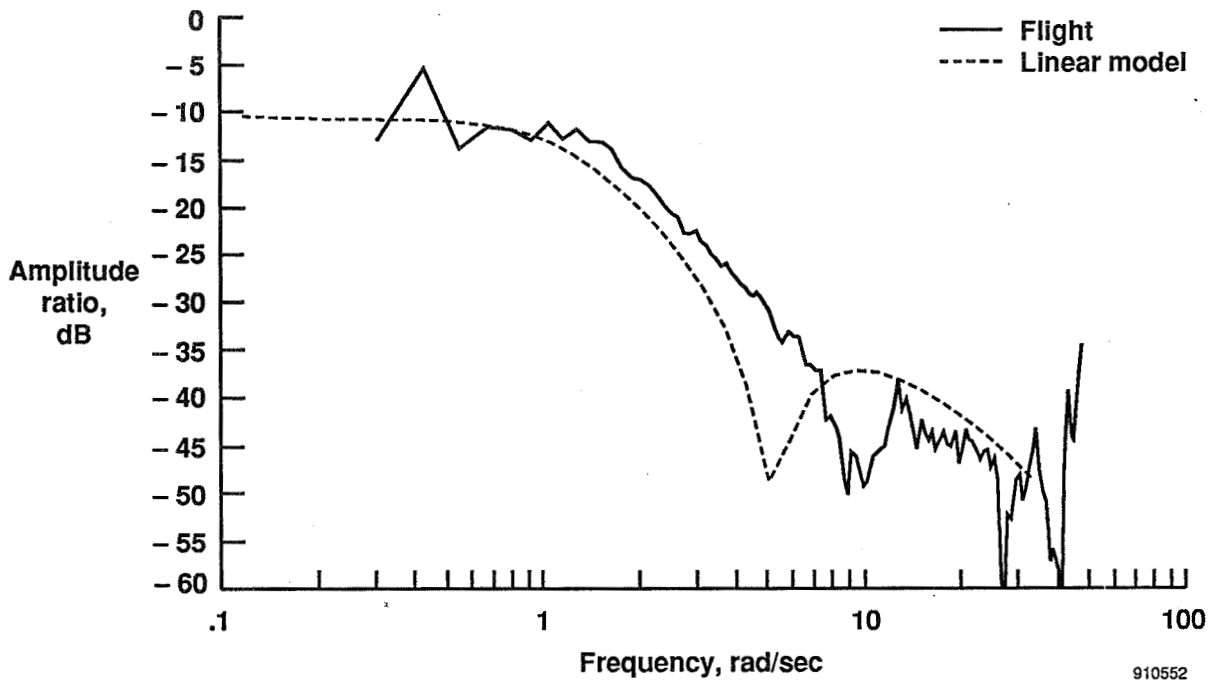
(a)
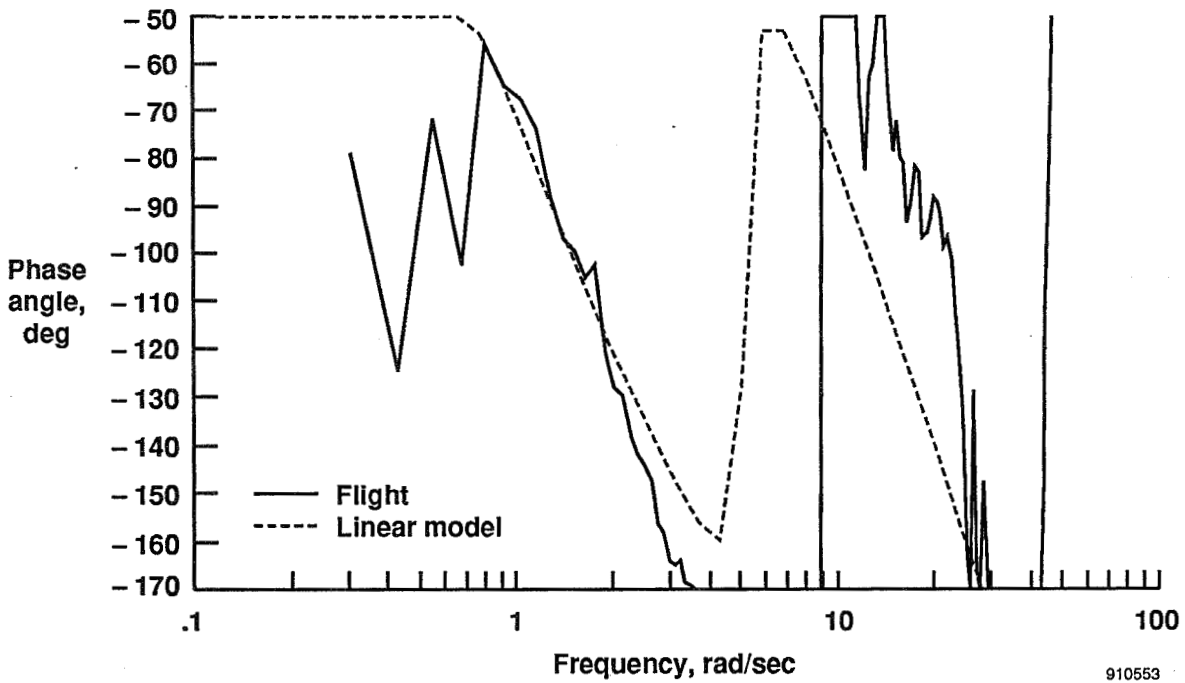
(b)

Figure 29. Normal acceleration due to longitudinal stick ($\frac{n_z}{DFTE}$), AR–PA mode; $M = 0.258$, $h = 4,000$ ft.
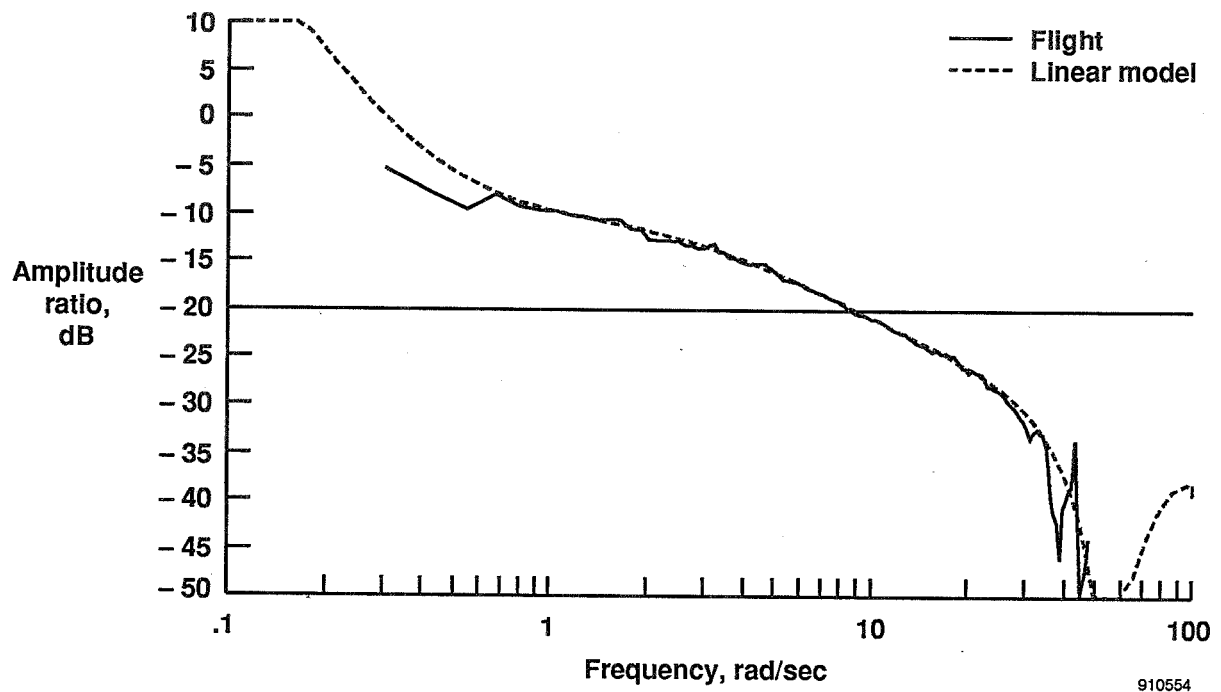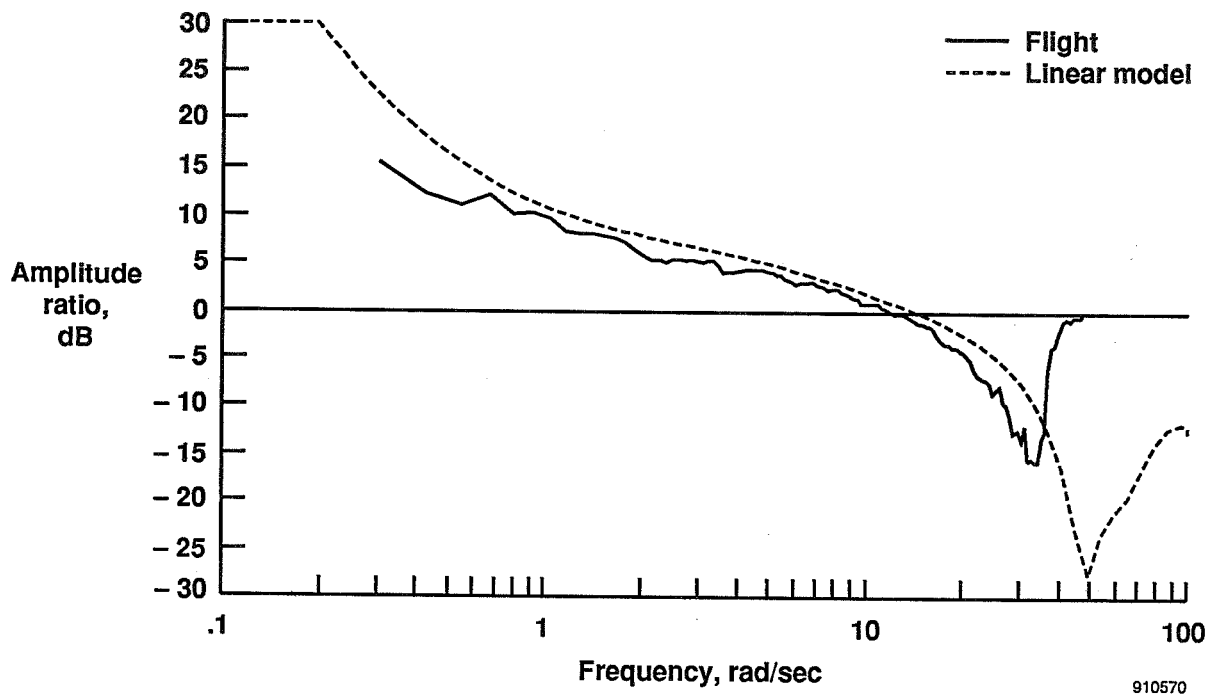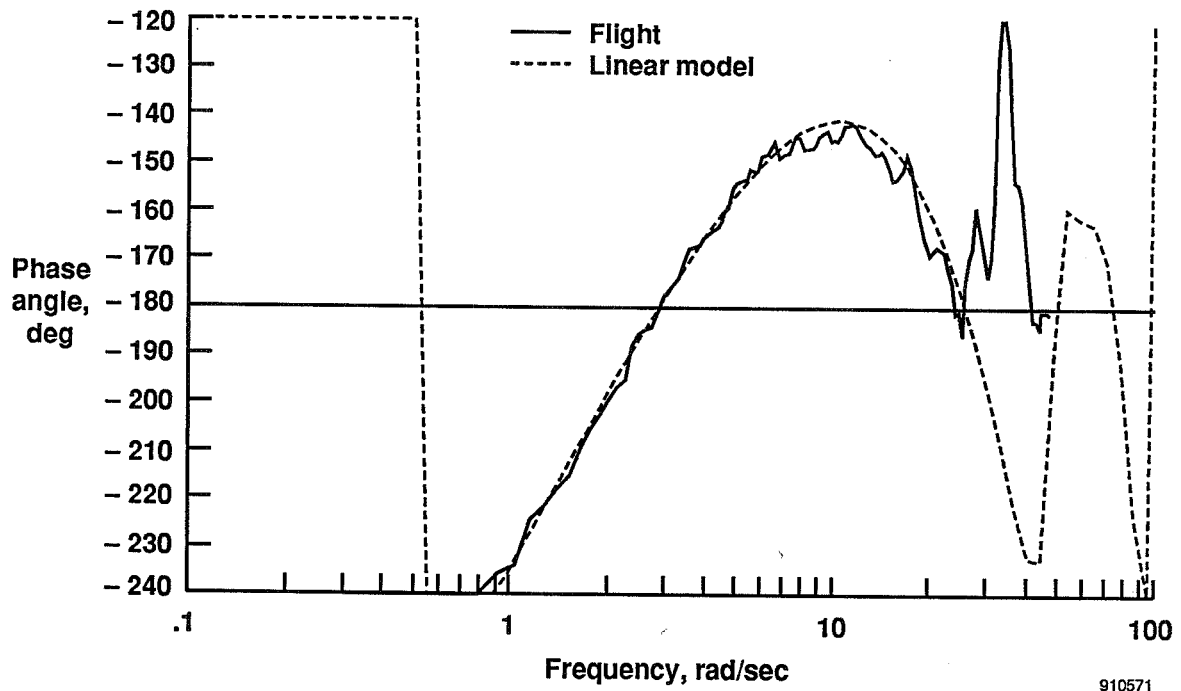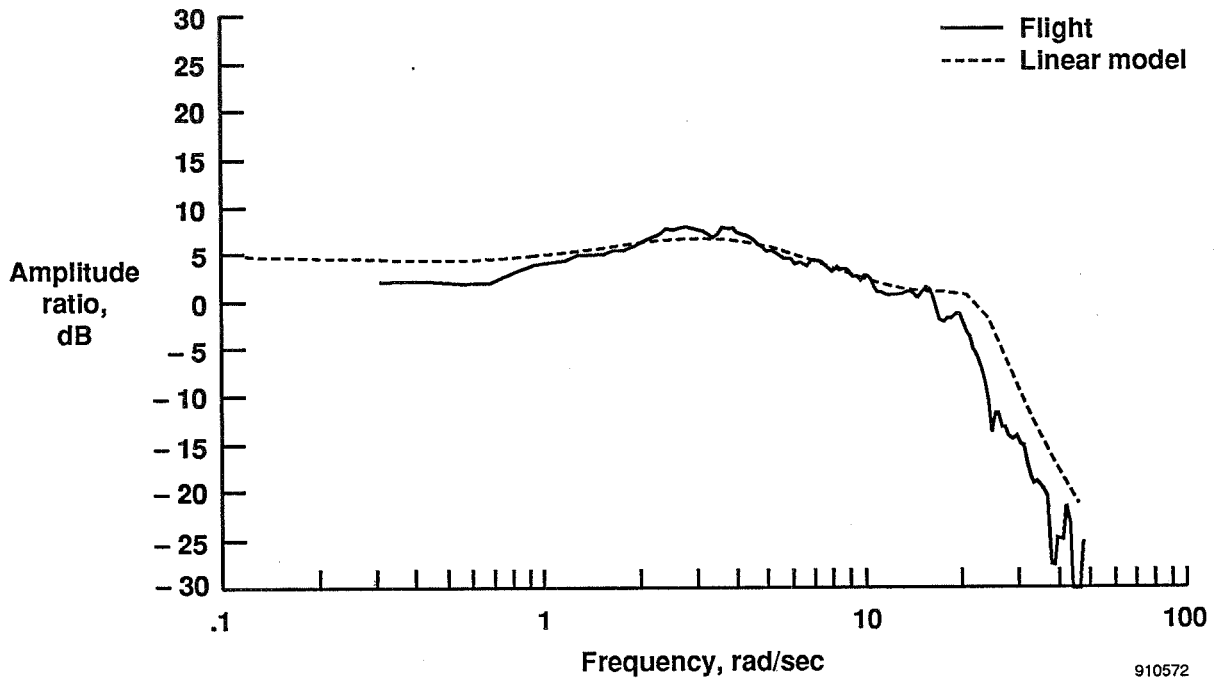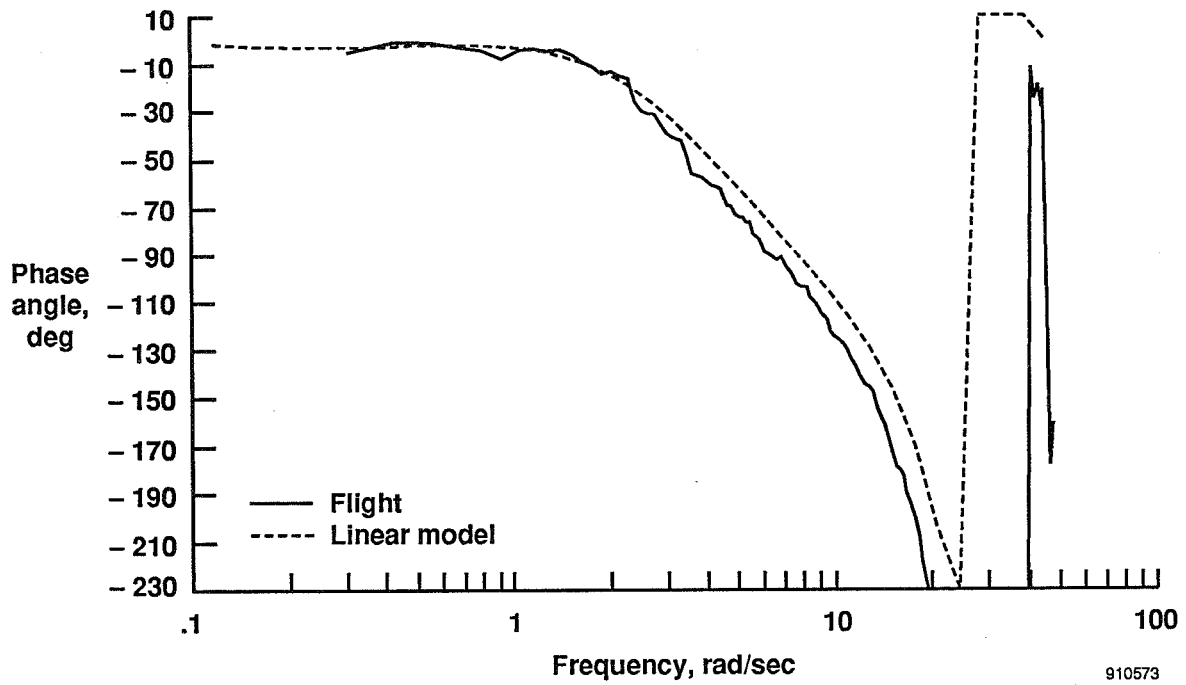
(a)
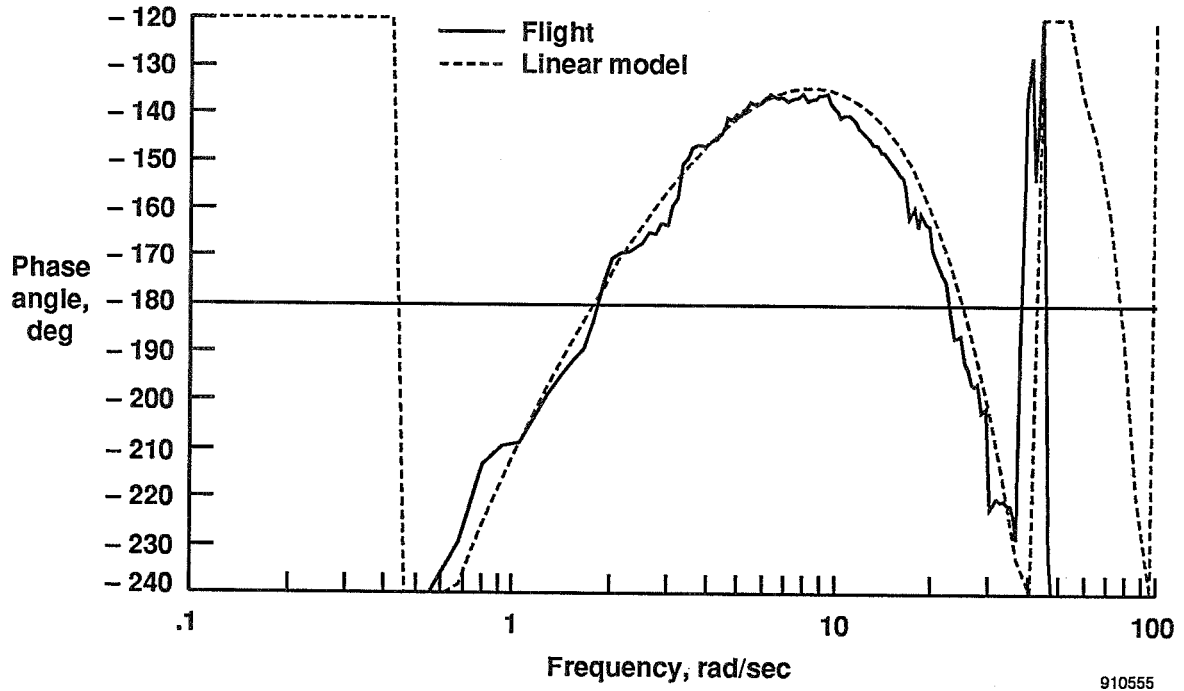
(b)

Figure 30. Open-loop frequency response ($\frac{y_{tc}}{e}$) ND–UA mode; $M = 0.70$, $h = 20,000$ ft.
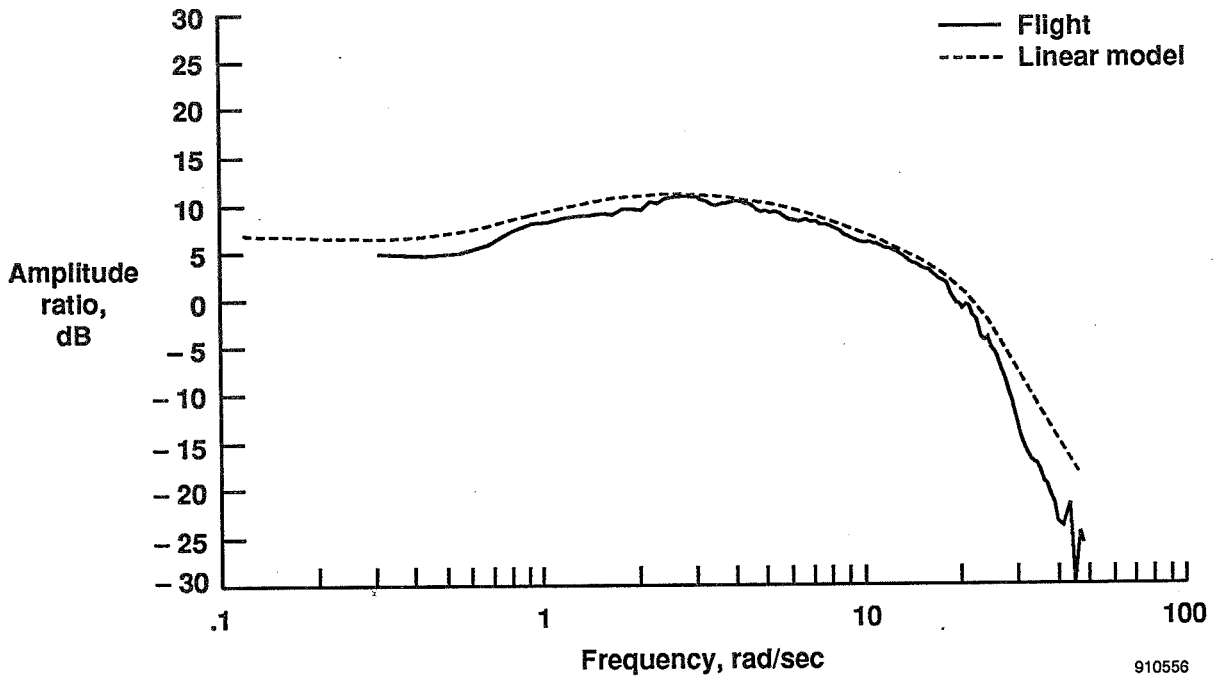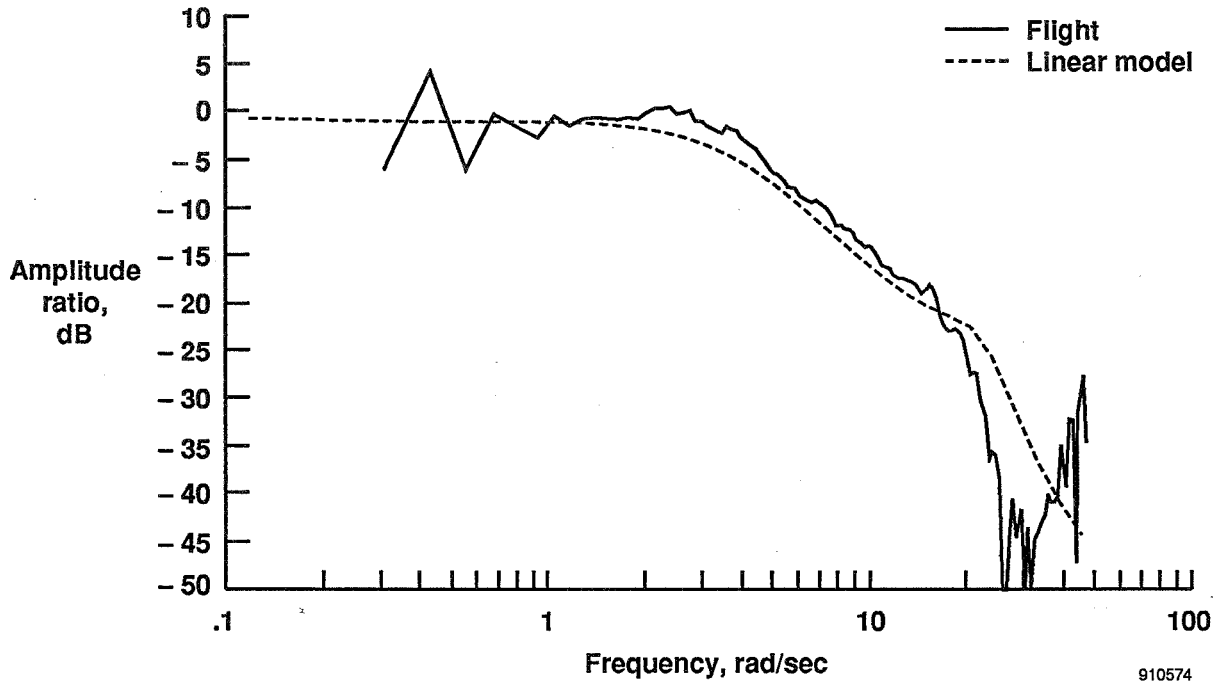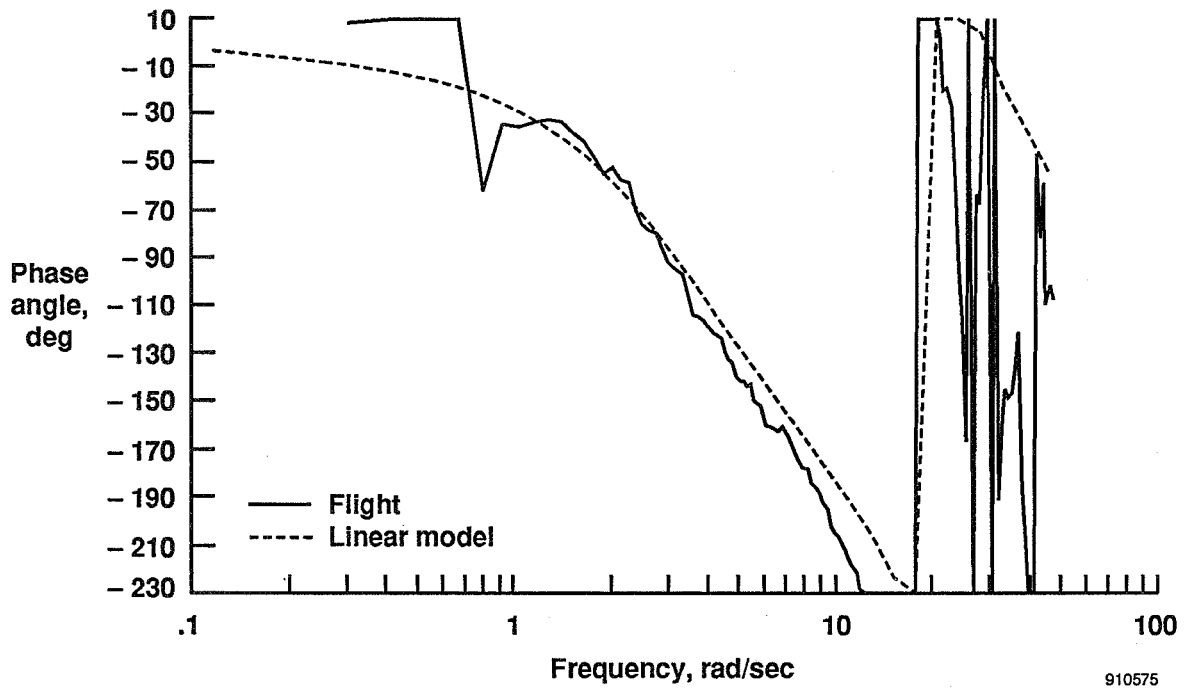
(a)
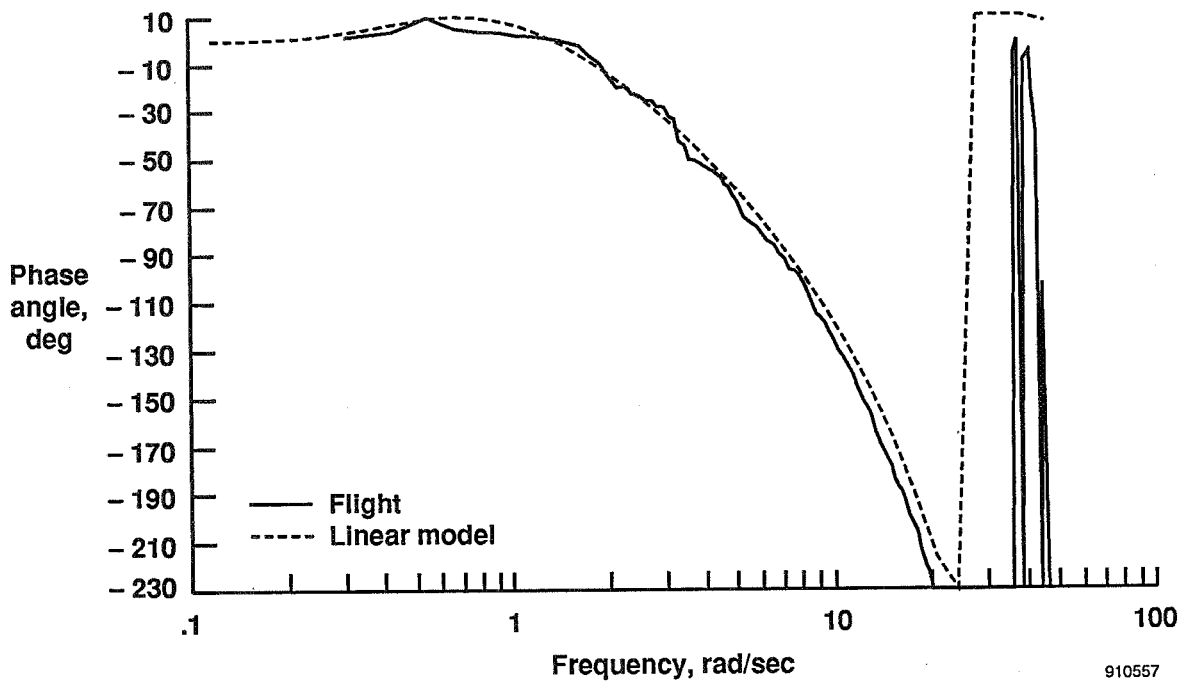
(b)

Figure 31. Pitch rate due to longitudinal stick ($\frac{q}{DFTE}$), ND–UA mode; $M = 0.70$, $h = 20,000$ ft.
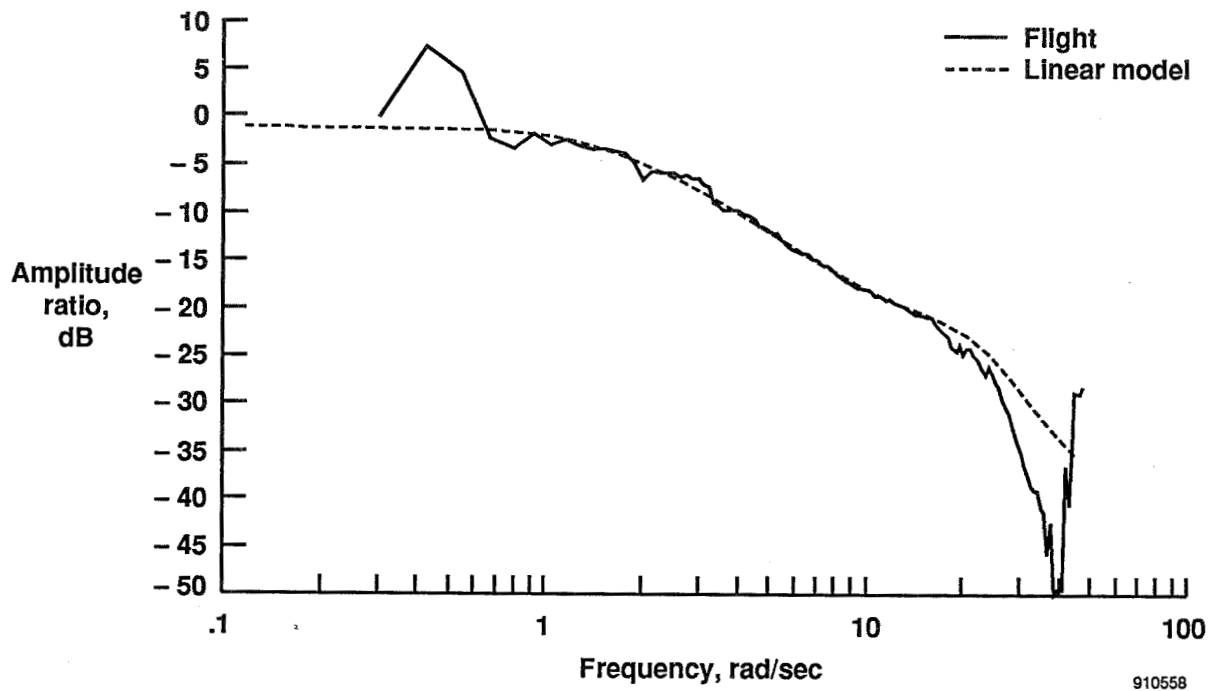
(a)
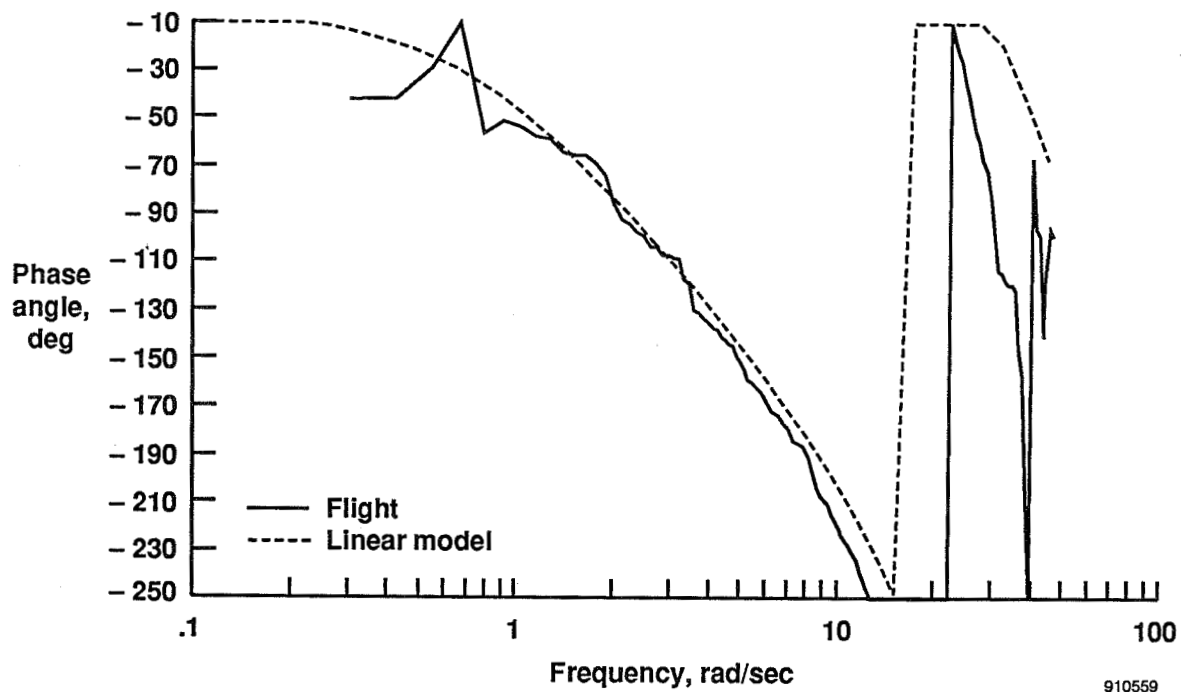
(b)

Figure 32. Normal acceleration due to longitudinal stick ($\frac{n_z}{DFTE}$), ND–UA mode; $M = 0.70$, $h = 20,000$ ft.

94
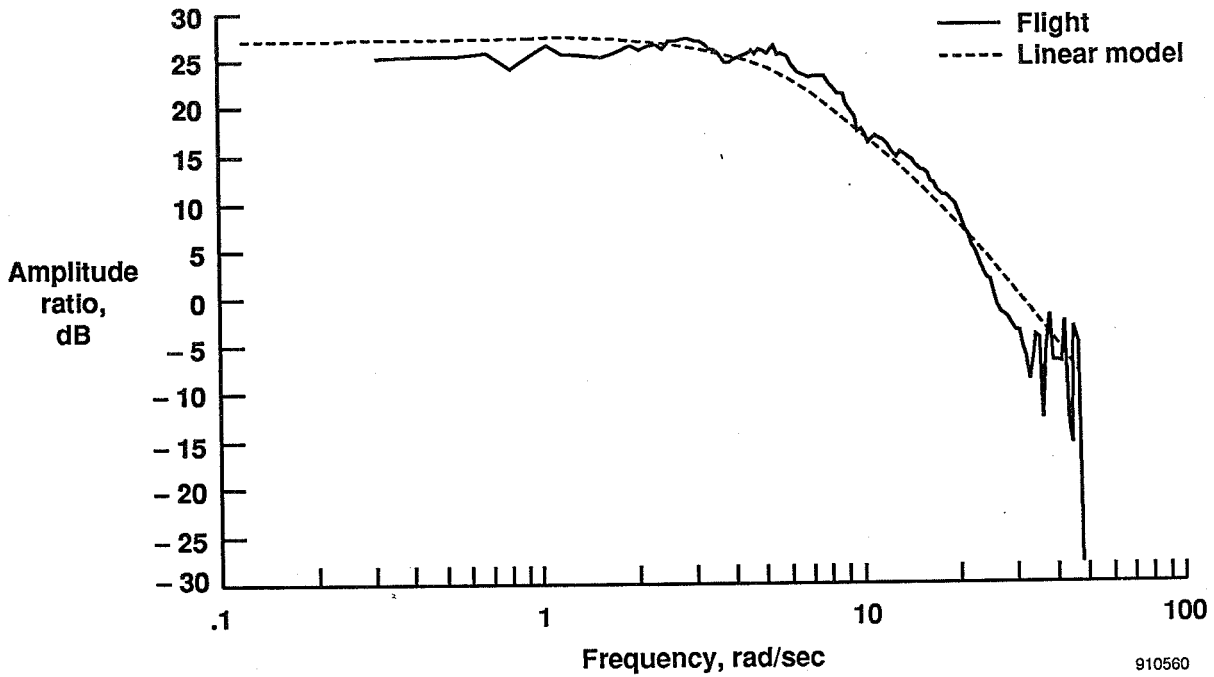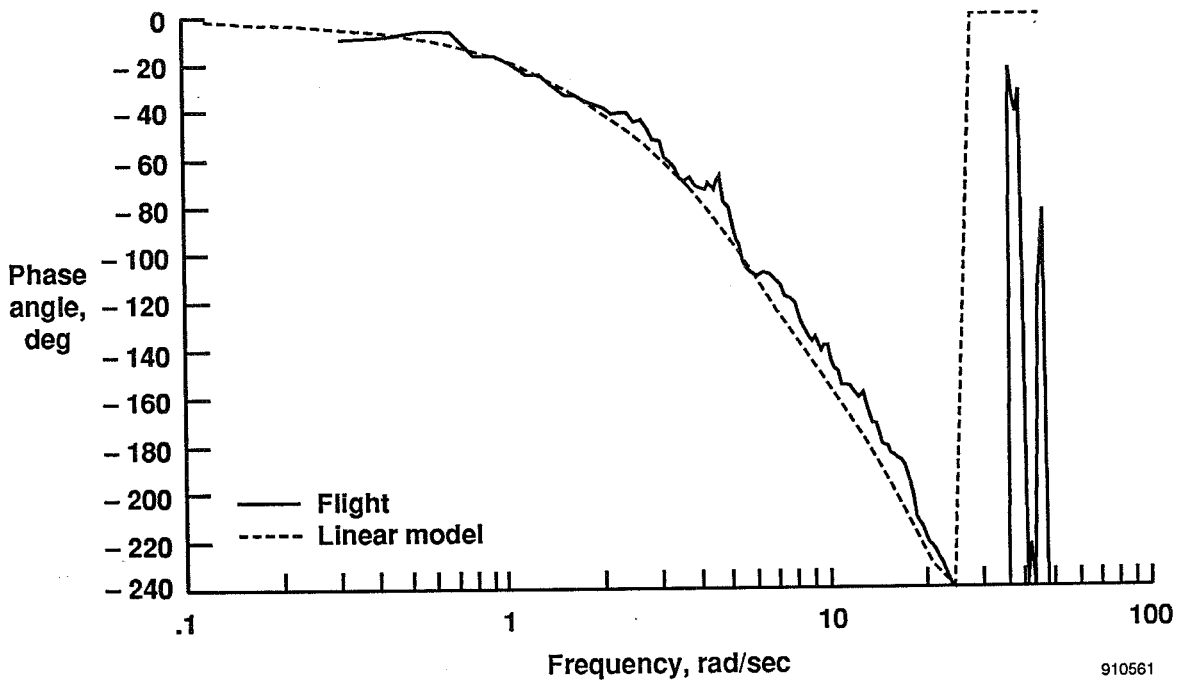
Figure 33. Roll rate due to lateral stick ($\frac{p}{DFTA}$), ND–UA mode; $M = 0.70$, $h = 20,000$ ft.
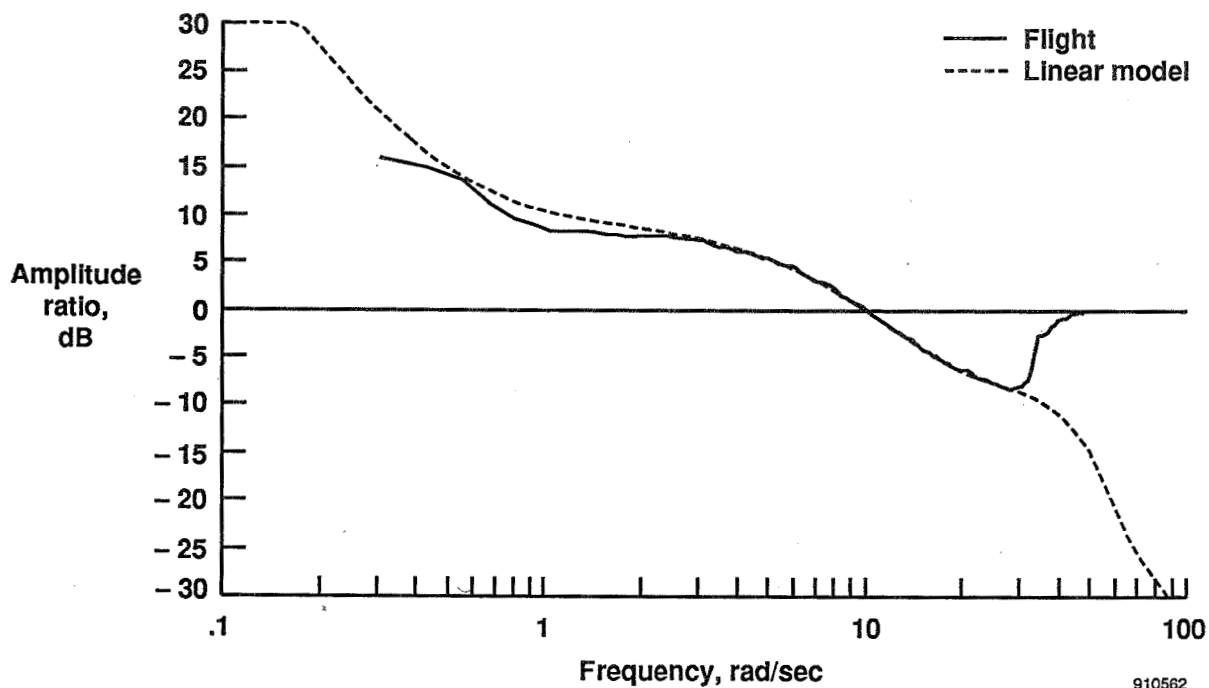
(a)
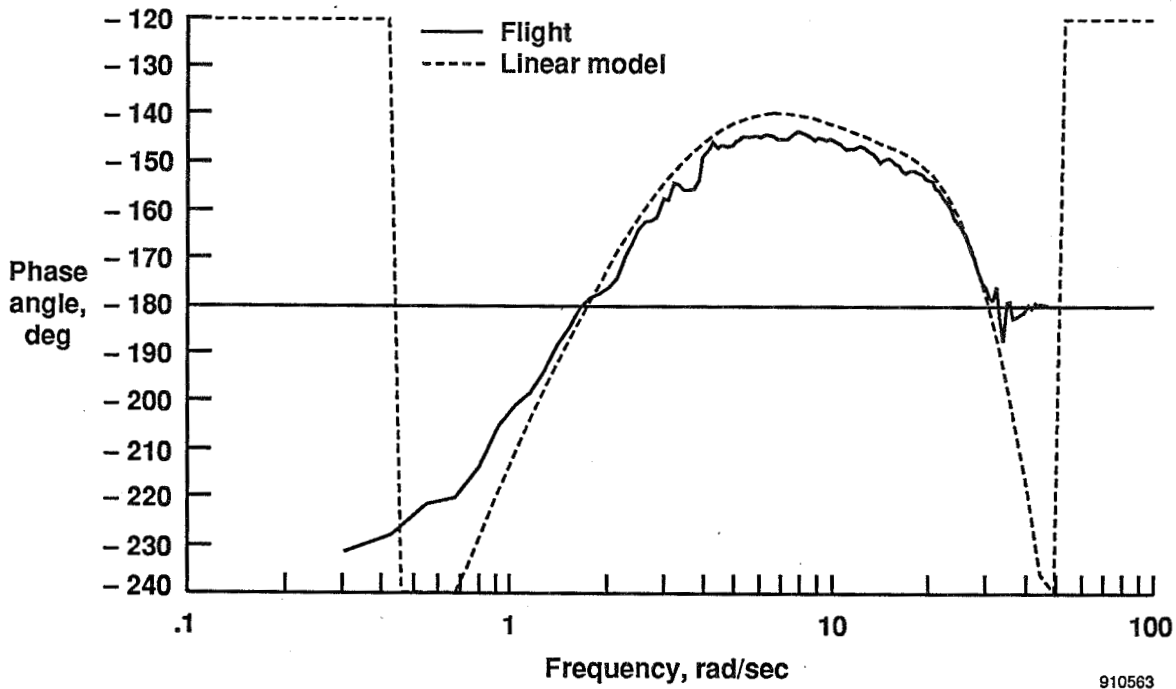
(b)

Figure 34. Open-loop frequency response ($\frac{y_{tc}}{e}$) AR–UA mode; $M = 0.70$, $h = 20,000$ ft.

96
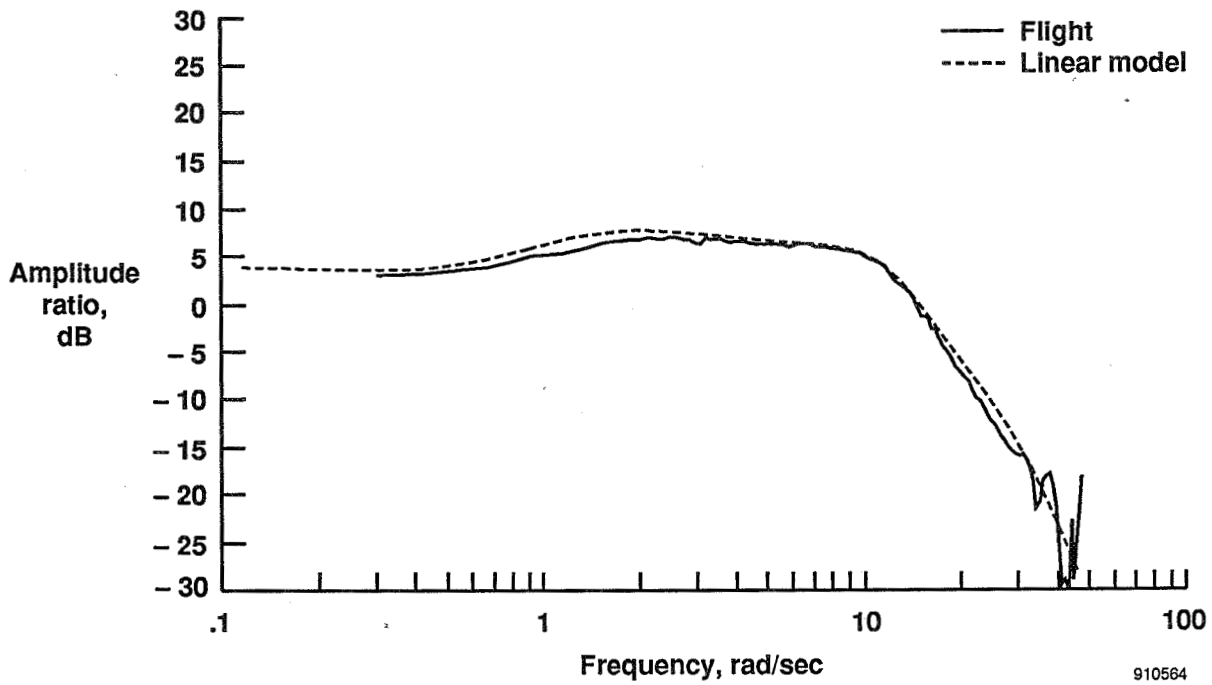
(a)
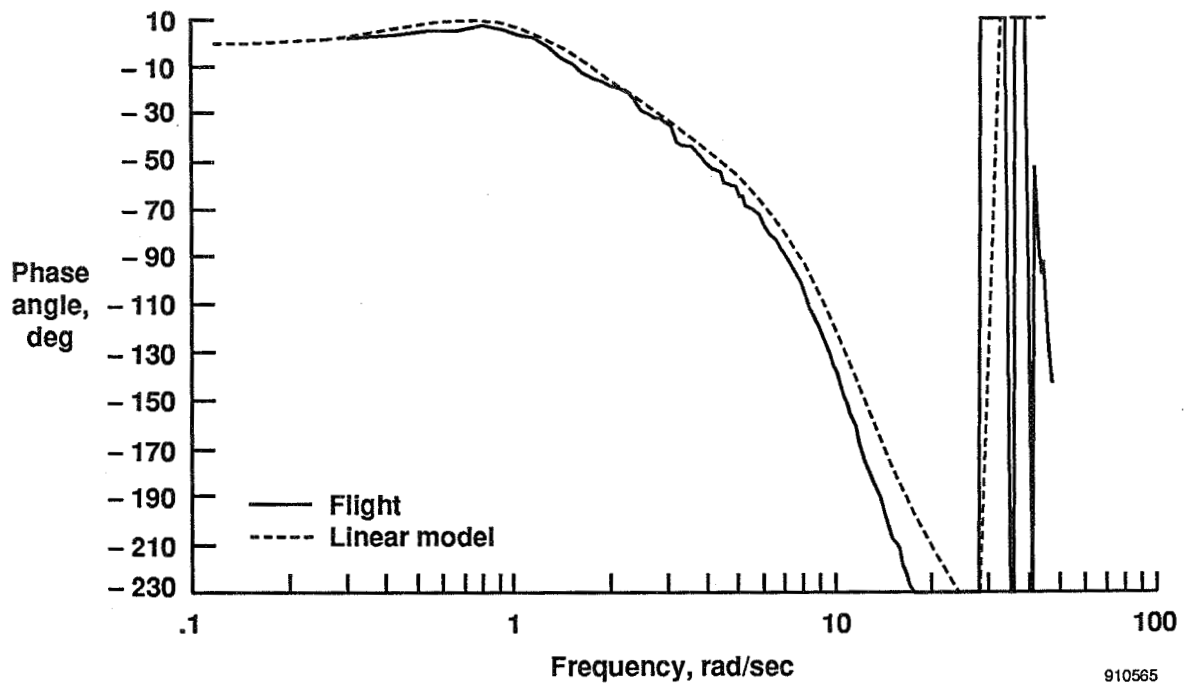
(b)

Figure 35. Pitch rate due to longitudinal stick ($\frac{q}{DFTE}$), AR–UA mode; $M = 0.70$, $h = 20{,}000$ ft.
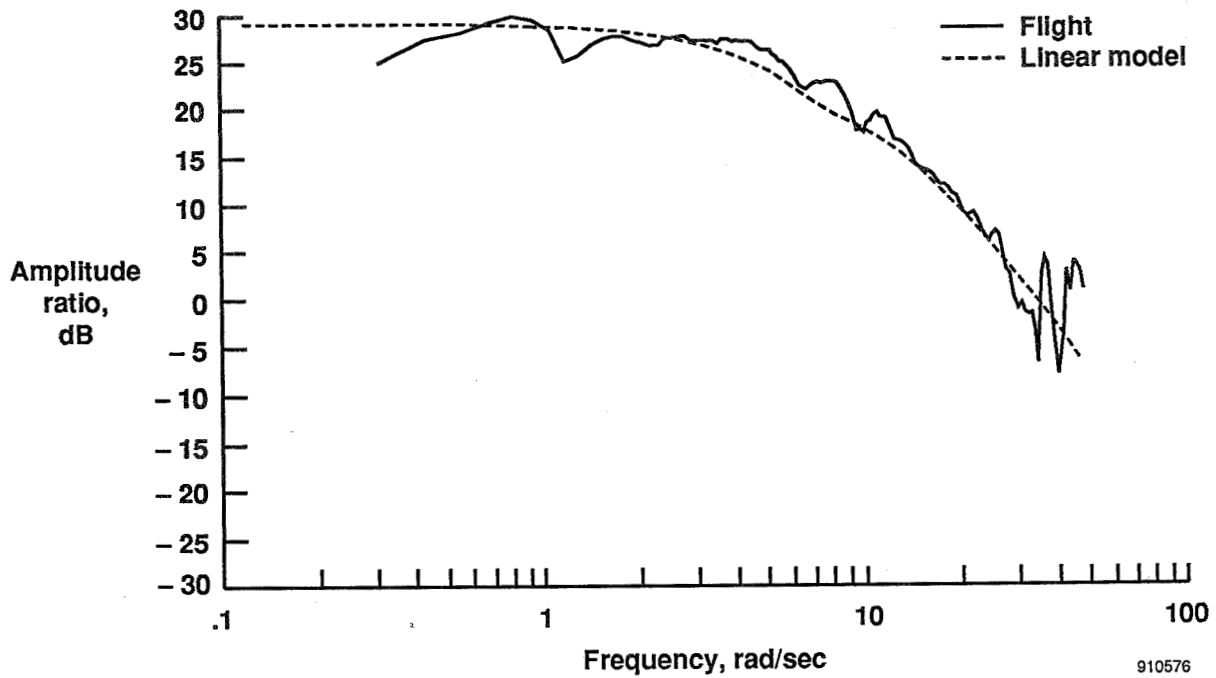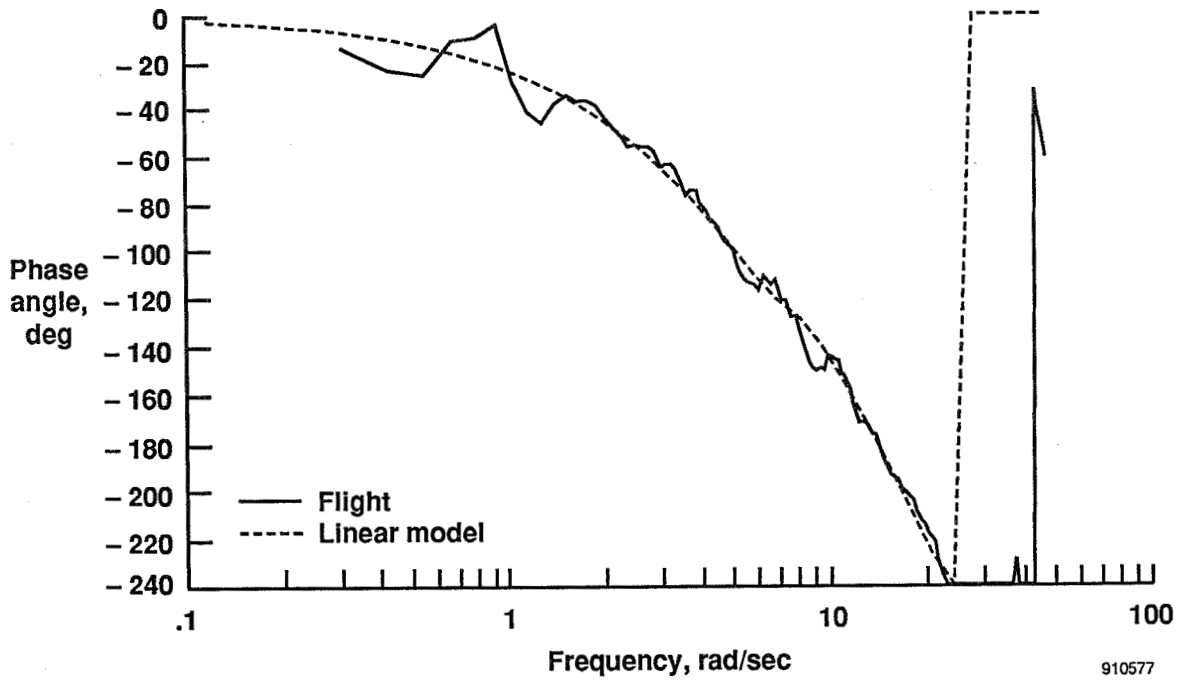
97
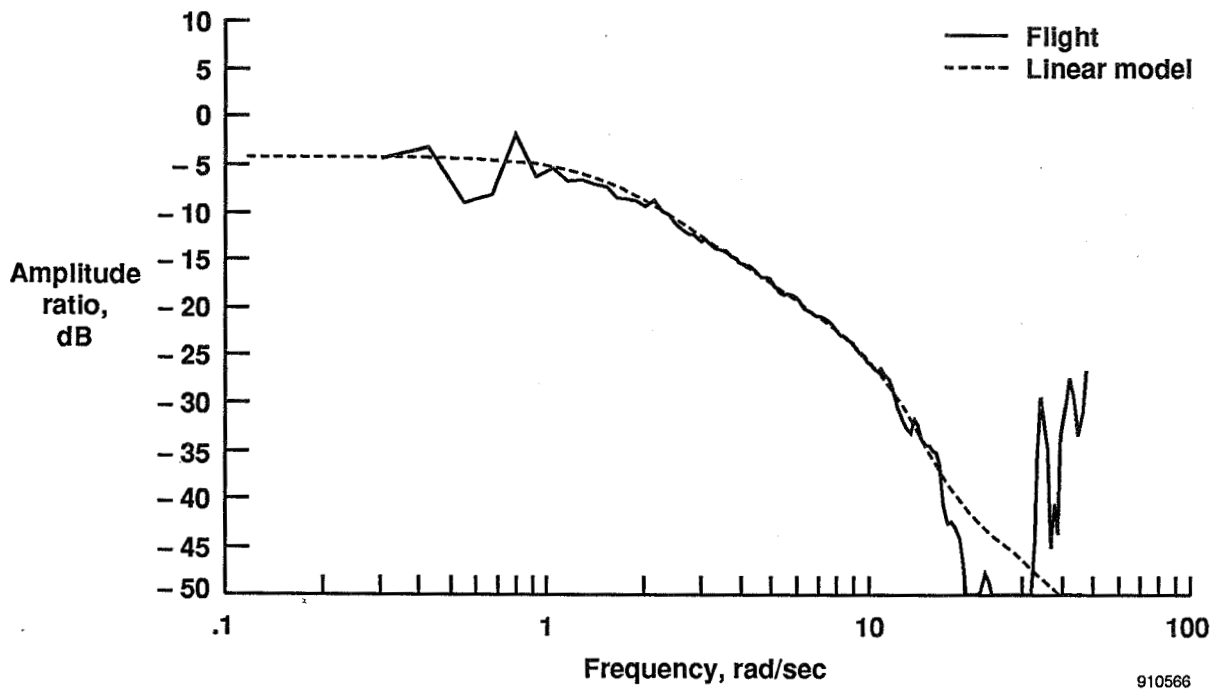
(a)
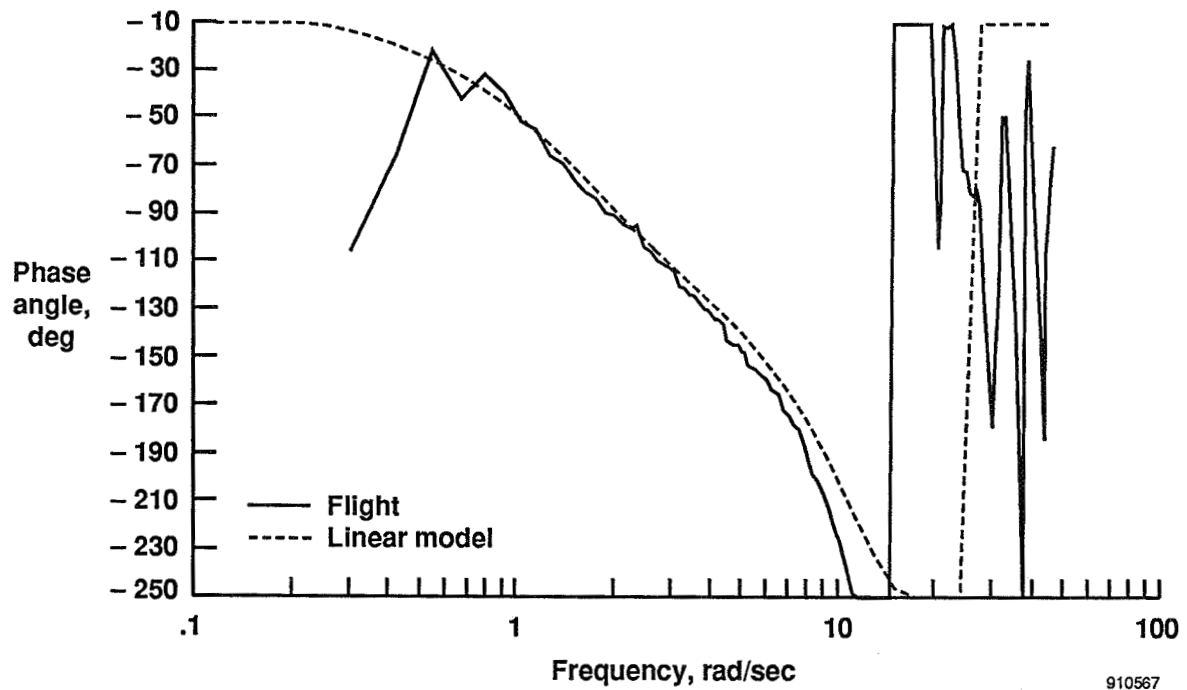
(b)

Figure 36.   Normal acceleration due to longitudinal stick ($\frac{n_z}{DFTE}$), AR–UA mode; $M = 0.70$, $h = 20,000$ ft.
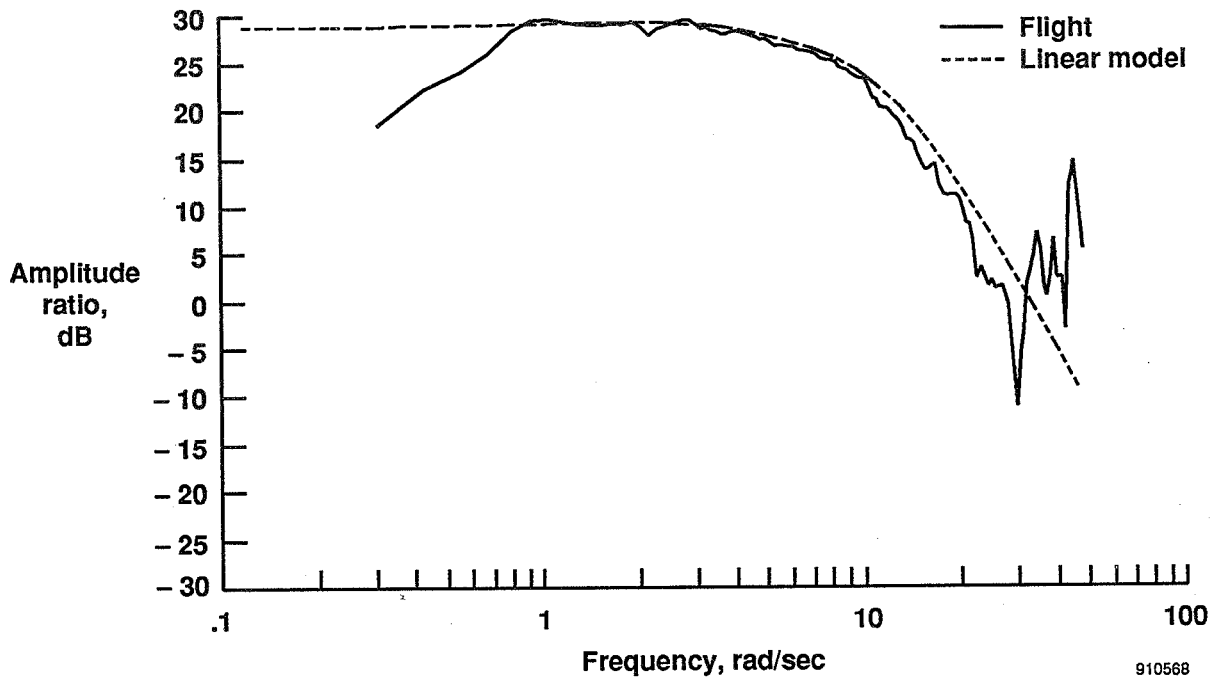
(a)
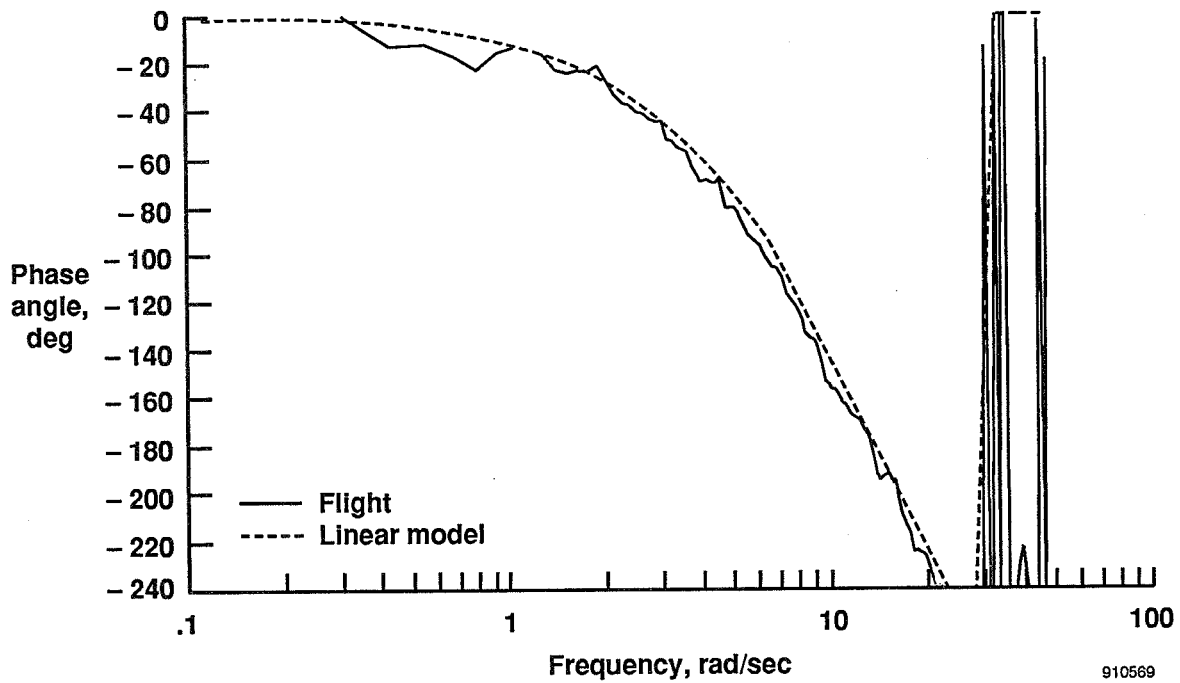
(b)

Figure 37. Roll rate due to lateral stick ($\frac{p}{DFTA}$), AR–UA mode; $M = 0.70$, $h = 20,000$ ft.

99

(a)

(b)

Figure 38. Open-loop frequency response ($\frac{y_{tc}}{e}$) ND–UA mode; $M = 0.90$, $h = 8,000$ ft.

Figure 39. Pitch rate due to longitudinal stick ($\frac{q}{DF_{TE}}$), ND–UA mode; $M = 0.90$, $h = 8,000$ ft.

(a)

(b)

Figure 40. Normal acceleration due to longitudinal stick ($\frac{n_z}{DFTE}$), ND–UA mode; $M = 0.90$, $h = 8,000$ ft.
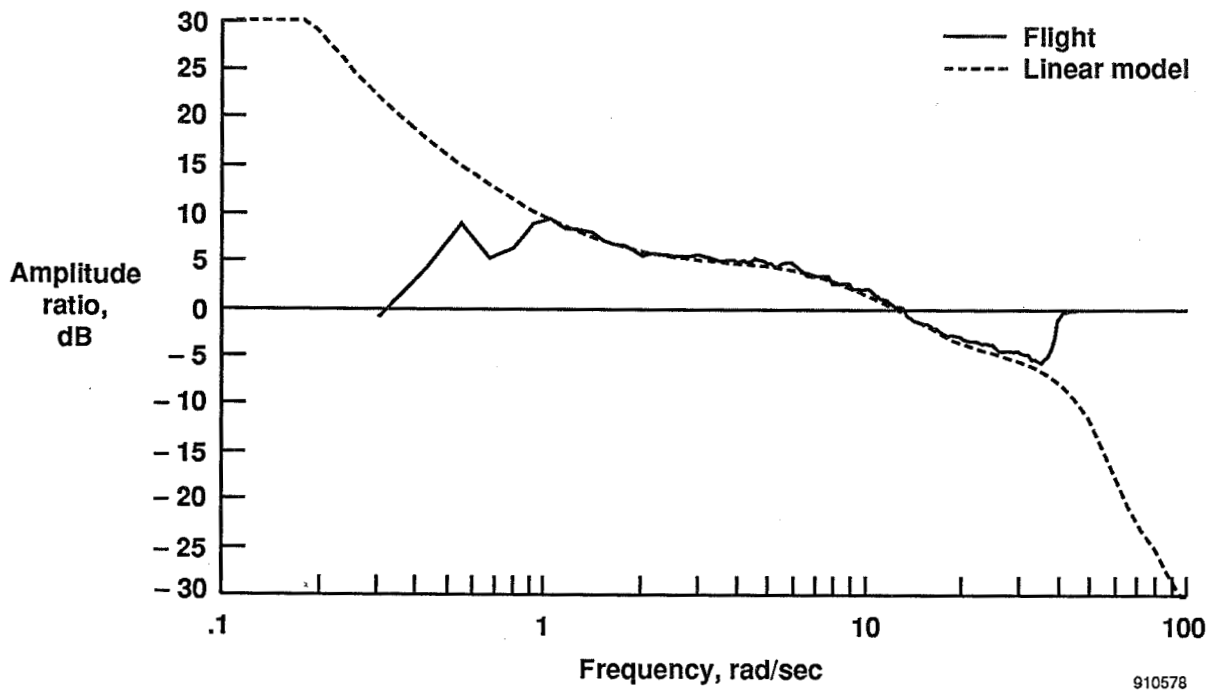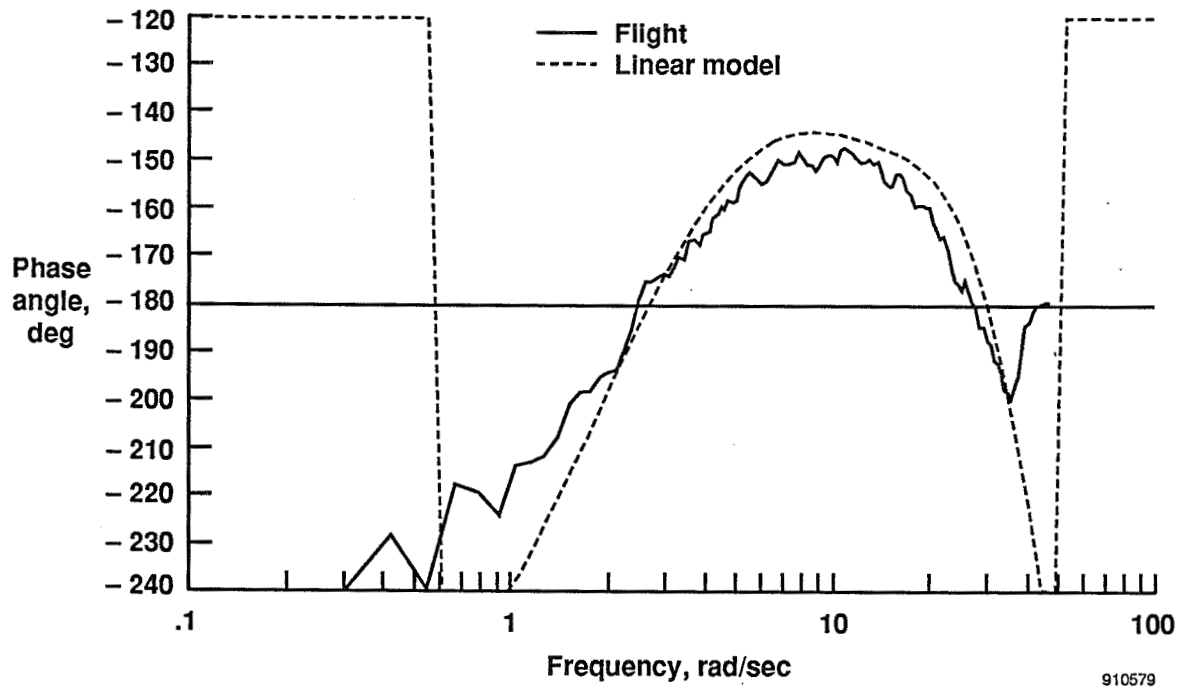
(a)

(b)

Figure 41. Roll rate due to lateral stick ($\frac{p}{DFTA}$), ND–UA mode; $M = 0.90$, $h = 8,000$ ft.
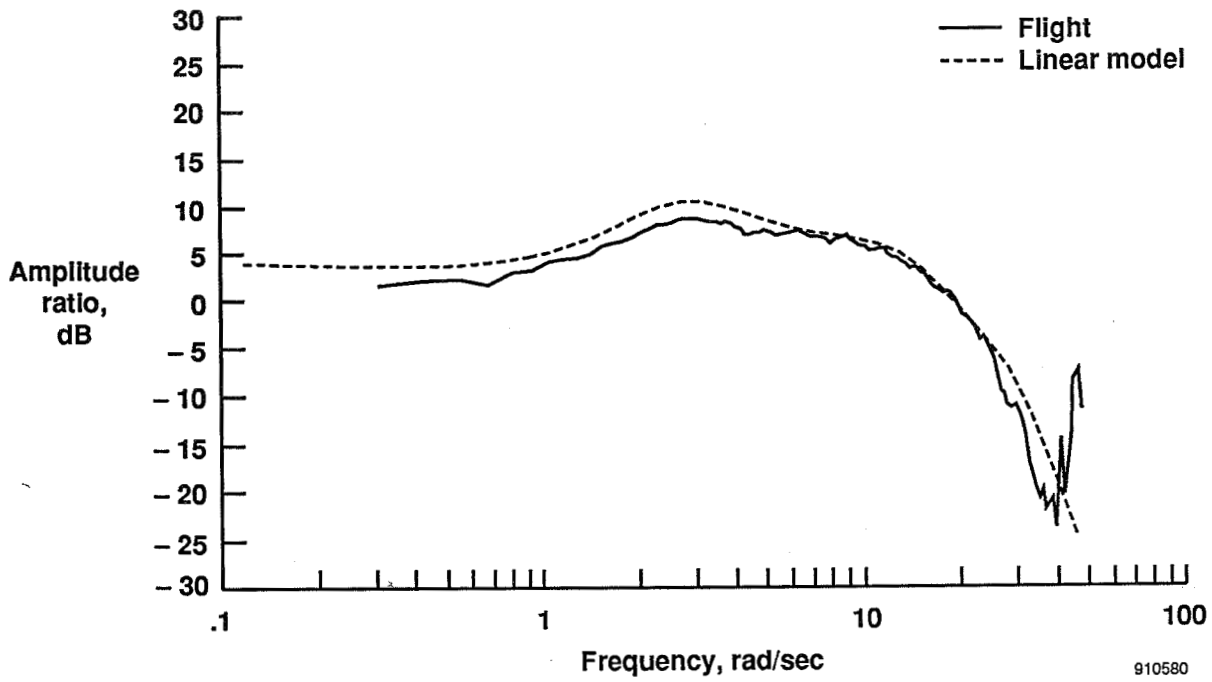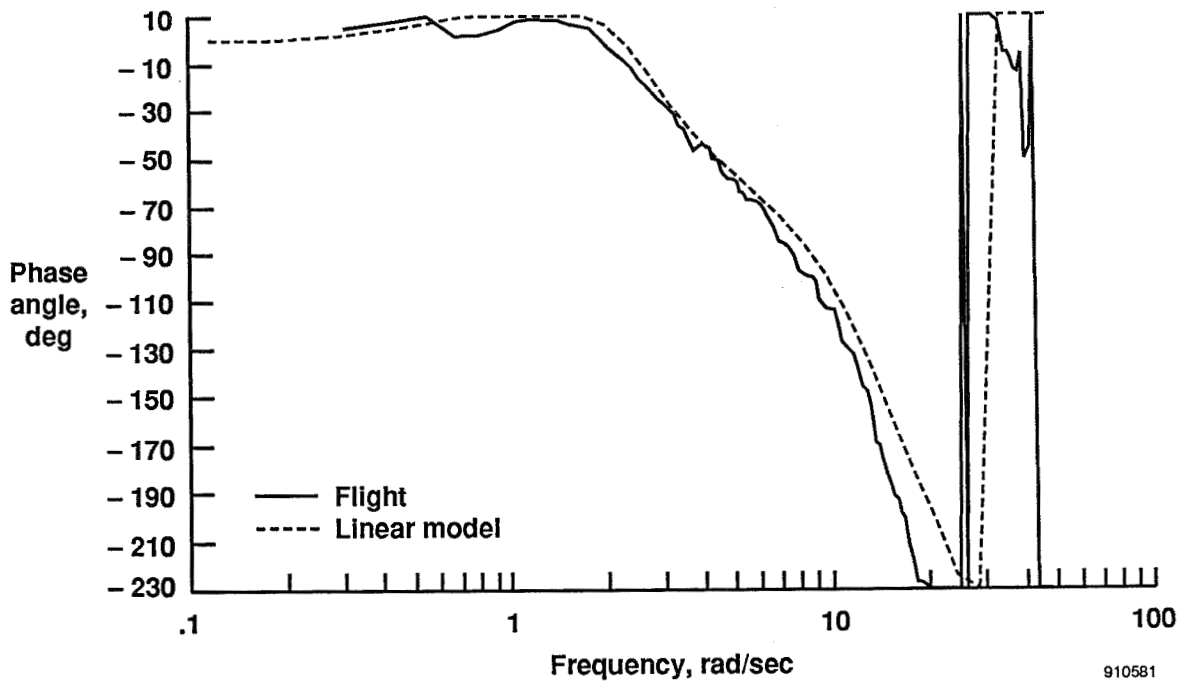
103

(a)

(b)

Figure 42. Open-loop frequency response ($\frac{y_{tc}}{e}$) AR–UA mode; $M = 0.90$, $h = 8,000$ ft.
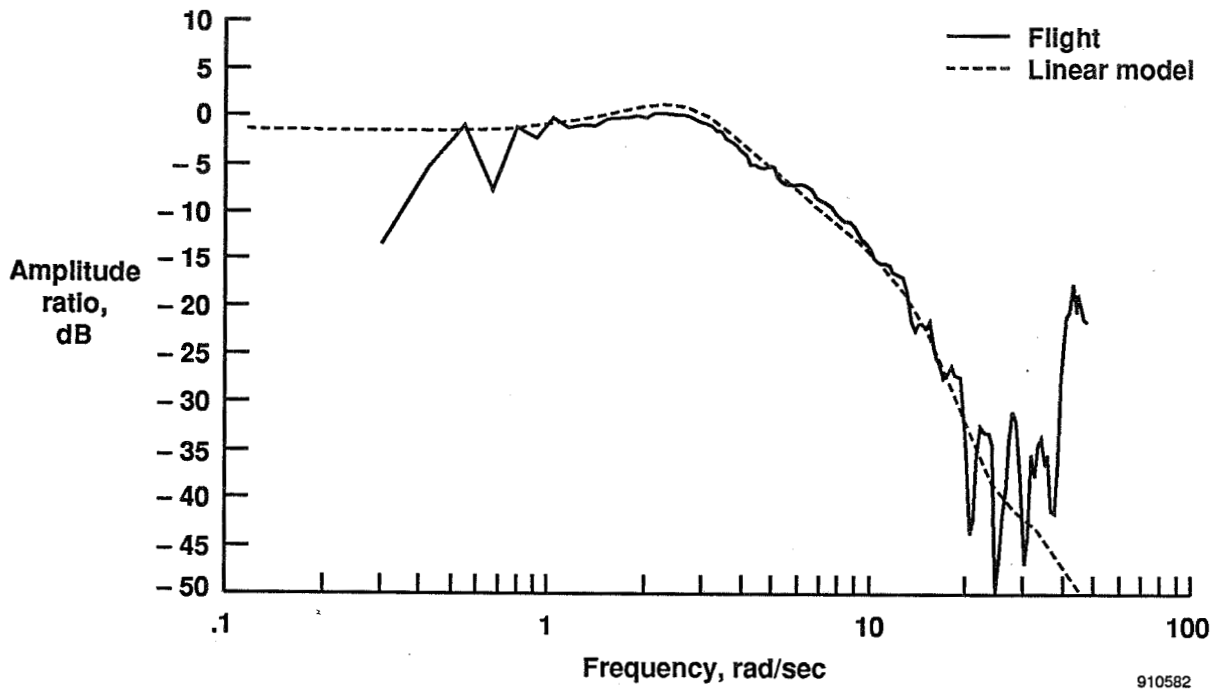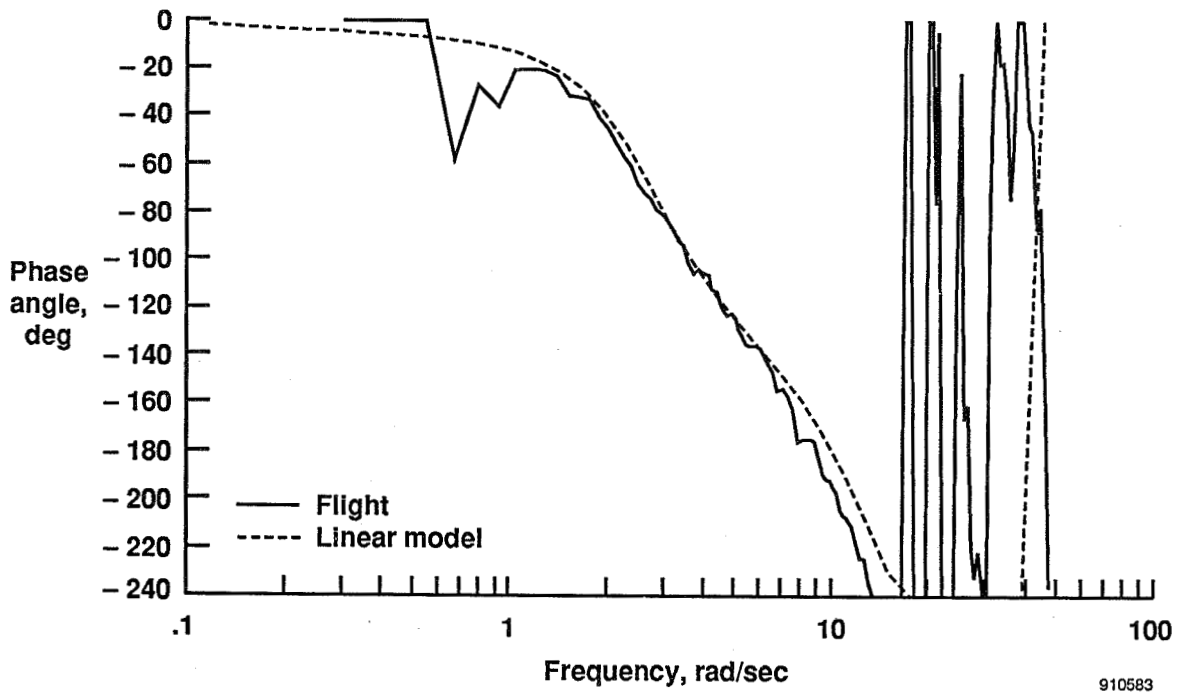
(a)

(b)

Figure 43. Pitch rate due to longitudinal stick ($\frac{q}{DFTE}$), AR–UA mode; $M = 0.90$, $h = 8,000$ ft.

(a)

(b)

Figure 44. Normal acceleration due to longitudinal stick ($\frac{n_z}{DFTE}$), AR–UA mode; $M = 0.90$, $h = 8,000$ ft.

REPORT DOCUMENTATION PAGE

Form Approved
OMB No. 0704-0188

Public reporting burden for this collection of information is estimated to average 1 hour per response, including the time for reviewing instructions, searching existing data sources, gathering and maintaining the data needed, and completing and reviewing the collection of information. Send comments regarding this burden estimate or any other aspect of this collection of information, including suggestions for reducing this burden, to Washington Headquarters Services, Directorate for Information Operations and Reports, 1215 Jefferson Davis Highway, Suite 1204, Arlington, VA 22202-4302, and to the Office of Management and Budget, Paperwork Reduction Project (0704-0188), Washington, DC 20503.

1. AGENCY USE ONLY *(Leave blank)*	2. REPORT DATE February 1992	3. REPORT TYPE AND DATES COVERED Technical Memorandum

4. TITLE AND SUBTITLE

Linearized Aerodynamic and Control Law Models of the X-29A Airplane and Comparison With Flight Data

5. FUNDING NUMBERS

WU-533-02-38

6. AUTHOR(S)

John T. Bosworth

7. PERFORMING ORGANIZATION NAME(S) AND ADDRESS(ES)

NASA Dryden Flight Research Facility
P.O. Box 273
Edwards, California 93523-0273

8. PERFORMING ORGANIZATION REPORT NUMBER

H-1676

9. SPONSORING/MONITORING AGENCY NAME(S) AND ADDRESS(ES)

National Aeronautics and Space Administration
Washington, DC 20546-0001

10. SPONSORING/MONITORING AGENCY REPORT NUMBER

NASA TM-4356

11. SUPPLEMENTARY NOTES

12a. DISTRIBUTION/AVAILABILITY STATEMENT

Unclassified — Unlimited
Subject Category 08

12b. DISTRIBUTION CODE

13. ABSTRACT *(Maximum 200 words)*

Flight control system design and analysis for aircraft rely on mathematical models of the vehicle dynamics. In addition to a six-degree-of-freedom nonlinear simulation, the X-29A flight controls group developed a set of programs that calculate linear perturbation models throughout the X-29A flight envelope. The models included the aerodynamics as well as flight control-system dynamics and were used for stability, controllability, and handling qualities analysis. These linear models were compared to flight test results to help provide a safe flight envelope expansion. This report presents a description of the linear models at three flight conditions and two flight control system modes. The models are presented with a level of detail that would allow the reader to reproduce the linear results if desired. Comparison between the response of the linear model and flight-measured responses are presented to demonstrate the strengths and weaknesses of the linear models' ability to predict flight dynamics.

14. SUBJECT TERMS

Aircraft; Flight control system; Linear aerodynamic model; State space, rigid body dynamic models; X-29A airplane

15. NUMBER OF PAGES

116

16. PRICE CODE

A06

17. SECURITY CLASSIFICATION OF REPORT Unclassified	18. SECURITY CLASSIFICATION OF THIS PAGE Unclassified	19. SECURITY CLASSIFICATION OF ABSTRACT	20. LIMITATION OF ABSTRACT

NASA